5-2013

Growth and Electric Field Control of Phase Separated Manganites

Hangwen Guo
hguo4@utk.edu

To the Graduate Council:

I am submitting herewith a dissertation written by Hangwen Guo entitled "Growth and Electric Field Control of Phase Separated Manganites." I have examined the final electronic copy of this dissertation for form and content and recommend that it be accepted in partial fulfillment of the requirements for the degree of Doctor of Philosophy, with a major in Physics.

Pengcheng Dai, Major Professor

We have read this dissertation and recommend its acceptance:

Norman Mannella, Janice Musfledt, Jian Shen

Accepted for the Council:

Carolyn R. Hodges

Vice Provost and Dean of the Graduate School

(Original signatures are on file with official student records.)

Growth and Electric Field Control of Phase Separated Manganites

A Dissertation

Presented for the

Doctor of Philosophy Degree

The University of Tennessee, Knoxville

Hangwen Guo

May 2013

Acknowledgements

First and foremost, I would like to show my deepest gratitude to my supervisor, Dr. Jian Shen, a respectable, responsible and resourceful scholar, who has provided me with valuable guidance in every stage of this thesis. The most valuable gift I learned from you is that you always provide a clear idea and a smart angle to look at it, then leaving the space of thinking and working to me. In these 5 years, I really learned on how to think and work "independently" and I'm sure I will appreciate this in my whole life.

Zac Ward has been my *de facto* advisor in day-to-day research and has been an incredible influence. He is such an excellent experimentalist and a kind person who is willing to teach me everything he knows about. I feel really lucky to work with him and words really cannot express the gratitude that I fell for all he has done for me.

I need to thank my committee: Pengcheng Dai, Norman Mannella and Janice Musfeldt. I appreciate them giving me their valuable time and even more valuable guidance.

I want to specially thank Xiaoshan Xu, who has been working with me in ORNL for two years. His dedication to science really impressed me and he always knows the right answer to every question I asked. It's a great experience working with him.

It was my pleasure to work with Dali Sun and Wenbin Wang. You are not only co-workers, but also best friends in my PhD life. I have been lucky to work with Paul Snijders over the last couple of years. I enjoy so much on his insight on science and sense of humor of his personality. Doing my research at ORNL has allowed me to interact with some truly amazing people: Hans Christian, Philip Rack, Joo Hyon Noh, Zheng Gai,

Chengjun Sun, Lifeng Yin, Xiaoying Xu, Min Gao and Katyayani Seal. You all helped me with my experiments and gave me good advices.

The 5 years experiences in America have been the most amazing time in my life, both scientifically and personally. I want to thank Wei Zhang for accompanying me of the happiest ever two and a half years in my life. I want to thank Michelle Lee and Wen Wang for the deep encourage when I was at my lowest. Also, thanks to all my UTK friends for all the life together.

Finally and most importantly, I want to say to my mom, dad, grandma, grandpa, aunts, uncles, Ada, Jiawen and Min, it is hard for all of us since we are 7500 miles apart. It is their support that has allowed me to fulfill my dream of going abroad and chasing my career. Without them, I won't be where I am.

Abstract

Perovskite Manganites have received numerous attentions due to exotic behaviors such as colossal magnetoreistance (CMR) and electronic phase separation (EPS). The purpose of my research is to answer fundamental questions about the growth properties of manganites and electric field control of the EPS properties.

Experimental study was conducted on controlling the growth mode of $La_{0.7}Sr_{0.3}MnO_3$[Lanthanum Strontium Manganese Oxide] thin films using pulsed laser deposition. Different thin film morphology, crystallinity and stoichiometry have been observed depending on growth parameters. To understand the microscopic origin, the thermodynamic processes were theoretically analyzed and a growth diagram was constructed. Three boundaries between highly and poorly crystallized, layer-by-layer and 3D, stoichiometric and non-stoichiometric growth were identified in the growth diagram. A good fit of our experimental observation with the growth diagram was found. This case study demonstrates that a more comprehensive understanding and the predicting of the growth mode in PLD is possible.

Behaviors such as high Tc superconductivity, CMR, and the metal-insulator transition, have been tied to inherent electronic phases coexisting in a single crystal material. These phases offer the potential for creating new types of electronic devices based on tuning the finely balanced energetics stabilizing emergent phase domains. Here we demonstrate novel approaches to induce resistive electric field effect transitions based on the modification of the inherent electronic domain structures in single crystal materials. A phase separated manganite system confined to a scale which isolates a few electronic domains is controlled using laterally gated electrodes to tune percolative conduction

channels which give repeatable resistive changes. This technique also makes it possible to create multistate switching devices from a single confined transport channel. Electro-resistance up to 400% is observed during the cooling process under static electric field. These findings provide an avenue to control inherent electronic phases as a means of creating novel nano-electronic devices.

While manganites are the primary focus throughout this dissertation, both the growth diagram and spatially confined E-field techniques can be extended to understand fundamental growth phases in other epitaxial oxides materials and exploring the electric field effect on different oxides system.

Table of Contents

List of Figures

Chapter 1 Introduction and Background

1.1Introduction

When we talk about the phrase “condensed matter physics”, most of people in the real world have no idea what we are talking about. So, I always like to describe my work as “designing and fabricating new materials” and hope it makes some sense. As a dissertation, most of the readers should have some backgrounds on what condensed matter physics means and I will present my dissertation in a more professional way.

Nowadays, the condensed matter physics research is becoming more and more industrial driven so that words such as nanoscale, novel materials are widely used. Indeed, my work contributes as small part of this research landscape. While most of my research is done not exactly in the scale of nanometer, but as I will show you later, the system I worked on can be considered as a prototype system towards achieving new devices and functional structures in nanometer scale. Also, I want to point out here that the purpose of my work is not focused on how to improve the recent nano-electronic devices functionality, but on discovering new physics phenomena on serving as new possibilities to achieve new types of useful devices.

The structure of this thesis is arranged as follow: Chapter 1 is introduction and basic physics of manganites system and the concept of electronic phase separation. Chapter 2 will discuss the experimental methods and equipment we used. Chapter 3 will be combined theory and experiments on discussing the growth phase diagram of manganites grown by Pulsed Laser Deposition Technique. Chapter 4 will discuss my results on electric field control of electronic phase separation in spatially confined manganites. Chapter 5 will give some outlook about future works and directions.

1.2 Basics of Perovskite Manganites

The works described in this thesis are all done in the system of perovskite manganites thus it is important to describe their structural and electronic properties.[1] As a member of strongly correlated materials,[2] the structure of perovskite manganites is of great importance on influencing the electronic and magnetic properties.[3] The ideal perovskite form is cubic with an empirical formula ABO_3—the A cations are located on the corners, the B cation is located in body center, and the oxygen occupy the faces, as shown in Figure 1-1.[4] Such crystal-field split the Mn *d* levels into low lying three t_{2g} states and high level two e_g states, as shown in Figure 1-2.[5]

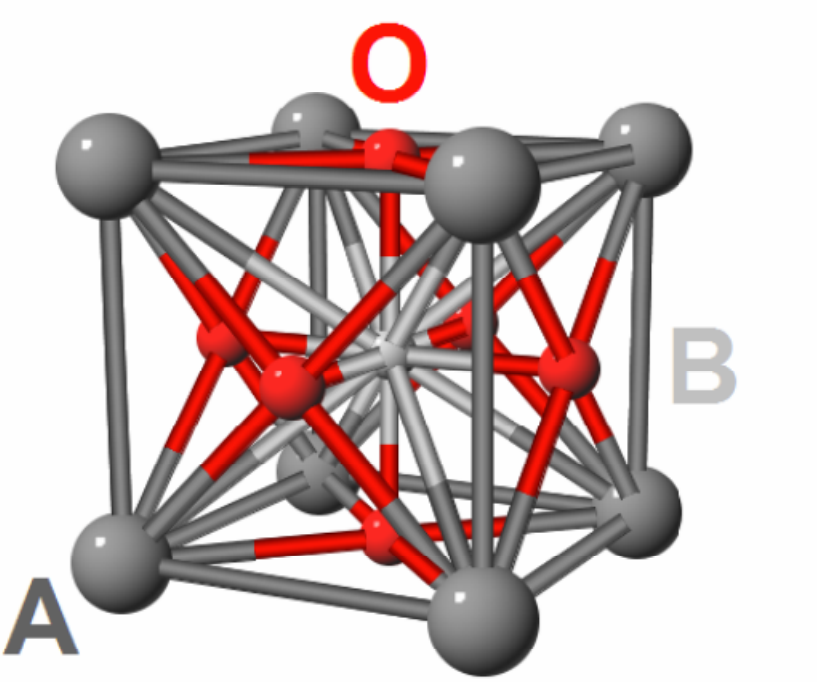

Figure 1-1: Perovskite structure. A-site is marked as dark grey at the corners of cubic structure. B-site is marked as light grey in the center of octahedral, representing Mn here. Oxygen is shown as red. – Reproduced from Ward[4] with permission.

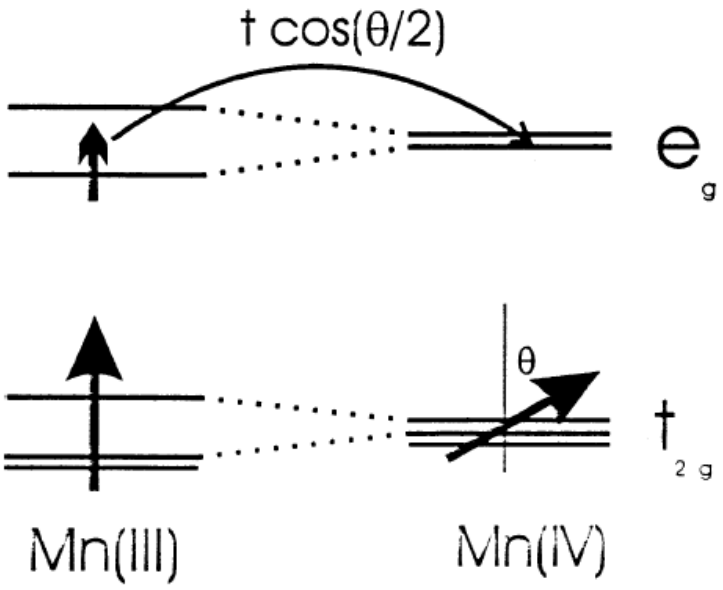

Figure 1-2: Electronic configuration for Mn^{3+} and Mn^{4+} ions in perovskite structure. The Mn^{3+} on the left shows the presence of Jahn-Teller splitting of e_g and t_{2g} orbitals due to breaking of cubic symmetry of oxygen octahedron distortion. The Mn^{4+} on the right is shown as cubic symmetry. – Reproduced from Mathur, *et al*[5].

Let's first consider the parent compound of $LaMnO_3$. Each e_g level has one electron occupied due to Coulomb repulsion so that they are localized. The direct on-site exchange interaction aligns the spins of different *d* orbitals. Thus, $LaMnO_3$ is an antiferromagnetic insulator. The two degenerated e_g levels have the tendency towards splitting to lower the total energy of the system, an effect known as Jahn-Teller (JT) distortion.[6] Such distortion behaves as oxygen cage deviate from cubic symmetry and is widely recognized in perovskite manganites. While the $LaMnO_3$ represent the case of zero doping (x=0), A finite doping of A site ions (x>0) can empty some of the e_g levels so that hopping is possible. As indicated in Figure 1-2, the exchange coupling J between the

e_g carrier and core t_{2g} spin is larger than the hopping matrix element of neighbouring e_g electrons. Also, the kinetic energy of itinerant electrons are minimized if all the t_{2g} core spins aligned in parallel, a famous mechanism known as double exchange interaction which proposed to explain ferromagnetic metal phase at low temperature in doped manganties (x>0), as illustrated in Figure 1-3.[7–9]

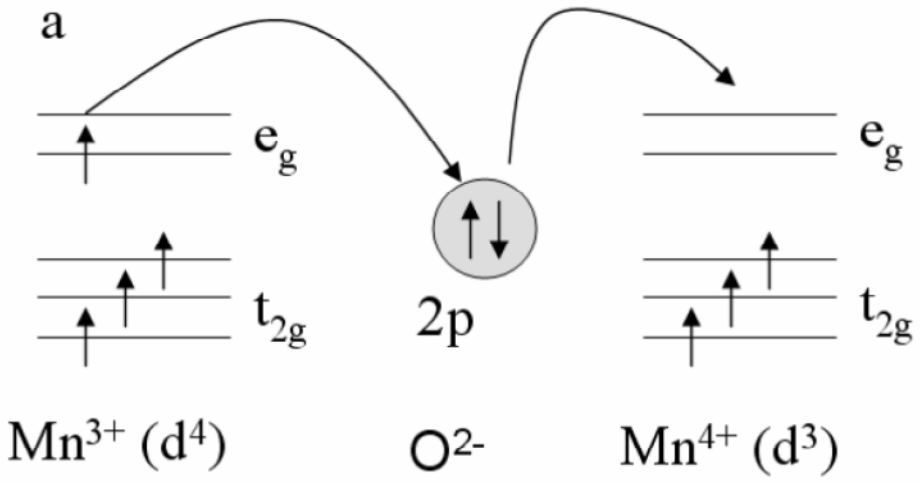

Figure 1-3: Zener's double exchange model as the basis of ferromagnetism in perovskite manganites.

Among doped manganites, three different phases are widely seen: Ferromagnetic metal phase (FMM), Charge ordered insulator phase (COI) and Paramagnetic insulator phase (PMI). As an example, a phase diagram of $LaCaMnO_3$ (LCMO) with varying doping level is shown in Figure 1-4.[10] Here we first discuss separately the features of these three phases, but note that these phases may coexist under different length scales, which will be discussed in the next section.

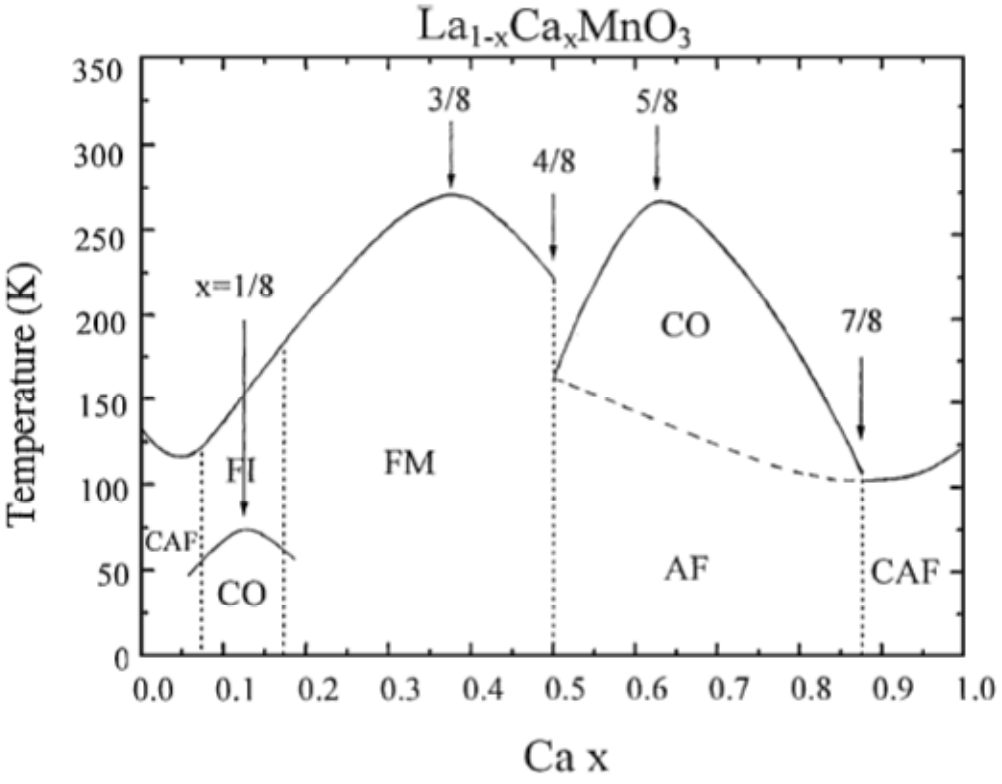

Figure 1-4: Phase diagram of $La_{1-x}Ca_xMnO_3$. The FM, AF phases are under discussion here. Taken from ref [10][10].

The FMM phase normally occurs at low temperature and are most pronounced at x=0.3 in the case of LCMO. As described above, the metallic behavior mainly comes from the double exchanged transport through O-Mn-O bonds and the JT fluctuations are strongly suppressed.

The charge ordered phase is recognized as ground states among many manganites at different doping range such as $PrCaMnO_3$. As discussed above, the localization came from JT distortion can be order because the oxygen octahedral share corners with its neighbour and the distortions about one Mn site are anti-shared with a neighbour.[5] Such COI phases are often recognized as stripe patterns in TEM techniques.[11–13] Figure 1-5 shows an example of COI stripes patterns in the system of $La_{0.25}Ca_{0.75}MnO_3$ from ref 10. Such phenomena strongly related to the A site ionic radius $<r_A>$. Charge carriers tend to localize and energetically favorable to order along with the orbital order, which can be attributed to strongly JT distorted region of Mn^{3+} O6 octahedra.[11] Note that the stripes can show strong commensurability effects as stabilized phase even though the doping can be incommensurate. The nature of this repeating commensurate effect is still not universally agreed. Aside from this charge and orbital ordered observation, there are phases with only charge-ordered but not orbital-ordered, suggesting strong local fluctuation and random orientation of JT distortion.[14]

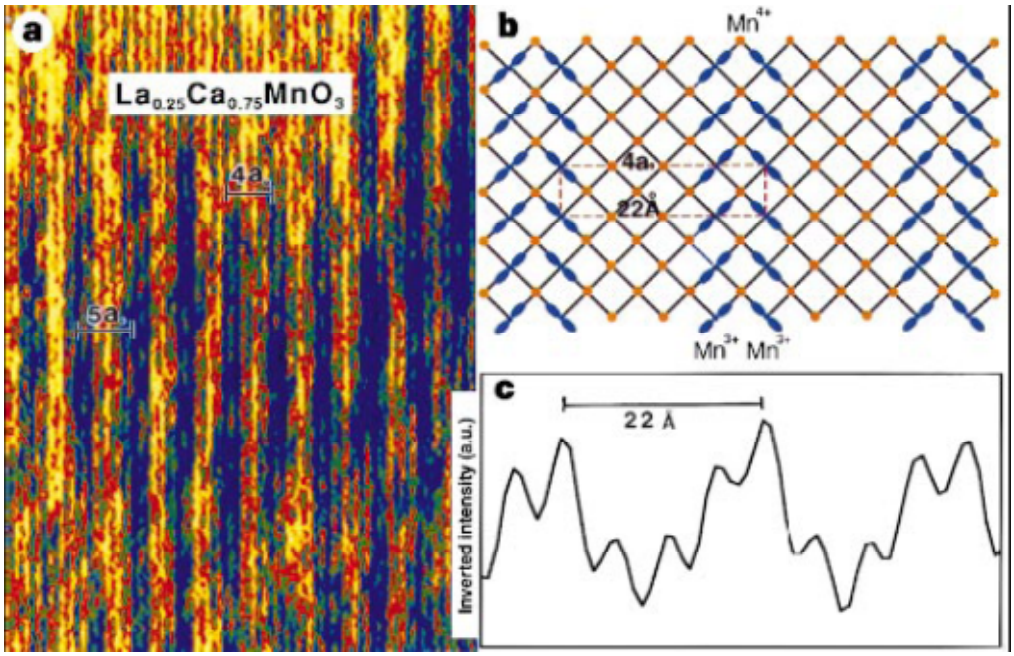

Figure 1-5: Pairing of charge ordered stripes in $La_{0.25}Ca_{0.75}MnO_3$. (a)TEM image showing stripes of $4a_0$ periodicity. (b)Proposed model showing paired Jahn-Teller stripes. (c) inverted intensity scan showing the stacking fault of $5a_0$ paired Jahn-Teller stripes in (a). Taken from ref [11][11].

The PMI phase is often observed at certain temperature window and always associated with polarons, which small regions of lattice distortion are generated by high local densities of carriers.[15,16] Such PMI phase is found to be quasi-insulating which is thermally activated and can explain some of the CMR effect in manganites.

1.3 Electronic Phase Separation (EPS)

The three phases described above are typical features found among many perovskite manganites. However, to a large extent, these phases do not appear individually. In other words, these electronic and magnetic phases may spatially coexist in certain temperature and magnetic field window, although chemically the sample is still random alloy.[17–20] Such domain can coexist on the order of nanometers to microns depending on the chemical composition of the material.

While the mechanism of such EPS effect is still under debate and not fully understood, different probing techniques such as transmission electron microscopy (TEM)[21], magnetic force microscopy (MFM)[22,23] and scanning tunneling spectroscopy (STS)[24,25]. Here we show two examples of sub-micron scale EPS in the system of $(LaPr)_{1-x}Ca_xMnO_3$ (LPCMO), which is the system where we did most of our studies on. In the case of LPCMO, a typical insulator to metal transition are widely seen in a wide doping range from the electronic transport data, as shown in Figure 1-6.[21] Colossal Magnetoreistance (CMR), an effect of orders of magnitude change in resistance under applied magnetic field is seen in the system. Such resistivity peak during the cooling process indicates a transition from insulating states towards metallic states. Another interesting effect is the hysteresis present on the resistivity for cooling and warming curves, indicating some sort of phase coexistence inside the system. Indeed, Figure 1-7a confirms the phase separation from TEM images, which shows the large submicron coexistence of the insulating (bright) and metallic (dark) phases. Such large scale electronic phase coexistence is somewhat striking because the Coulomb energy associated with big amount of charge density fluctuation is prohibitive on such length

scales. In Figure 1-7b, the MFM study associated with transport measurement reveals some of the mystery of EPS. While the transport data shows similar behavior as Figure 1-6, the temperature dependent MFM images clearly shows a growing of FMM phase while cooling. The authors speculate that such metal-insulator transition is associated with percolation of the ferromagnetic metallic channels in the film. In later chapters, we will show our novel way of spatial confinement on unraveling more intrinsic features of EPS.

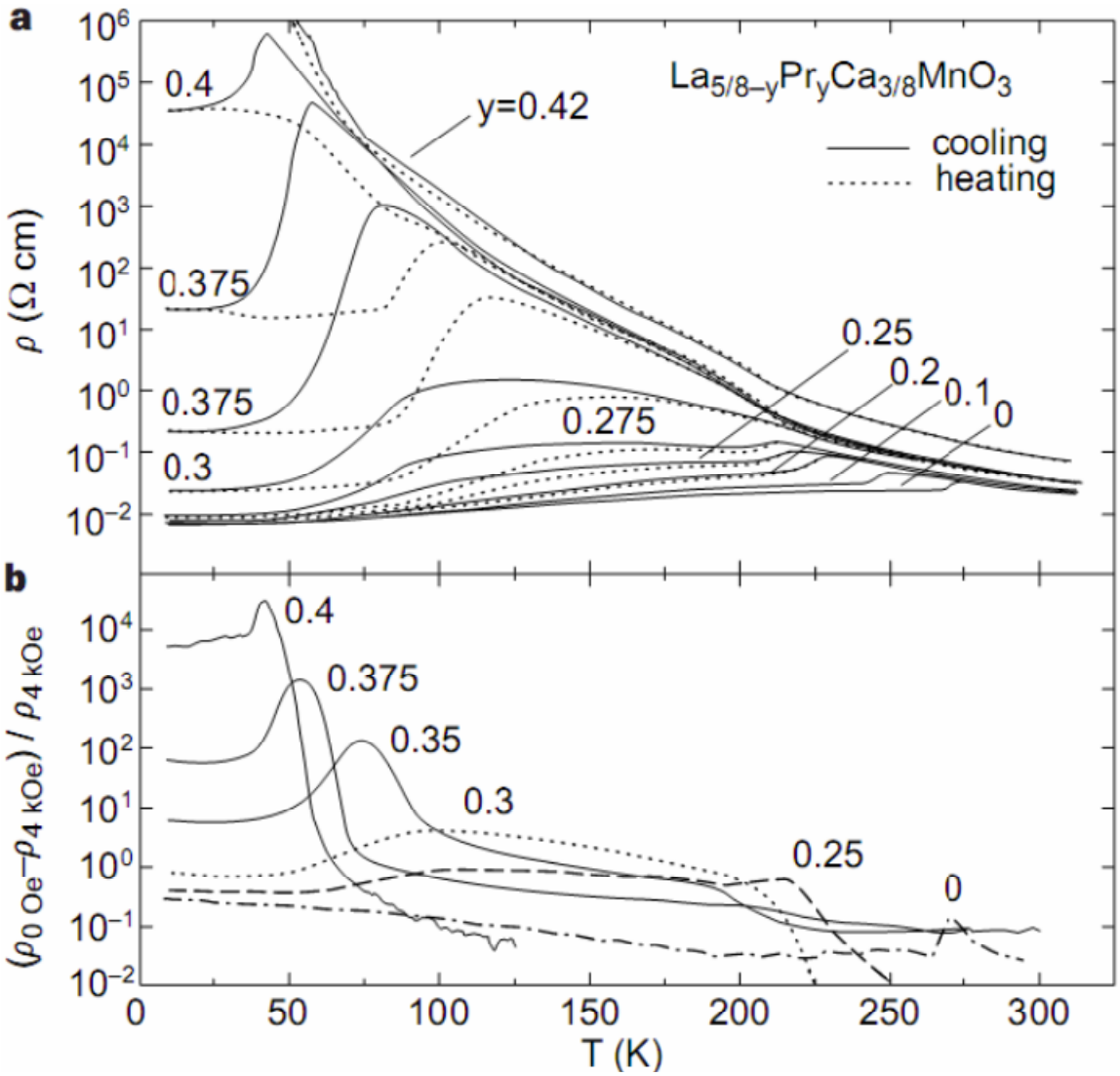

Figure 1-6: transport measurement of Colossal Magnetoresistance (CMR) manganites LPCMO. (a) Resistivity vs. temperature for different doped LPCMO. (b) Relative change in resistivity on application of 0.4T magnetic field. Taken from ref [21][21].

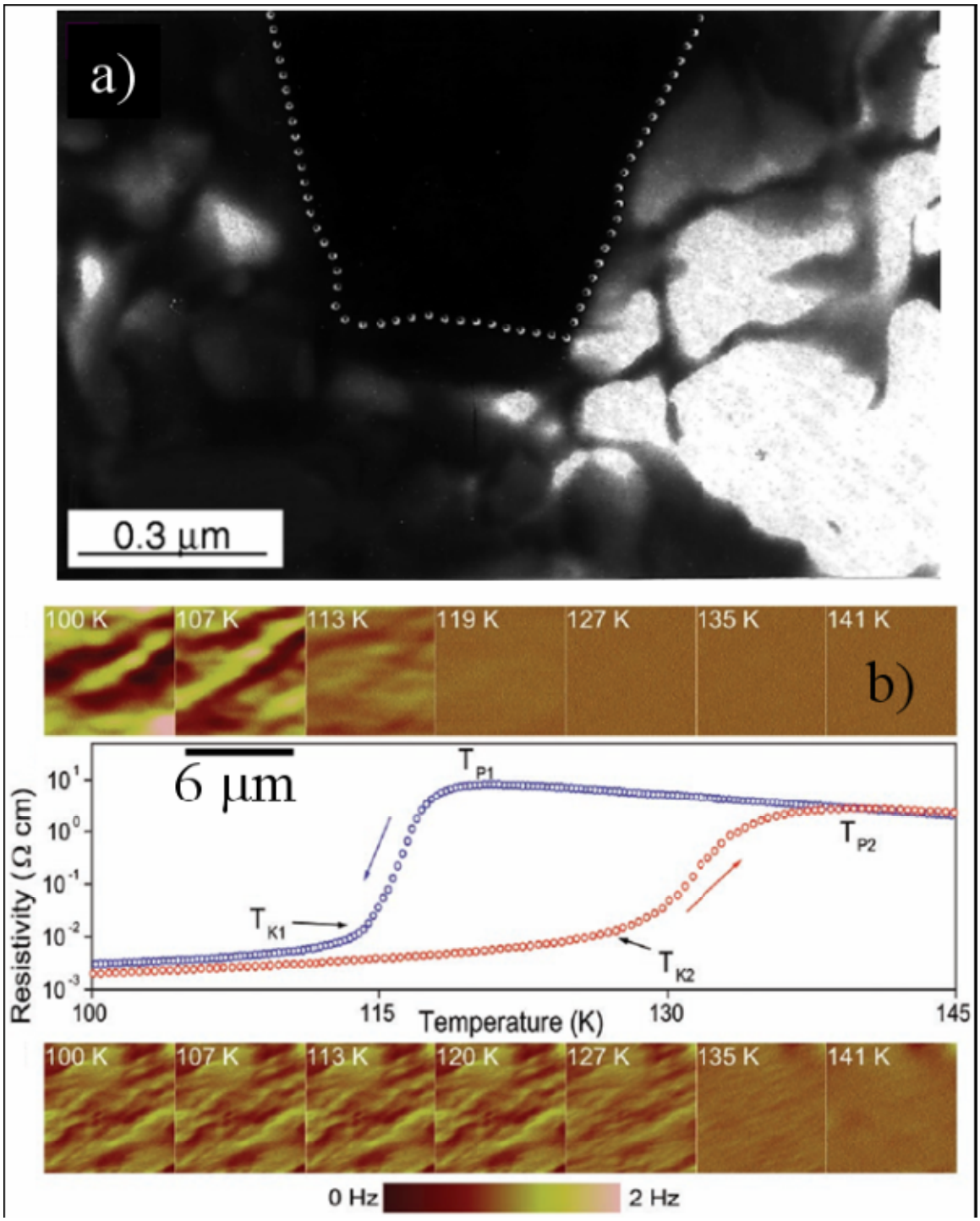

Figure 1-7: Direct observation of electronic phase separation in LPCMO. (a) TEM image of bulk LPCMO showing EPS, taken from ref 20. (b) MFM images showing EPS along with the Resistivity versus Temperature data. Taken from ref [25][25].

The theoretical understanding of such a large scale EPS has been proposed by different research groups, such as quenched disorder[26] and strain[27], although a conclusive understanding of EPS picture is still controversial. Aside from explaining the mechanism, lots of experimental efforts on tuning EPS by external perturbations have been achieved, which will be discussed in the next section.

1.4 External Parameters on Tuning EPS

Due to the strongly correlated nature of electron, orbital, spin and lattice parameters, any change in one or more of these parameters can induce a substantial change in a global manner. Figure 1-8 illustrates some examples on using external perturbation to modulate manganites properties, mostly through transport characterization. The CMR concept is donated as huge resistivity change induced by the magnetic field.[6] The large enough current can also induce a giant resistivity reduction in the system of PCMO, possibly due to heating effect or dielectric breakdown.[28] By means of epitaxial growth of manganites on different substrate, the manganites lattice can be strongly lock to the substrate, causing the effect of strain. The strain can have substantial effect on tuning the electronic ground state between metal and insulator[29] as well as lock the preferential direction of electronic domains.[30] Instead of substrate, a direct mechanical stress applied on bending the film can also shift the metal-insulator transition temperature (MIT) and induce a large scaling factor.[31] Also, applying pressure as high as 11kbar can shift the MIT temperature by changing the Mn-O-Mn bond stretching configuration.[32]

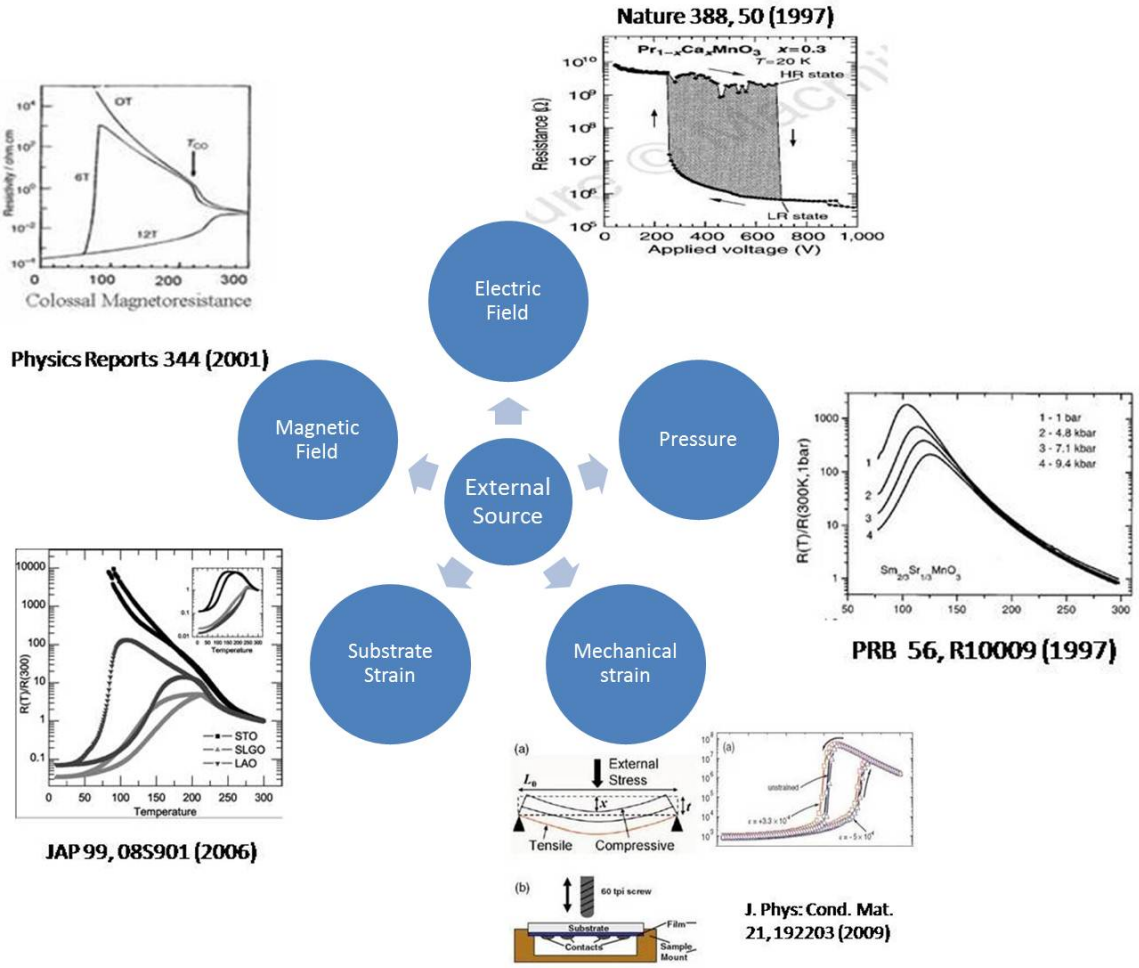

Figure 1-8: external parameters on tuning electronic properties of perovskite manganites.

During my PHD study, most of my focus is on how to use electric field to tune the EPS properties and explore new types of physical mechanism as well as electronic devices, which will be discussed extensively in Chapter 4.

Chapter 2 Experimental Methods

2.1 Overview of Methods

While perovskite manganites exhibit many exotic behaviors, the growth of high quality sample is the first required step to study and discover new properties. While single crystal bulk sample of manganites can be prepared by techniques such as sol-gel method, the requirement of high quality epitaxial thin film on different lattice matched or mismatched substrates. Among many different growth techniques, Pulsed Laser Deposition (PLD) is definitely one of the most promising and popular technique to fabricate high quality thin films.[33] Characterization techniques such as atomic force microscopy, magnetometry, x-ray diffraction and transport measurement are commonly used to study thin film properties.

Even in thin film geometry, the system can be considered somewhat as quasi-two dimensional, it is necessary to shrink the system down to smaller structure. This lies in the fact that in a two dimensional system, if a transport measurement is performed, the electrons will still follow the least resistive path, ignore the high resistive paths such as COI state. By spatially confined the thin film into wire geometry with wire width comparable to the domain size, we are able to study "hidden" regions and discover much interesting phenomena which is missing when probing a two dimensional system.[34–37] Figure 2-1 gives a mimic picture of electrons forcing to pass COI domains in a confined geometry, while in unconfined geometry the electrons are likely to path through metallic states. Thus, the techniques on spatially confining the system to smaller structure are very important on studying new EPS phenomena.

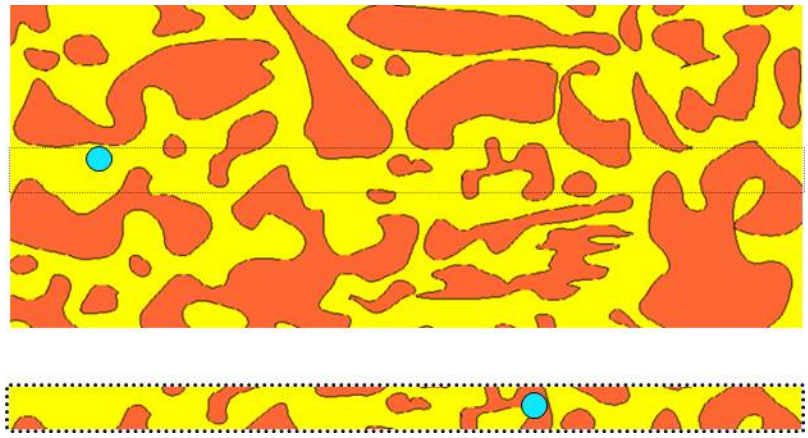

Figure2-1: spatial confinement effect on electronic transport. Red and yellow regions denote COI and FMM domains, respectively. The blue balls represent electrons and the electron in wire geometry is forced to pass COI domains. Taken from ref [37][37].

In this chapter, we will discuss PLD as the main technique for our sample growth. Characterization techniques will be briefly introduced. Different methods of spatial confinement will be discussed, too.

2.2 Pulsed Laser Deposition

2.2.1 Basic Properties

The complex nature of perovskite manganites materials requires a precise control of crystallinity, stoichiometry and morphology of epitaxial thin film. PLD proves itself to be one of the best system on prepare such materials in a thin film manner.

Figure 2-2 shows our typical components of PLD chamber. The KrF Excimer Laser generates laser pulses of wavelength 248nm and duration of about 30ns. The laser penetrates through chamber under vacuum or oxygen background gases and hit the target material. The surface of target material gets activated, generating large amount of atoms, ions and plasmas. These elements interact with background oxygen and reach the substrate. High enough temperature is hold on the substrate through home-made heater so that the arriving adatoms can nucleate, diffuse and form a layer onto the substrate. A Reflection High Energy Electron Diffraction (RHEED) system is always used to monitor the growth process and thin film quality.

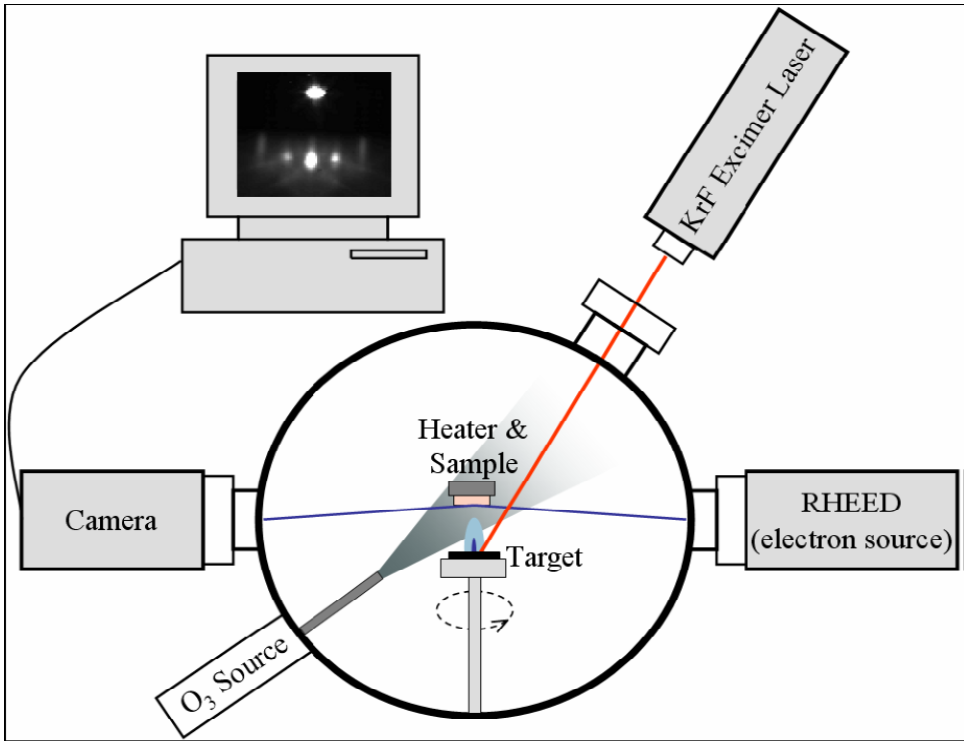

Figure 2-2: Schematic of Pulsed Laser Deposition system.

2.2.2 Target Preparation

We usually make all the targets with different ratio of composition to achieve different doping levels. We first purchase high purity powders with required components and calculate the correct ratios to mix. Take $La_{5/16}Pr_{5/16}Ca_{3/8}MnO_3$ for example, it requires a chemical mixing equation of:

(3)La2O3 + (1)Pr6O11+ (6)CaCO3 + (6)MnO3 = (6)La PrCaMnO3 + (6)CO2 + (10)O2

The calculated proper mass of materials is:

$La_2O_3 \Rightarrow (5/16)\bullet(325.8\ g/mol)\bullet(3\ mol) = 305.4\ g$
$Pr_6O_{11} \Rightarrow (5/16)\bullet(1021.4\ g/mol)\bullet(1\ mol) = 319.2\ g$
$CaCO_3 \Rightarrow (3/8)\bullet(100.1\ g/mol)\bullet(6\ mol) = 225.5g$
$MnO_3 \Rightarrow (1)\bullet(86.9\ g/mol)\bullet(6\ mol) = 521.2\ g$

After careful measurement through high precision scale, the materials are mixed with mortar and pestle for 1 hour until they are in uniform consistency and color. The mixture is then pressed into disk pellets in a solid form and annealed in oxygen environment of about 1.2 atm at 1300 C for 24 hours. A second mixing and annealing process is taken to ensure proper integration of the material. The target then be put into the vacuum chamber and degased by means of laser shots under rotating the target. Such target rotation is necessary during the growth process to ensure uniformity of target surface and preventing particulates ejected.

2.2.3 Reflection High Energy Electron Diffraction (RHEED)

RHEED has become a routine component in any vacuum growth system. In PLD, it is used to monitor the growth features and surface quality. In principle, an electron beam is reflected of the growth sample surface and diffracted, then collected on a phosphor screen. A high resolution KSA-400 camera is used to collect the image from the screen and transfers it to computer which can monitor pixel intensity. RHEED intensity oscillation is usually observed and always reflects as a symbol of layer-by-layer growth, i.e., atoms form one layer of unit cell (u.c.) followed by stacking layers. Figure 2-3 shows several commonly seen growth modes and typically corresponding RHEED patterns. Step-flow growth is characterized by atom directly moving to step edges; 2D growth mode is characterized by 2D nucleation on the terrace and complete for one

monolayer; 3D growth islands is characterized by 3D growth on the terrace and always shows a reduction of RHEED intensity.

Here, in this method section, we will not go deep into the growth modes and how it corresponds to RHEED oscillation and images. This will be discussed extensively in chapter 3 where we construct growth phase diagram in the system of $LaSrMnO_3$.

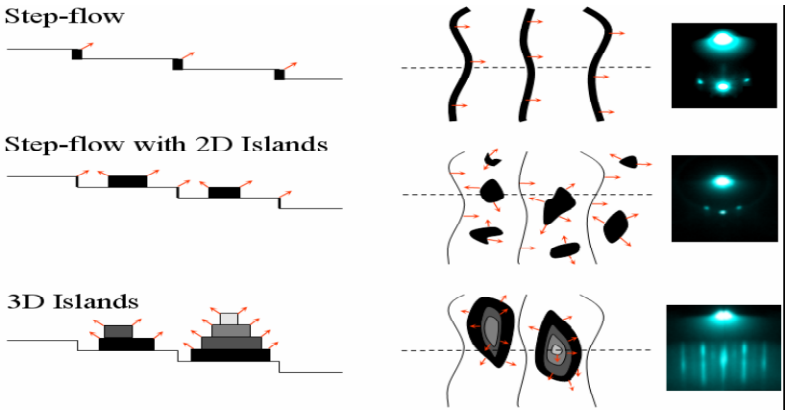

Figure 2-3: Diagram of RHEED data for different growth modes.

2.2.4 Growth Parameters

Temperature, background oxygen pressure and laser fluence are direct tunable parameters experimentally. Any changes in these parameters can alter the growth properties totally. In Chapter 3 we will have comprehensive study on how these parameters change the growth properties.

2.3 Characterization Methods

2.3.1 Atomic Force Microscopy

AFM is a very useful tool on determining film roughness and observing surface morphologies, which strongly related to global properties of the sample.[38] We use room temperature AFM at ambient condition to check our thin film morphologies regularly. In principle, a cantilever with many microns is equipped with a probe tip having a radius of curvature of several nanometers to detect the surface. Figure 2-4 provide a typical block diagram of AFM system setup. When the tip is brought close to the sample surface, the tip interacts with the sample surface through forces and causes a deflection of cantilever. A laser is reflected off of the cantilever's surface and focused on an array of photodiodes. Thus, such deflection can be recorded on a computer.

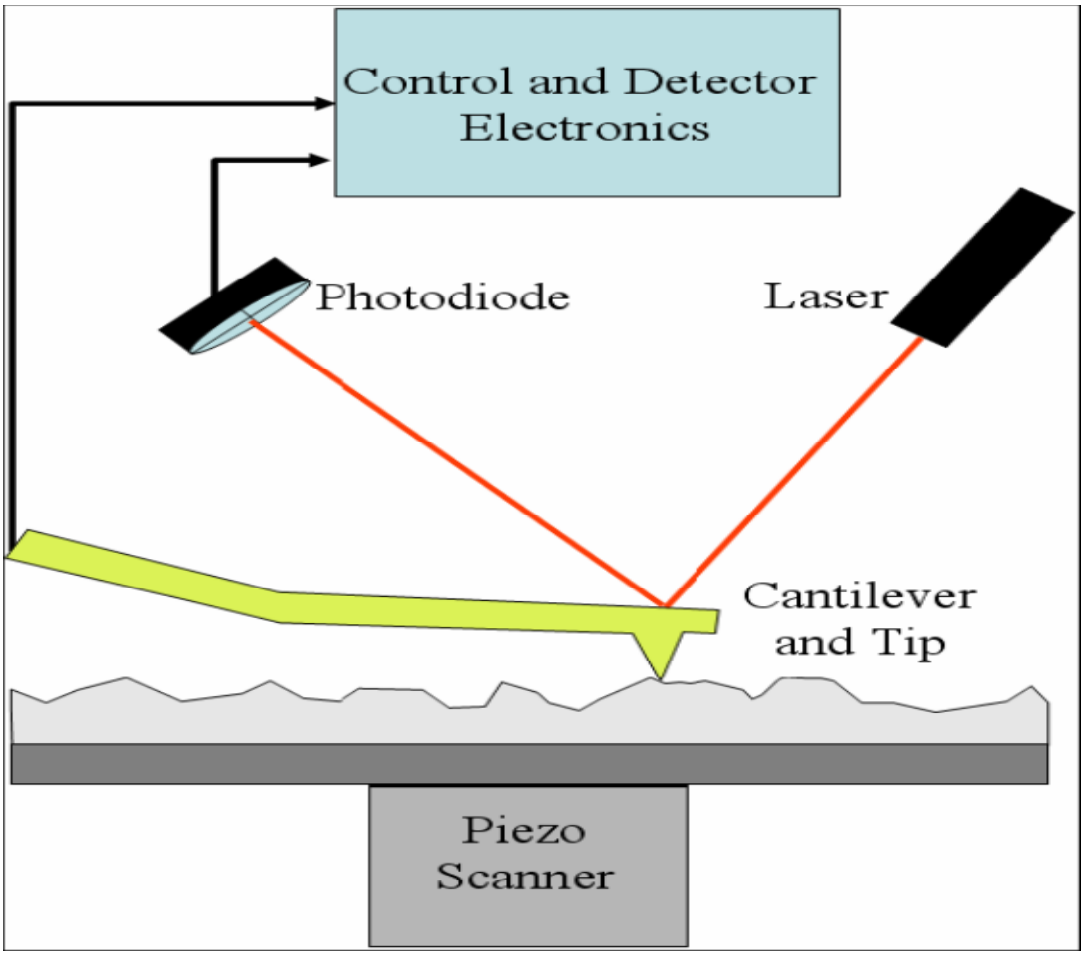

Figure 2-4: Diagram of AFM in contact mode.

The contact mode and tapping mode are often used to scan a sample surface. In contact mode, the static tip is used as feedback signals with usually gives a better resolution on sample morphology. However, it takes the risk that the sample surface will be damaged as well as tip damage since they are in contact each other. Tapping mode is often used on the purpose of getting a rough idea of sample's surface morphologies since

there is no direct contact evolved and the sample-tip distance is normally kept constant. Detailed AFM study on tuning growth parameters will be discussed in Chapter 3.

2.3.2 X-ray Diffraction Technique

XRD is a powerful tool on detecting crystal lattice information as well as thin film crystallinity. The X-rays have wavelength on the same order as crystal lattice spacing, thus making it an ideal tool to study lattice information. The basic principle of XRD is fundamental text book concept of Bragg diffraction, as shown in Figure 2-5. The Bragg's law is defined as $2d\sin(\theta)=n\lambda$ where d is the lattice spacing, θ is the angle between incident x-ray beam and scattering plane, n is integer and λ is the wavelength of incident photon. When the X-ray strikes an atom in the thin film, it reradiates out of the atom as Rayleigh scattering. Following the Bragg's law, the reemitted waves interfere with each other constructively or destructively, thus to reconstruct the crystalline structures. This technique is always known as θ-2θ scans in the x-ray diffraction programs.

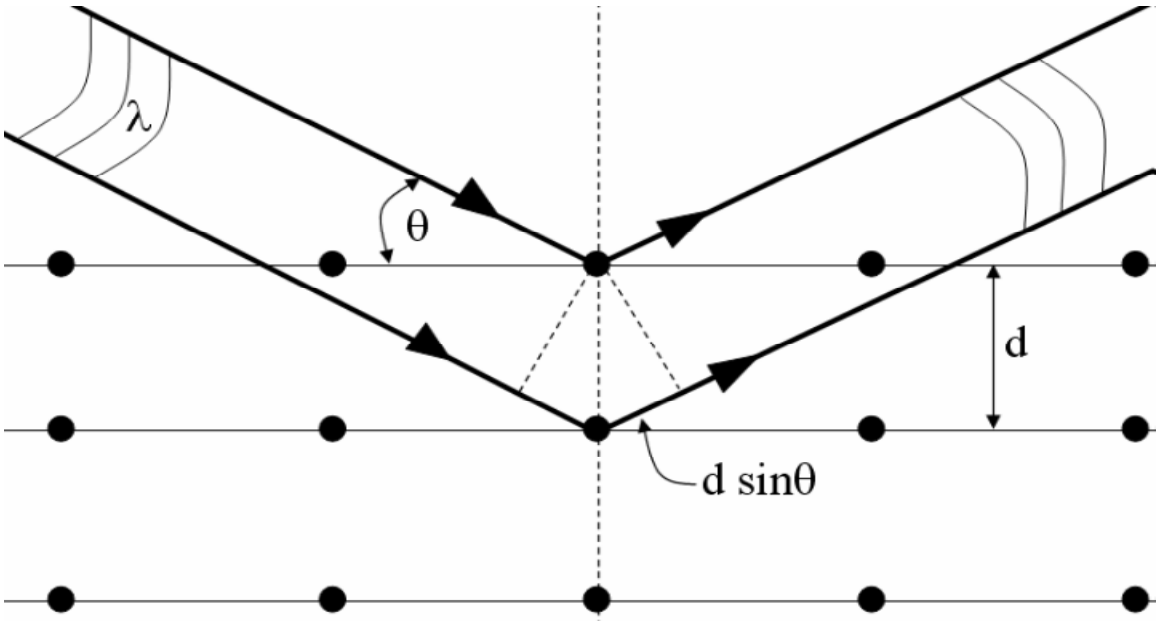

Figure 2-5: Bragg diffraction at sample surface.

Another useful purpose on XRD is known as rocking curve measurement. This is often used to determine the crystallinity of the sample on a large scale. In the ideal case, if the crystal lattices are perfect aligned, a peak with delta function will be observed with no broadening effect. However, it is not the case since the as-grown sample will sometimes have a slight difference of lattice deviation and the crystallized direction. Thus, by "rock" the sample in a small angle around the brag peak angle, one can detect the peak counts and peak width to determine the relative crystallinity of the sample.

2.3.3 Magnetometry

Known the magnetization properties of our thin film is an important piece of information to study the electronic properties. We use a Quantum Design MPMS, known as Superconducting Quantum Interference Device (SQUID) which can apply up to 7T magnetic field, working temperature range from 5K to 400K and sensitivity of 2×10^{-8} emu.

The working principle of SQUID is based on Josephson junctions (JJ), as illustrated from Figure 2-6. JJ consists of an insulating bridge that connects two superconductors.[39] A current will flow and tunnel through the junction when no voltage is applied. A constant driving source current across the junction ring parallel to JJ will give a system in which the current across each junction is equal, thus no voltage reading is available at the counter. Once any value of magnetic flux is applied (sample magnetization), a multiple of the flux quanta $\hbar/2e$ will pass through the ring opening, where $\hbar$ is the Planck's constant and e is the charge of electron. So by linearly changing the flux passing through the ring, the circulating current will react as a sinusoidal function and a change in voltage (current) will be measured by the counter. In this sense, the device is incredibly sensitive to magnetic fields and suitable to detect small magnetization in our thin film samples.

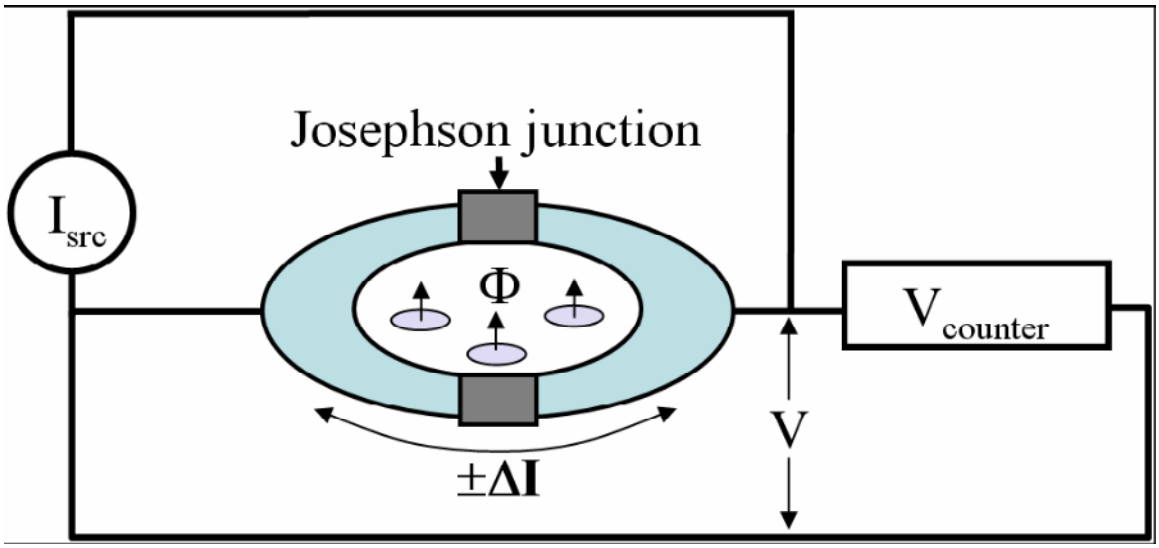

Figure 2-6: DC superconducting quantum interference device.

2.3.4 Transport Measurements

Transport measurements are definitely the key part in my PHD works thus a highly controllable temperature and magnetic field equipment is necessary. Fortunately, our group owns a Quantum Design Physical Properties Measurement System (PPMS) with ever-cooling add-ons. The PPMS can apply magnetic fields up to 9T with a control resolution of 0.03mT from 0T to1.5T and 0.3mT from 1.5T to 9T. The temperature can be stabilized from 1.9K to 400K. A rotator option allows us to rotate our sample with respect to the direction of magnetic field during the measurement. Figure 2-7a shows a PPMS 6000 system.

To ensure that the measuring properties come from the thin film, we usually perform 4-probe resistance measurement, as illustrated in Figure 2-7b. Contact pads

consist of 5nm Ti and 100nm Au is put down using sputtering. The purpose of evaporating Ti can increase the adhesive force between contact electrodes and manganites film. After the contacts are put, a wire bonding machine is used to connect the sample to PPMS sample puck by Al wire. A break-out box is used to connect the external electronics to the sample to lower the noise level and achieve more measurement functionalities.

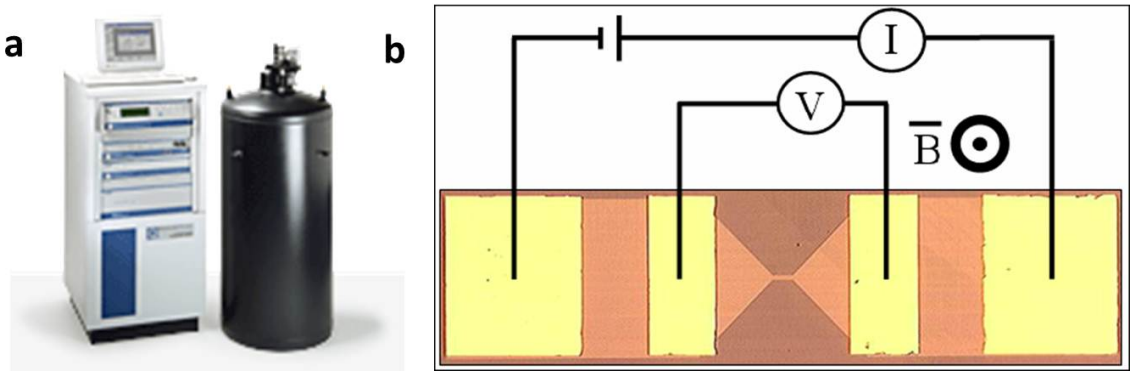

Figure 2-7: electronic measurement. (a) PPMS system consisting a high magnetic field and low temperature dewar and a controlling system. (b) Standard 4-probe measurement.

2.4 Spatial Confinement Techniques

2.4.1 Introduction and Motivation

As mentioned in the introduction, the requirement of shrinking the system down to lower dimension is the tendency towards not only fabricating nano-electronic devices, but also exploring new physics phenomena. As a prototype system, LPCMO offers an opportunity to shrink the system down to micron meter scale to study the confinement behavior. Indeed, several important and exotic phenomena have been reported by means of wet etch lithography[34–37] and focused ion beam etching[40] of LPCMO thin films.

While the submicron scale may be enough for the confinement study in LPCMO, a much broader audience can be attracted by the materials such as LCMO or LSMO which have domain sizes on the order of nanometers. Thus, new fabrication techniques towards smaller dimension and self-organized nanostructures are really important on manganites study.

In this section we will briefly discussed the confinement techniques of wet etch and e-beam lithography.

2.4.2 Photolithography

Photolithography, or known as wet etch lithography, is one of the most popular etching techniques widely used. The advantage of photolithography is its relatively easy accessing, while the drawback lies in that it has spatial limitation about 1um.

The process of photolithography is shown schematically in Figure 2-8. First, sample surface needs to be cleaned by acetone and water. Then, the sample is coated with a layer of micron thick photoresist (PMMA) and warm up to 115 C about 2 min.

Designed mask is put on top of PMMA and exposed under UV light. If positive photoresist (PR) is used, the part of PR which is covered by mask will not change its chemical property while the part of PR which is uncovered by the mask will change its property and easily dissolved in developer. After developer treatment, the required PR will leave on top of manganites to protect it, as shown in step 4 of Figure 2-8. Then, the sample was etched in etchant such as KI for couple of seconds and followed by removal of PR by acetone. Such process can give us a spatial confinement about 1.2um.

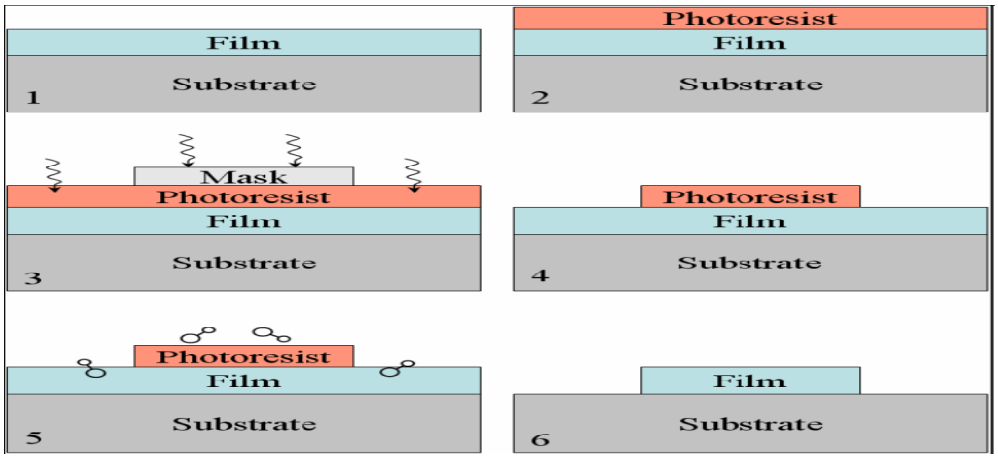

Figure 2-8: Schematic processes of wet etch lithography.

2.4.3 E-beam Lithography

E-beam lithography is becoming more and more popular and required to fabricate smaller structures. The e-beam lithography has similar processes as wet etch except that instead of hard mask, the pattern is written by electron beam. Also, the etching is through high energy milling process rather than chemical etch. As for perovskite manganites, we collaborate with Dr. Philip Rack and Dr. Joo Hyon Noh from Material Science and Engineering Department of University of Tennesse on fabricating small wire structure. Wire width as small as 400nm is successfully fabricated, as shown in the SEM images in Figure 2-9.

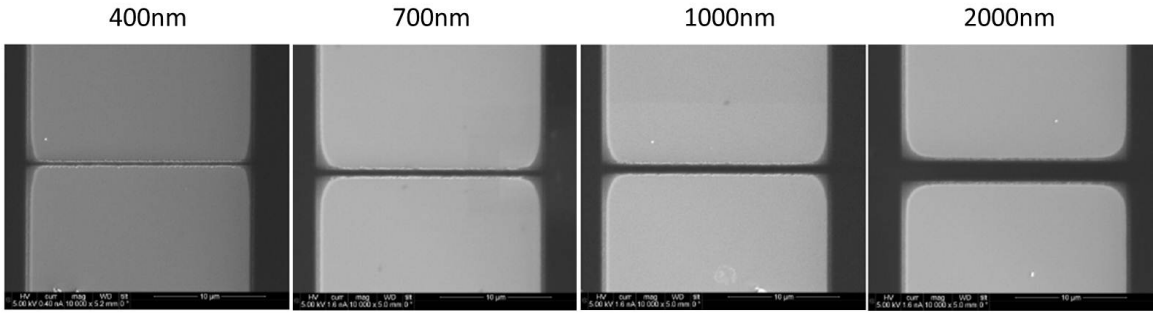

Figure 2-9: LPCMO wires fabricated by means of e-beam lithography.

While the e-beam lithography can shrink the system down to order of hundreds nanometers, a strategy known as Al-assistant fabrication gives us the possibility to further confine the system to about 50nm. The schematics of such method are illustrated in Figure 2-10. The PMMA on top of manganites is first patterned with e-beam lithography, followed by evaporation of Al. The Al will be oxidized in air and Ar ion milling is performed to remove PMMA so that the smaller Al pattern will survive. By etching again, a smaller manganites structure can be achieved.

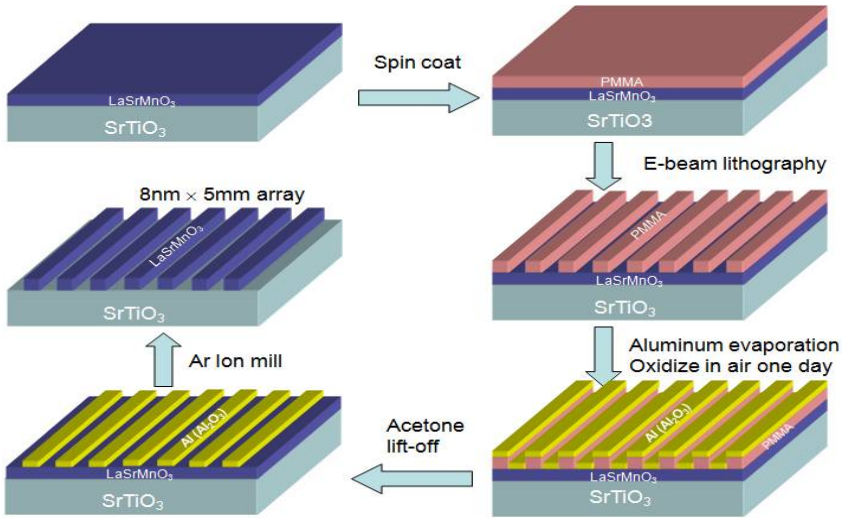

Figure 2-10: Schematics of Al-assistant e-beam lithography.

Chapter 3 Growth Diagram of LSMO Thin Films by PLD

3.1 Introduction and Background

As mentioned previously, thin film epitaxial growth using pulse laser deposition (PLD) has become one of the most popular growth techniques in condensed matter physics because of its versatility and the relatively easy ability to control certain functionalities by varying growth parameters.[33,41–45] However, the physical PLD growth process is far from simple, because it involves multiple complex steps such as ablation of target material, plasma generation and propagation through vacuum or background gas, deposition of ablated atoms on substrate, non-equilibrium processes on the surface such as diffusion, desorption, nucleation and attaching onto existing atomic steps.[46–49] The resulting PLD film growth mode depends strongly on all of these steps, in addition to the consideration of the cohesive energy between the ablated atoms and the binding energy between the atoms and substrate.[47,48] For example, it is well established that the background gas pressure plays an important role in plume collisions while acting to compensate film stoichiometry.[33] It is shown that a high instantaneous deposition rate implies a high supersaturation value that gives rise to a small critical nucleus and thus to a high density of nucleation sites.[33,47] Further, the temperature is known to have a critical influence on the diffusion barrier, which may strongly affect the growth mode. Although various kinds of growth modes have been observed for oxide thin films under different growth conditions[50–52], a growth diagram which combines multiple parameters and builds up a broad picture is still lacking.

In this work, we choose a prototypical system of $La_{0.7}Sr_{0.3}MnO_3$ (LSMO) thin films grown on $SrTiO_3$ (STO) (001) substrates to study the growth properties under different

conditions. This doping of LSMO is a known half-metallic ferromagnet with a critical temperature above room temperature, and is of interest to many different areas, such as spin valves, resistive random access memory (RRAM), etc.[53–56] Theoretically, our focus is on the microscopic processes of adatom *nucleation, step advance* and their influence on the growth properties of oxide thin films. Based on our model analysis, we propose a growth diagram which defines the dependence of surface morphology, crystallinity and stoichiometry of oxide films on the parameters such as supersaturation and temperature. Our experimental observations of the LSMO growth modes under various growth conditions fit in the growth diagram nicely. We emphasize that the concept of supersaturation plays an important role in constructing and understanding growth diagrams for PLD thin film growth of complex oxides.

3.2 Experimental Results

3.2.1 Experimental Conditions

Thin films of $La_{0.7}Sr_{0.3}MnO_3$ were grown on single crystal substrates of $SrTiO_3$ (001) (in-plane lattice mismatch of 0.8%[57]) using PLD with a KrF (λ= 248 nm) laser in an oxygen background containing 10% ozone,[34,37] with the growth pressure of 2 mTorr. The typical film thickness is 10 nm. The repetition rate of the laser is kept at 1 Hz. *In-situ* high-pressure Reflection High Energy Electron Diffraction (RHEED) is used to monitor the entire deposition process. The time dependence of the intensity of the specular reflection was recorded. Here we employ the Pulse Laser Interval Deposition technique (see Ref. [2]), i.e. the growth periods are separated by the annealing periods (typically 5 min) in which laser pulses are paused. Specifically, the laser is paused every time when

the RHEED intensity reaches a local maximum to allow sample annealing which manifests itself as the upturn of RHEED intensity. The laser pulse is resumed when the RHEED intensity saturates. The laser fluence was varied between 1 and 4 J/cm^2. The substrate temperature was varied from 650 to 840 ^{o}C. The substrates are treated by buffered-HF and pre-annealed in O_2 (1 atm) for 3 hours at 950 ^{o}C. The target-substrate distance was 4 cm. The RHEED images were taken using KSA-400 camera at exposure time of 667 ms at the end of the growth. *Ex-situ* Atomic Force Microscopy (AFM) is used to obtain details of surface morphology. X-ray diffraction (XRD) experiments are conducted to measure the crystallinity of the films. Energy-dispersive X-ray spectroscopy (EDX) is carried out to analyze the chemical composition.

3.2.2 Temperature Dependence of Thin Film Properties

We first study the influence of growth temperature while fixing the background oxygen pressure and the laser fluence at 1J/cm^2. Figure 3-1a shows AFM and RHEED images of the pretreated $SrTiO_3$ substrates. Flat surfaces with terrace width of approximately 300 nm are obtained. The sharp RHEED pattern also indicates the presence of flat terraces and a good surface crystallinity. Figure 3-1b and 3-1c show the *ex-situ* room temperature AFM, RHEED oscillations and *in-situ* RHEED images at growth temperature of 720 ^{o}C and 776 ^{o}C, respectively. In Figure 3-1b, for the sample grown at 720 ^{o}C, the single layer terraces inherited from the substrate are still visible while many sub-monolayer-height islands exist on top of each terrace. The RHEED intensity can only maintain its initial level for the first several oscillations, after which it decreases upon further growth. The final RHEED pattern shows weak intensity contrast,

although no extra diffraction spots are present. The room temperature AFM data indicates that the growth mode is still layer by layer at 720 ^{o}C, with a RMS roughness of only 0.14 nm. The measured X-ray Diffraction rocking curve shows the full width of half maximum (FWHM) of 0.046^{o}, compared to 0.039^{o} for a well-crystallized film. These features suggest that the film surface is poorly crystallized with layer-by-layer feature preserved. In Figure 3-1c, the room temperature AFM image of the sample grown at 776 ^{o}C reveals neither regular terraces nor steps from the substrate and has rms roughness of 0.45 nm. The RHEED intensity decreases during the growth and displays a weak pattern with extra spots, indicating 3D island formation. For sample grown at 840^{o}C, as shown in Figure 3-1d, totally different features are present. Rod-like structures (as high as 100 nm) are clearly visible in the AFM image. EDX experiments were conducted to investigate the stoichiometry of these features. Figure 3-1d shows the Mn-Kα and O-K spectroscopy maps. The Mn and O concentrations of the film and the rod are different, indicating chemical phase separation occurs in this growth regime resulting in different stoichiometry of the rods as compared to the film. As shown in Table 1, a semiquantitative analysis[58] indicates that the Mn:O composition ratio is roughly 1:1 on the rod and 1:3 on the film. The Sr concentration is hard to determine due to large background from the STO substrate. We cannot resolve the La concentration due to its proximity to the substrate Ti peak. According to the data in TABLE 3-1, the composition on the rod is likely to be MnO due to the high vapor pressure of Sr and chemical bond stability of MnO.[59]

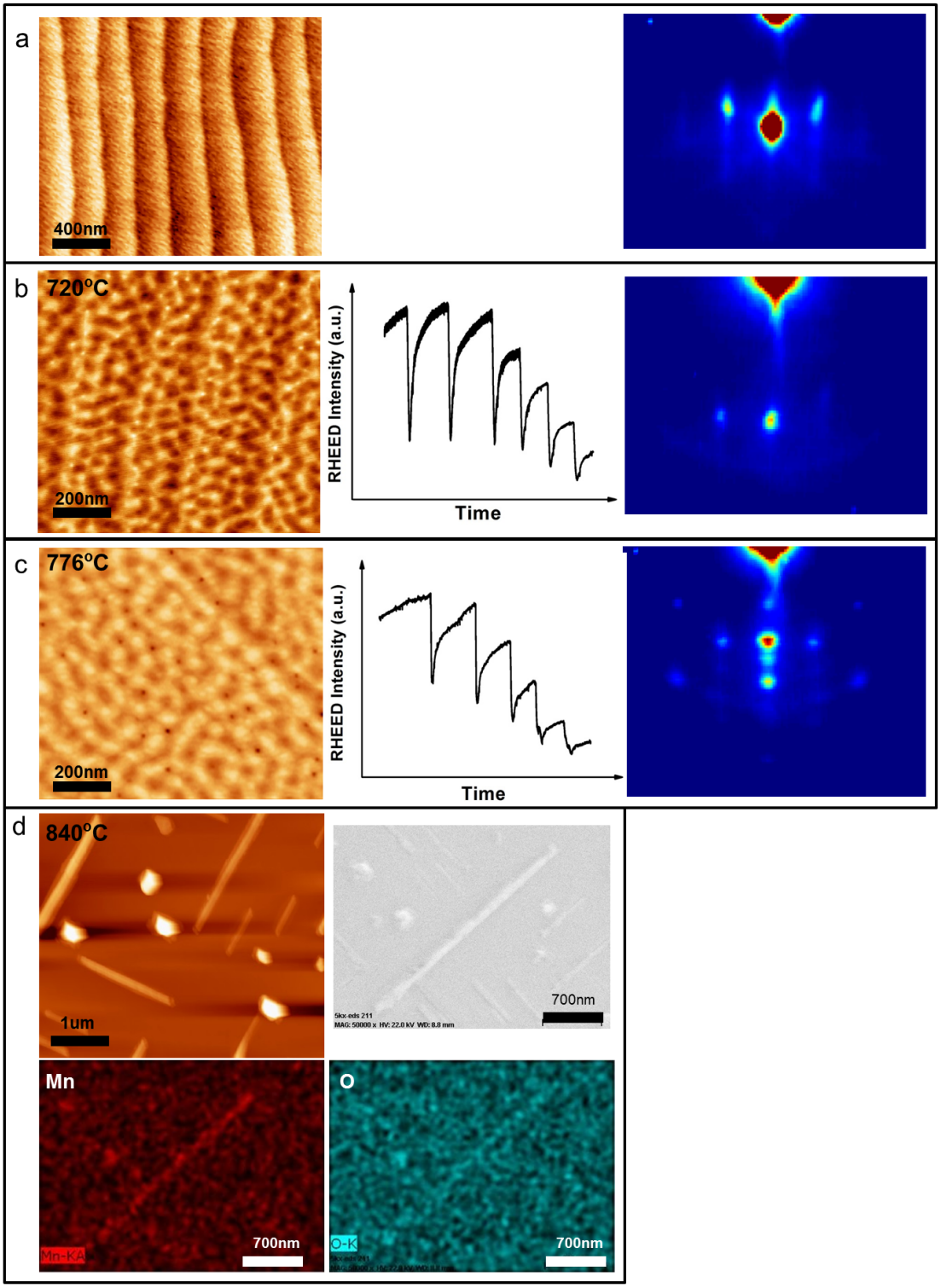

Figure 3-1: Temperature dependence of growth properties at laser fluence of 1J/cm^2. (a) AFM image (left) and RHEED image (right) of $SrTiO_3$ (001) substrate. (b), (c) AFM, real-time RHEED oscillations and RHEED images of samples grown at 720 ^{o}C and 776 ^{o}C under 1J/cm^2 laser fluence. (d) AFM (upper left) and SEM (upper right)

images of sample grown at 840 ^{o}C under 1J/cm^{2} laser fluence. Mn (lower left) and O (lower right) EDX spectroscopy are shown corresponding to SEM image area.

	Counts of film	Counts of film and rod	Counts of rod	Standard Relative Intensity	Counts of rod normalized with standard intensity
Mn(Kα)	52	120	68±9	150	0.45±0.06
O(K)	470	529	59±22	151	0.39±0.14

Table 3-1. EDX analysis of non-stoichiometric sample (840 ^{o}C, 1J/cm^{2}).

The temperature dependence of growth mode has also been investigated at different laser fluence of 4J/cm^{2}. As shown in Figure 3-2a, sample grown at 660 ^{o}C have layer-by-layer features (AFM and RHEED images will be discussed in Section II-C). The sample grown at 760 ^{o}C shows a completely different morphology. In Figure 3-2(b)-(d), a 3D growth mode is revealed in both AFM and RHEED images. At first, the maximum intensity of primary RHEED spot gets weaker with each oscillation, then it remains nearly unchanged with almost no oscillations. The RHEED pattern shows spots with a strong intensity, indicating a well crystallized, 3D growth mode.

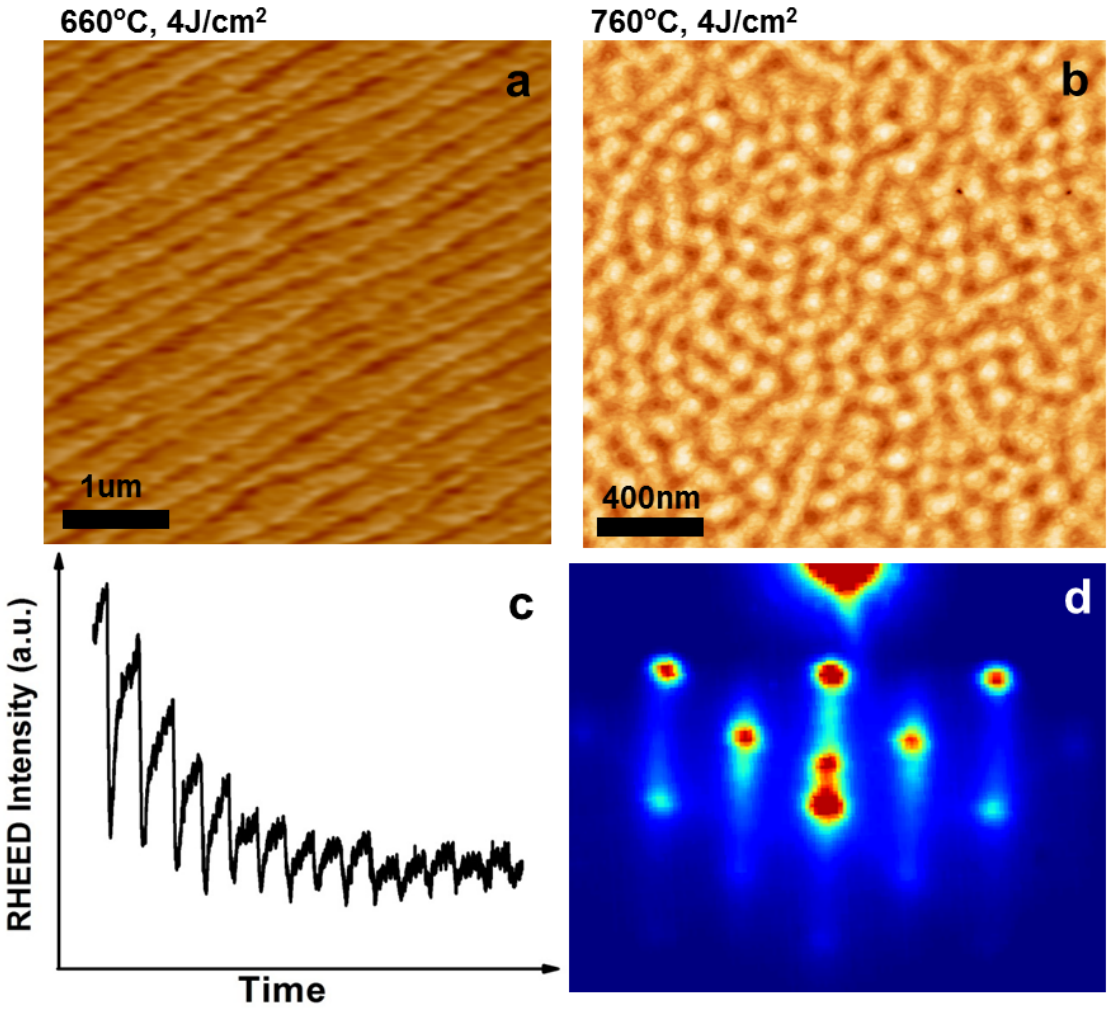

Figure 3-2: Temperature dependence of growth properties at laser fluence of 4J/cm^2. (a), (b) surface morphologies of samples grown at 660 ^{o}C and 760 ^{o}C. (c), (d) corresponding RHEED oscillations and image of sample in (b).

3.2.3 Pressure Dependence of Thin Film Properties

Next, we tune the background oxygen pressure while keeping the temperature (730 ^{o}C) and laser fluence (1 J/cm^{2}) constant. A tube was installed with its end close to the sample surface to supply an oxygen gas pressure during the growth process. To ensure the same laser and temperature conditions, we use a larger substrate (5mm×8mm) and carefully position the oxygen tube nozzle with respect to the sample to create a pressure gradient over the surface of one sample. Similar approach has been used to create temperature gradient by other authors.[60] As shown in Figure 3-3a, a 3D growth mode is obtained at low oxygen pressure, while flatter films are visible at higher pressure. In Figure 3-3b, we show the rms roughness of the entire film area as measured by *ex-situ* AFM. It is clearly seen that the rms roughness decreases with the direction of increasing local pressure. To verify that the roughness distribution does not originate from temperature variations due to the large substrate size, we moved our substrate by 1 mm laterally with respect to the oxygen tube and grew a sample under the same conditions. We find that the rms roughness distribution on the sample correspondingly shifts by about 1 mm, which excludes temperature non-uniformity effects as the cause for the observed surface roughness distribution.

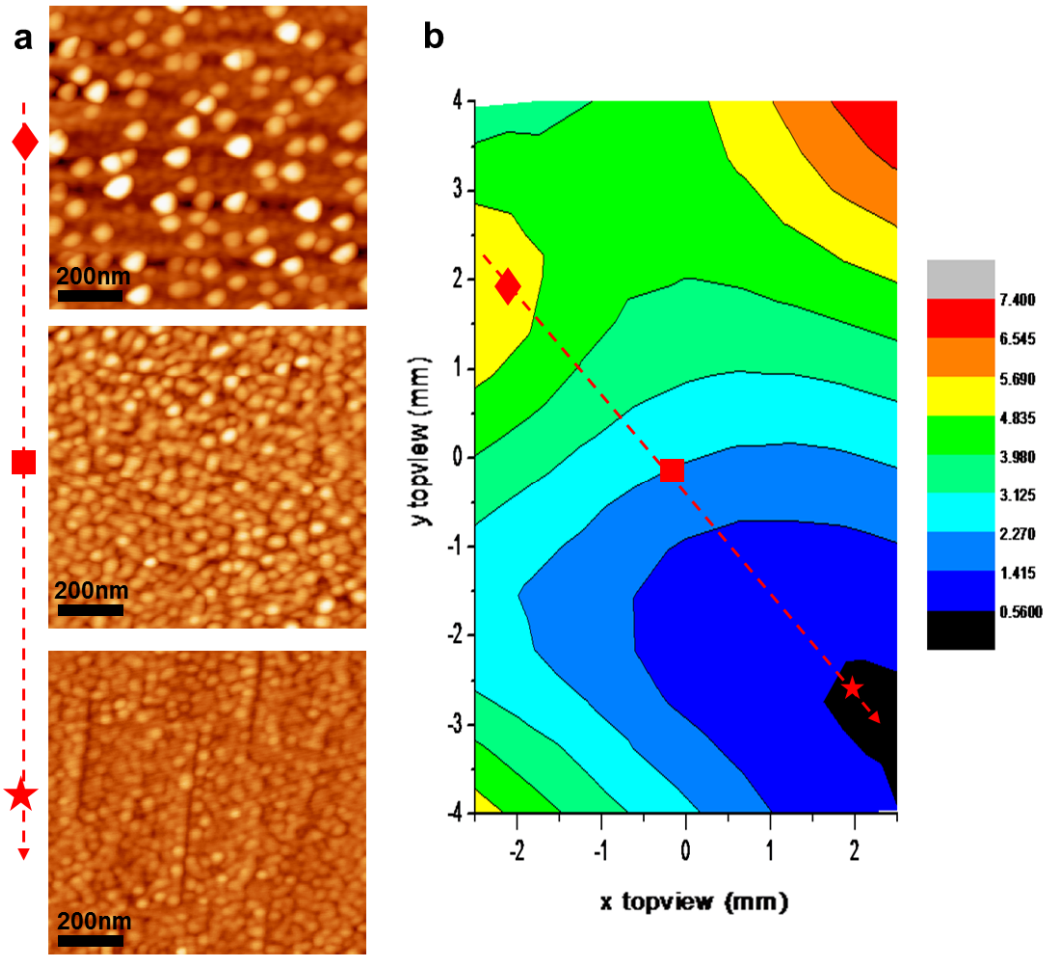

Figure 3-3: Oxygen pressure dependence of thin film morphologies. (a) growth pressure dependence of surface morphology under growth temperature of 730 ^{o}C and laser fluence of 1J/cm^{2} . (b) surface roughness (in unit of nm) map of the sample under oxygen pressure gradient. The dashed arrow indicates the direction of increasing local pressure.

3.2.4 Laser Fluence Dependence of Thin Film Properties

In addition to the temperature and the oxygen pressure, the pulsed laser fluence is another important parameter to control the film quality. Here we keep the temperature at 740 ^{o}C and increase the laser fluence from 1 J/cm^2 to 2.2 J/cm^2. Dramatic changes are observed in the film growth as shown in Figure 3-4a and 3-4b. In Figure 3-5, The sample grown at 1 J/cm^2 shows 3D features with FWHM of 0.050^{o} in the rocking curve, which indicates the poorly-crystallized nature. The sample grown at 2.2 J/cm^2 indicates a layer-by-layer growth mode with FWHM of 0.039^{o}. According to Figure 3-4c and 3-4d, perfect oscillations as well as good RHEED patterns are observed, both indicating good surface morphology and crystallinity.

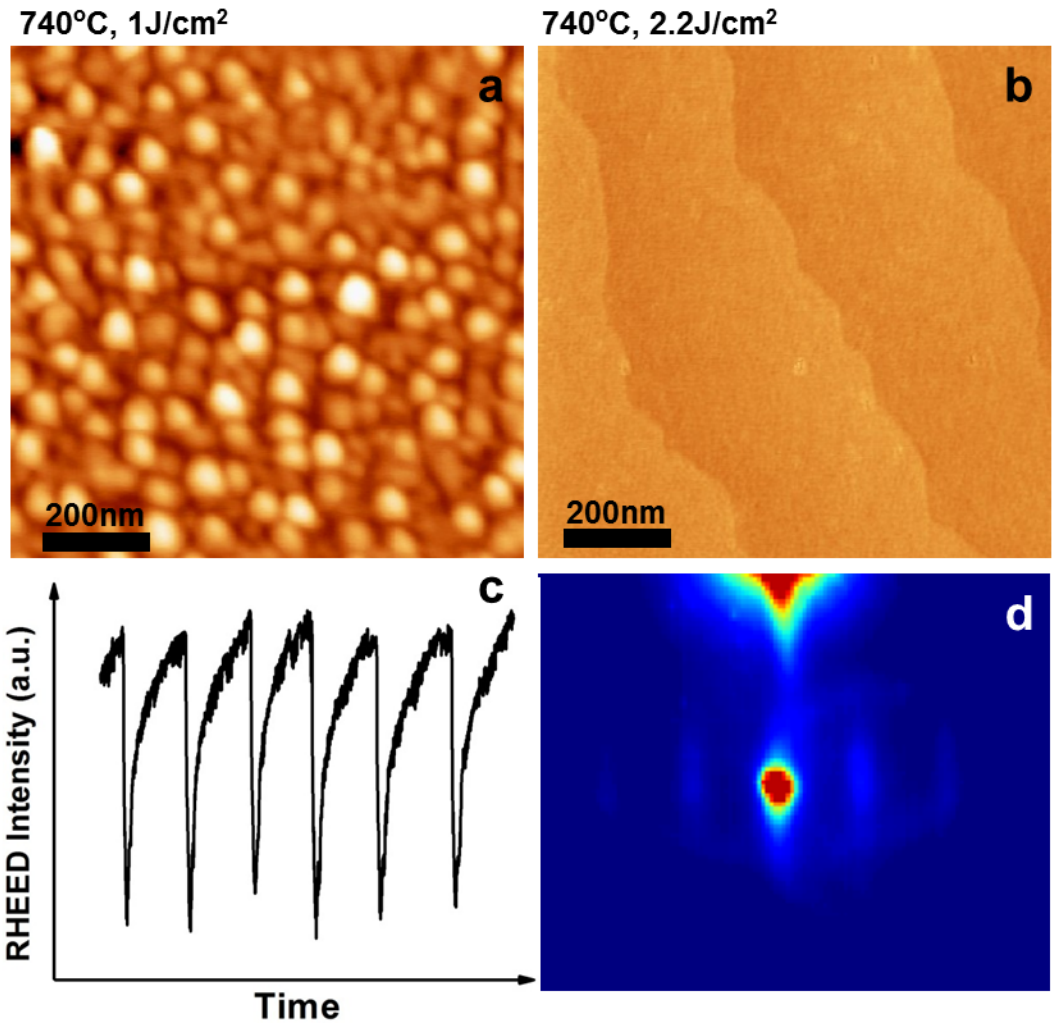

Figure 3-4: Laser fluence dependence of samples. Samples grown at (a) 1J/cm^2 and (b) 2.2J/cm^2, both under growth temperature of 740 ^{o}C. (c), (d) corresponding RHEED oscillations and image of the sample in (b).

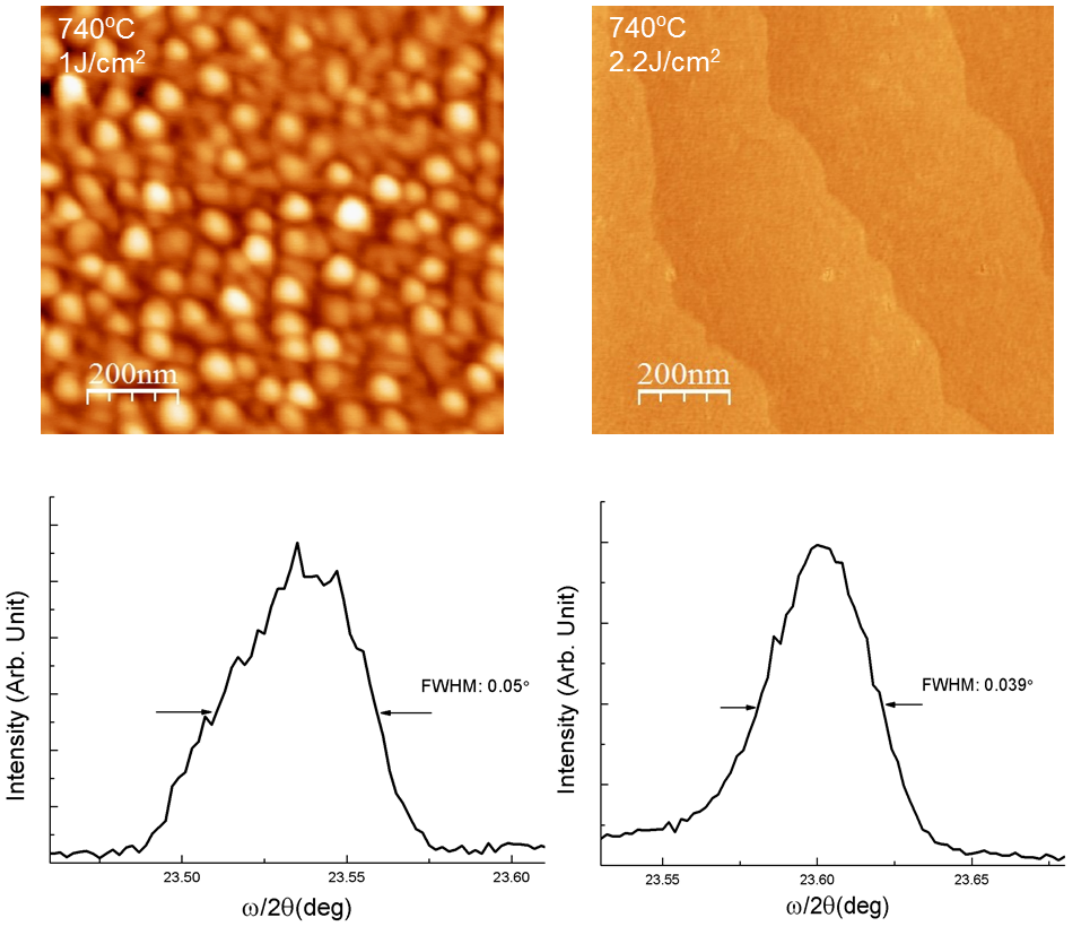

Figure 3-5: AFM images and their corresponding rocking curve of (002) peak.

3.2.5 Annealing Effect on Thin Film Properties

Another experimental distinction of multilayer poorly-crystallized and multilayer well-crystallized features of the thin film sample is in use of post-annealing process. As shown in Figure 3-6, a poorly crystallized surface is obtained as-grown. After annealing

the sample in O_2 at 700 ^{o}C for 3 hours, a much more flat and well-crystallized film is achieved.

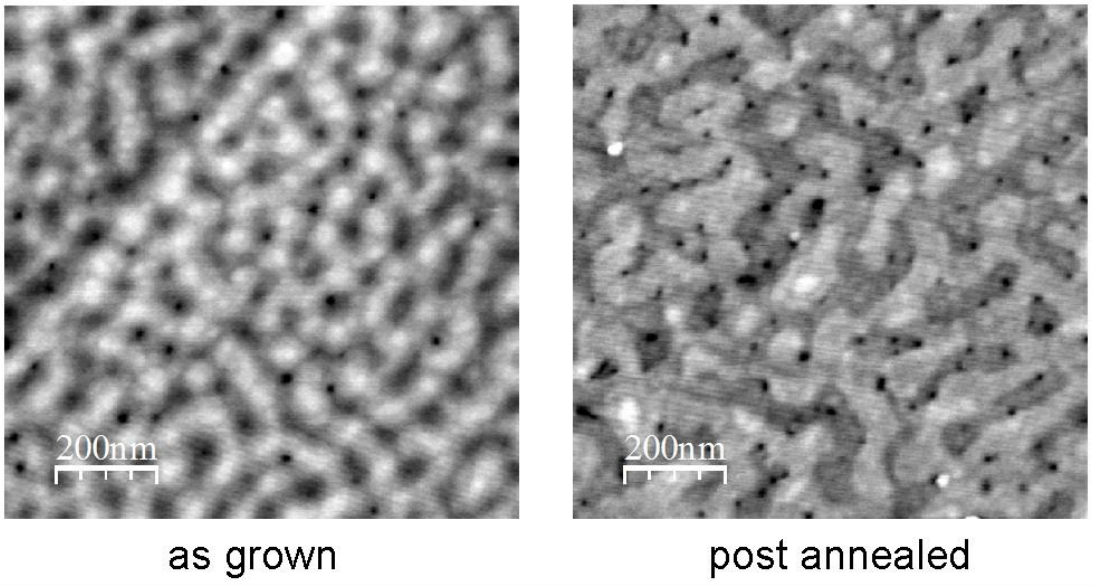

Figure 3-6: comparison on surface morphologies of as-grown sample (left) and the same sample annealed in O_2 at 700 ^{o}C (right).

3.3 Theoretical Results

3.3.1 Introduction and Overview

As a starting point, the change in surface energy $\Delta\sigma = \sigma + \sigma_i - \sigma_s$ is widely adopted to analyze observed surface morphology, where σ, σ_s and σ_i denote the surface energy of the depositing layer, the underlying layer and the interface energy, respectively.[49] Indeed, such analysis lies in the core of the origin of the well-known crystal growth mechanisms such as Volmer-Weber (VW)[61], Frank-van der Merwe (FM)[62] and Stranski-Krastanov (SK)[63] growth. When $\Delta\sigma < 0$, layer-by-layer growth mode (FM) is favored; while 3D islands or 3D growth mode (VW) is preferred when $\Delta\sigma > 0$. The SK growth mode represents a transition from 2D to 3D growth when the lattice strain is taken into account. However, this description of growth is oversimplified. For example, even for $\Delta\sigma > 0$, it is still possible to achieve layer-by-layer growth.[49] As seen above, by tuning experimental parameters, different varieties of surface morphology, surface crystallinity and stoichiometry have been observed. As shown in Fig.5a, the microscopic growth process involves multiple steps, more than the picture of surface energy change. Moreover, what also needs to be described is the relation between the growth conditions and the crystallinity and the stoichiometry of the films. Note that the discussion of stoichiometry is even beyond the picture of Fig. 5a where the smallest components are the unit cells.

The boundaries of 2D and 3D growth have been discussed in the literature. For example, Metev et al. considered the mean film thickness of a 99% covered substrate and its dependence on the growth temperature and deposition rate.[33,64] The boundary between

a low-island growth mode and a high-island growth mode was defined in terms of the deposition rate and growth temperature. It was shown that a high deposition rate and a low growth temperature favored a 2D growth mode. By comparing the timescale of diffusion and laser pulse interval, W. Hong et al.[50] have constructed the boundary between step-flow growth and 2D island formation.

The crystalline properties of $SrTiO_{3-\delta}$ homoepitaxial thin films have been reported by Ohtomo and Hwang[51] The growth phase diagram in terms of O_2 pressure and temperature has been studied. It is noted that at the high temperature and low pressure region, the mismatching between crystallization and oxidation timescale gives rise to irregular *nucleation* and growth cycle.

Here, we applied the theoretical treatment in Ref. [10] on the PLD growth of oxide thin films, i.e. 1) to consider the factors of particle exchange and energy barrier in nucleation to account for the crystallization; 2) to consider the rate of *step advance* not only in terms of the diffusion process, but also the adatom concentration and their spatial gradient on the surface which all play important roles in determining the boundary between 2D and 3D growth modes. In addition, the film stoichiometry is described using the supersaturation of the corresponding vapor to solid process.

Here we first focus on the discussion on the temperature dependence of the nucleation process which strongly affects the crystallinity of thin films. Then, we focus on the discussion on the competition between *nucleation* and *step advance* (the growth of 2D islands and advance of steps), which determines the boundary of layer-by-layer and 3D growth. A growth phase diagram is developed based on those discussions in terms of growth temperature and supersaturation which is a useful concept in describing the

growth conditions. Our experimental findings and theoretical model are compared to test the feasibility of our growth diagram.

3.3.2 Nucleation

During PLD growth, the laser ablation generates a large atomic flux. As seen in Figure 3-7(a), these incoming atoms become adatoms on the substrate surface and diffuse. Some coalesce and become nuclei. At low laser repetition rate,[65] to form small nucleus on top of a surface, the chemical potential of the vapor phase has to overcome a barrier due to the fact that the small nuclei have higher energy per atom than their bulk counterpart. For 2D nucleation: the change of the Gibbs free energy for forming such a square nucleus is

$$\Delta G = -\frac{l^2}{S_C}\Delta\mu + l^2\Delta\sigma + 4l\chi \tag{1}$$

$$\Delta\sigma = \sigma + \sigma_i - \sigma_s \tag{2}$$

where l is the length of the nucleus, Sc is the area of the unit cell, σ is the surface energy of the 2D nucleus, σ_i is the interface energy between the nucleus and the underlying layer and σ_s is the surface energy underneath the nucleus and χ is the edge energy per unit length.

The maximum value of ΔG with respect to the length l is the barrier:

$$\Delta G^* = \frac{4\chi^2 s_c}{\Delta\mu - s_c\Delta\sigma} \tag{3}$$

Correspondingly, the critical length for the maximum ΔG is

$$l^* = \frac{2\chi s_c}{\Delta\mu - s_c\Delta\sigma} \tag{4}$$

The nuclei smaller than this size will decay and those larger than this size will grow.

Because of this barrier, and the dependence on the number of adatoms and their diffusion length, the speed of 2D nucleation takes the form:

$$J_{nuc} = f(\Delta\mu, T)\exp\left(-\frac{H(\Delta\mu)}{kT}\right) \tag{5}$$

$$f(\Delta\mu, T) = 2\sqrt{s_c}arN_0\left(\frac{\Delta\mu - s_c\Delta\sigma}{\pi kT}\right)^{1/2} \tag{6}$$

$$H(\Delta\mu) = \frac{4\chi^2 s_c}{\Delta\mu - s_c\Delta\sigma} - (E_{des} - E_{sd}) \tag{7}$$

where s_c is the area of the surface unit cell; a is the lattice constant; N_0 is the density of adsorption sites; χ is the step edge energy per unit length; *r* is the arrival rate which is proportional to the concentration of adatoms; *k* is Boltzmann constant; E_{des} and E_{sd} are the desorption and diffusion energy barriers. $\Delta\mu$, known as supersaturation, is the chemical potential difference of adatoms transitioning from their quasi-vapor phase (the mobile adatoms on the surface and the background oxygen in the gas phase) near the substrate to their solid phase on the substrate.

The factor $f(\Delta\mu,T)$ can be considered as an effective Zeldovich factor which accounts for the deviation of the system from the equilibrium state; it describes the rate of atom exchange between the nuclei and its quasi-vapor parent phase. The factor $H(\Delta\mu)$ denotes the energy barrier of the *nucleation*. The competition between $f(\Delta\mu,T)$ and

$\exp(-H(\Delta\mu)/kT)$ as a function of temperature results in a maximum value of *nucleation* rate:

$$T_{nuc}^{m} = H(\Delta\mu)/2k \tag{8}$$

When the sample temperature is low, the *nucleation* rate is low because it's difficult to overcome the *nucleation* energy barrier. At the same time, the effective Zeldovich factor is relatively high, indicating a low atom exchange rate between gas and solid. Thus, the *nucleation* rate is low and the films are not well crystallized. When the temperature is high, the *nucleation* rate is limited due to a low Zeldovich factor. However, it is easier to overcome the *nucleation* energy barrier to form nuclei. Thus, the films are well crystallized although the *nucleation* rate is also low. Consequently, Eq. (8) divides the poorly crystallized and well crystallized growth modes, as illustrated in Figure 3-7(b).

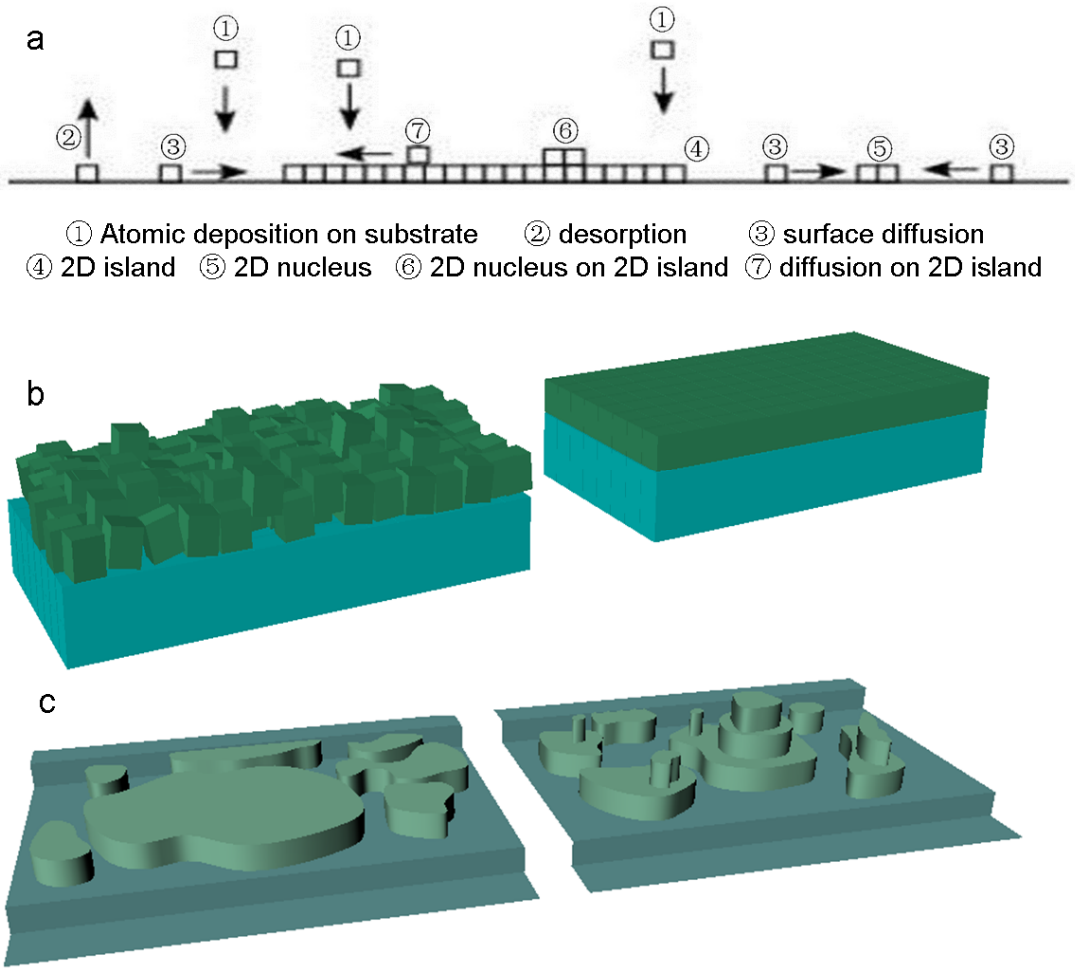

Figure 3-7: Microscopic illustration of the growth processes. (a) Schematic diagram of the atomic process in the deposition. (b) Schematic of the poor crystalization (left) and the good crystalization (right). (c) Schematic of the 2D layer-by-layer growth and the 3D growth.

3.3.3 Diffusion and Step Advance

As shown in Figure 3-7(a), besides *nucleation*, another way for adatoms to contribute to the film growth is to attach to existing nuclei or steps causing *step advance*. The process includes the surface diffusion of adatoms towards the steps or edges of nuclei and incorporation of the adatoms into the kinks.

The density of atoms adsorbed on the surface n_{ad} (mostly the case 3 in Figure 3-7(a)) is proportional to the atom arrival rate r and the adsorption time of the atoms. Therefore,

$$n_{ad} \propto r\tau_{ad} \tag{9}$$

given that the sticking coefficient is unity, which is the case for high energy incoming atomic flux.

The life time of the adatoms τ_{ad} is the time between the adsorption and the desorption which involves overcoming an energy barrier E_{des}, as shown in Figure 3-8. Therefore

$$\tau_{ad} = \frac{1}{\nu}\exp\left(\frac{E_{des}}{kT}\right) \tag{10}$$

where ν is the vibrational frequency of the adatom.

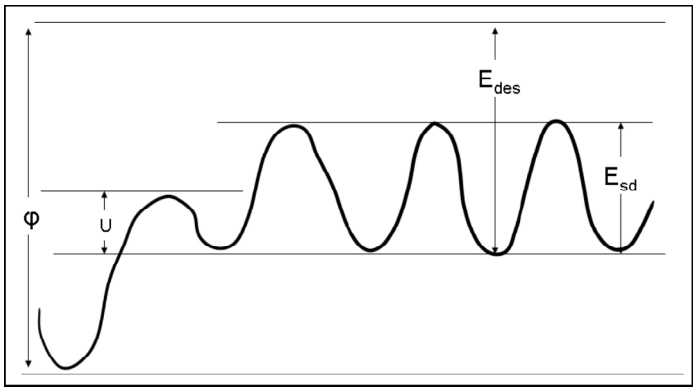

Figure 3-8: Energy potential plot. φ: energy potential for kink position; E_{des}: desorption energy; E_{sd}: surface diffusion potential; U: energy barrier for attaching to kink position.

During the lifetime of an adatom, it moves along the surface according to the thermal fluctuation, or random walk, i.e. diffusion. The diffusion coefficient is

$$D_{sd} = a^2 \nu \exp\left(-\frac{E_{sd}}{kT}\right) \tag{11}$$

where a is the lattice constant and E_{sd} is the diffusion energy barrier (Figure 3-8). Therefore the diffusion length is given as

$$L_{sd} = \sqrt{D_{sd}\tau_{ad}} = a \exp\left(\frac{E_{des} - E_{sd}}{2kT}\right) \tag{12}$$

The speed of step advance involves two processes. First, an adatom moves to a step kink by diffusion, the rate is described as the mean distance L_{sd} divided by the mean residence time τ_{ad}

$$V_d = \frac{L_{sd}}{\tau_{ad}} = a\nu \exp\left(-\frac{E_{des} + E_{sd}}{2kT}\right) \tag{13}$$

Second, the adatoms overcome an energy barrier to attach to the step kink (Figure 3-8), the rate of which can be described as

$$V_{sk} = \frac{a^2 \nu}{\delta_0} \exp\left(-\frac{U}{kT}\right) \tag{14}$$

where δ_0 is the mean distance between step kinks and U is the energy barrier for adatom to attach on a step kink. Because in most cases $E_{des} + E_{sd} >> U$, the rate of step advance is limited by the diffusion process.

Assuming that the growth is in the diffusion region, i.e. the diffusion process is the limiting factor of step advance, the rate of step-advance can be written in the form of[49]

$$V_{sa} = 2a\nu \frac{\Delta\mu}{kT} \exp\left(-\frac{\varphi - (E_{des} - E_{sd})/2}{kT}\right) \tag{15}$$

where ν is the vibrational frequency of the adatom; φ is the adsorption energy at the kink position. We note that similar to *nucleation*, the rate of step-advance is also a function of supersaturation and temperature.

3.3.4 Growth Phase Diagram

The annealing process used in this work for each monolayer helps to reach layer by layer growth in the later stage of a monolayer deposition. For example, the small nucleation on top of 2D islands may become unstable due to the lowered supersaturation without laser pulses and decompose into adatoms which eventually attach to the step edges of the lower layer via interlayer mass transfer. Thus, the processes at the early stage of a monolayer deposition such as *nucleation* and surface migration of the adatoms are more important to determine the growth properties.[2] In such case, the competition between the *nucleation* rate and the *step advance* rate becomes a crucial factor to

determine the growth mode. As illustrated in Figure 3-7(c), if the *nucleation* rate J_{nuc} is much higher than the rate of *step advance* V_{sa}, new nuclei can form on top of existing islands before the completion of the underlying layer. In turn, several layers can grow simultaneously, causing 3D growth. Such a growth mode induces a reduction of the peak intensity of RHEED oscillation. In the other case, if the *nucleation* rate is much lower than the rate of *step advance*, new nuclei will form after most of the underlying layer is filled, which gives rise to a layer-by-layer growth mode.

To compare the timescales, we calculate:

$$t_{layer} = \frac{L}{v_{sa}}; \tag{16}$$

$$t_{nuc} = \frac{1}{J_{nuc} L^2} \tag{17}$$

where t_{layer} denotes the time to completely cover the substrate terrace with width *L* (the upper limit of the distance of the step advance) by one monolayer via *step advance*; t_{nuc} denotes the time to form one nucleus on the same substrate terrace.

The boundary in the growth diagram between layer-by-layer or 3D island growth is given approximately from $t_{layer} \sim t_{nuc}$:

$$\frac{L^3 \sqrt{S_C} r N_0}{\upsilon} \left(\frac{\Delta\mu - S_C \Delta\sigma}{\pi \Delta\mu^2} kT \right)^{1/2} \exp\left(\frac{\varphi + (E_{des} - E_{sd})/2 - \frac{4\chi^2 S_C}{\Delta\mu - S_C \Delta\sigma}}{kT} \right) \sim 1 \tag{18}$$

As can be seen in Eq. (18), layer-by-layer growth can be achieved above a certain threshold $\Delta\mu$ even with $\Delta\sigma > 0$. In addition, the step width L is also an important parameter to tune the growth modes.[50]

By considering all the above discussions, taking Eq. (8) and Eq. (18), using $\Delta\mu$ and T as variables, we are able to construct a growth phase diagram, as shown in Figure 3-9. For simplicity, a Kossel crystal (i.e. here a layer refers to a layer of unit cell instead of an atomic monolayer) has been considered here and we only consider the nearest neighbor interaction for the strength (or the bond energy) b. The parameters used are: L=300 nm; $\nu = 10^{13}$ Hz; a=0.4 nm; r=10^{22} cm^{-2}s^{-1}; $E_{des} = 2b$; $E_{sd} = b$; $\chi = b/2$; and $\varphi = 3b$. The change of surface energy $\Delta\sigma$ is assumed to be zero.

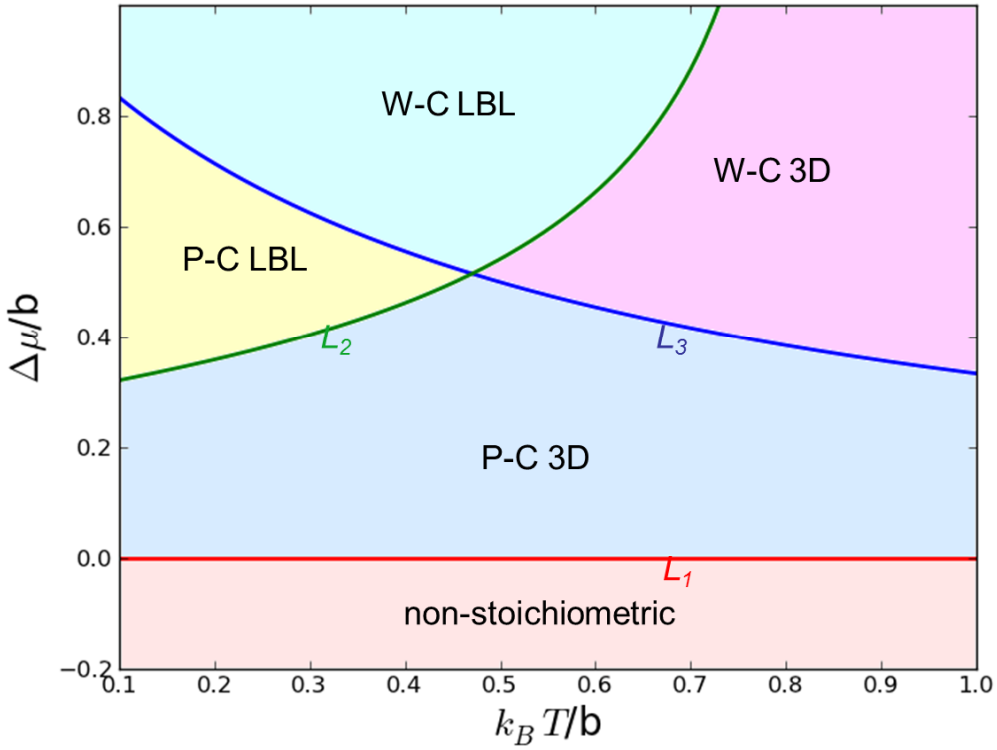

Figure 3-9: The theoretically constructed growth diagram. L_1 (red): boundary between stoichiometric and non-stoichiometric growth; L_2 (green): boundary between layer-by-layer (LBL) and 3D growth; L_3 (blue): boundary between the poorly crystallized (P-C) and well crystallized (W-C) growth.

The boundary L_1 (red online) corresponds to $\Delta\mu = 0$. Below L_1 the growth is non-stoichiometric due to the inability of completing the thermo-chemical transition from the quasi-vapor phase to solid phase of the certain compound.[66] Above L_1 the film can be grown with the right stoichiometry. Boundary L_2 is calculated using Eq.18 which separates the layer-by-layer growth from the 3D growth. Boundary L_3 is calculated using

Eq.8 which separates the poorly crystallized (P-C) and well crystallized (W-C) growth modes. Here we assume that all the boundaries are independent with each other. Thus, five different regions can be defined in the phase diagrams: non-stochiometric; poorly crystallized 3D (P-C 3D); poorly crystallized layer-by-layer (P-C LBL); well crystallized layer-by-layer (W-C LBL); well crystallized 3D (W-C 3D).

We note that the low laser repetition rate used (1 Hz) allows us to use steady-state considerations since the adatoms reach steady-state concentration during pulse intervals.[65] For simplification, we used the average deposition rate to analyze the process of *nucleation* and *step advance*. We also neglected the effect of epitaxial strain which affects step bunching phenomena in the step flow regime.[50]

3.4 Comparison of Experimental Results with Growth Phase Diagram

3.4.1 Dependence of Growth Parameters with Supersaturation

It is important to verify whether the predicted phase diagram is consistent with the experimental data, and provides useful guidance on thin film growth of complex oxides by PLD.

The supersaturation, though not a direct tunable experimental parameter, is dependent on the temperature T, background oxygen pressure P, and the laser fluence (i.e. atom arrival rate r).

As seen in Figure 3-10, in gas-solid phase transition, the phase boundary as a function of $P(T)$ divides the two phases. In equilibrium, if the (P, T) combination falls on the solid side the system is in its solid phase. On the other hand, at non-equilibrium, for a

finite amount of time, a system can be with a (P, T) combination on the solid side but still remains in gas phase. This chemical potential difference between the combination (P, T) in solid phase the combination (P_0, T) on phase boundary is called supersaturation.

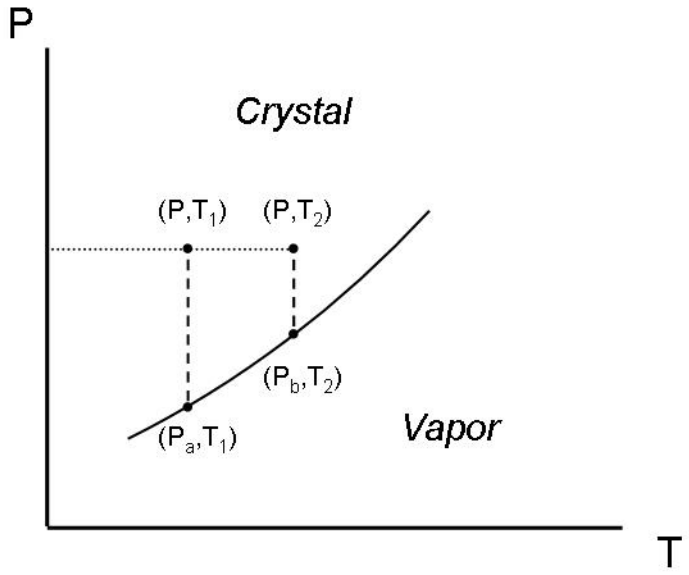

Figure 3-10: Illustration of solid-gas phase diagram

The quantitative definition of supersaturation for point (P, T) is

$$\Delta\mu = RT\ln\left(\frac{P}{P_0}\right) \tag{19}$$

where P_0 is the pressure value at the equilibrium state. Same analogy holds for the atom arrival rate. Thus, supersaturation increases with increasing pressure and laser energy.

To find the dependence of supersaturation on temperature, one has to consider the supersaturation change at the phase boundary, as shown in Figure 3-11:

$$\begin{aligned}&\Delta\mu(P,T_2)-\Delta\mu(P,T_1)=\left[\mu(P,T_2)-\mu(P_b,T_2)\right]-\left[\mu(P,T_1)-\mu(P_a,T_1)\right]\\&=\left[\mu(P,T_2)-\mu(P,T_1)\right]-\left[\mu(P_b,T_2)-\mu(P_a,T_1)\right]\end{aligned} \tag{20}$$

From Gibbs-Duham equation $d\mu = vdP - sdT$ where S denotes the entropy, the first term:

$$\left[\mu(P,T_2)-\mu(P,T_1)\right]=-s(T_2-T_1) \tag{21}$$

The second term is the chemical potential changes along the phase boundary, which has the relation $d\ln P = -\Delta h/Rd(1/T)$, where Δh is the enthalpy change between crystal and vapor phase per mole, which does not vary too much with temperature.

Using Gibbs-Duham equation again, one can get:

$d\Delta\mu = -\Delta h d(\ln T) + \left[s(P,T)-s(P,boundary)\right]dT$, where s(P, boundary) is the entropy at the phase boundary with pressure P. Since entropy does not change very much within the solid phase, $d\Delta\mu \approx -\Delta h d(\ln T)$.

One can see that at constant pressure, the supersaturation decreases approximately exponentially with increasing temperature.

3.4.2 Comparison of Experimental and Theoretical Data

In Figure 3-11, we summarize our experimental AFM images and fit them into the theoretical growth diagram. For guiding purpose, we use different arrows to illustrate the qualitative dependence of growth mode under different growth parameters.

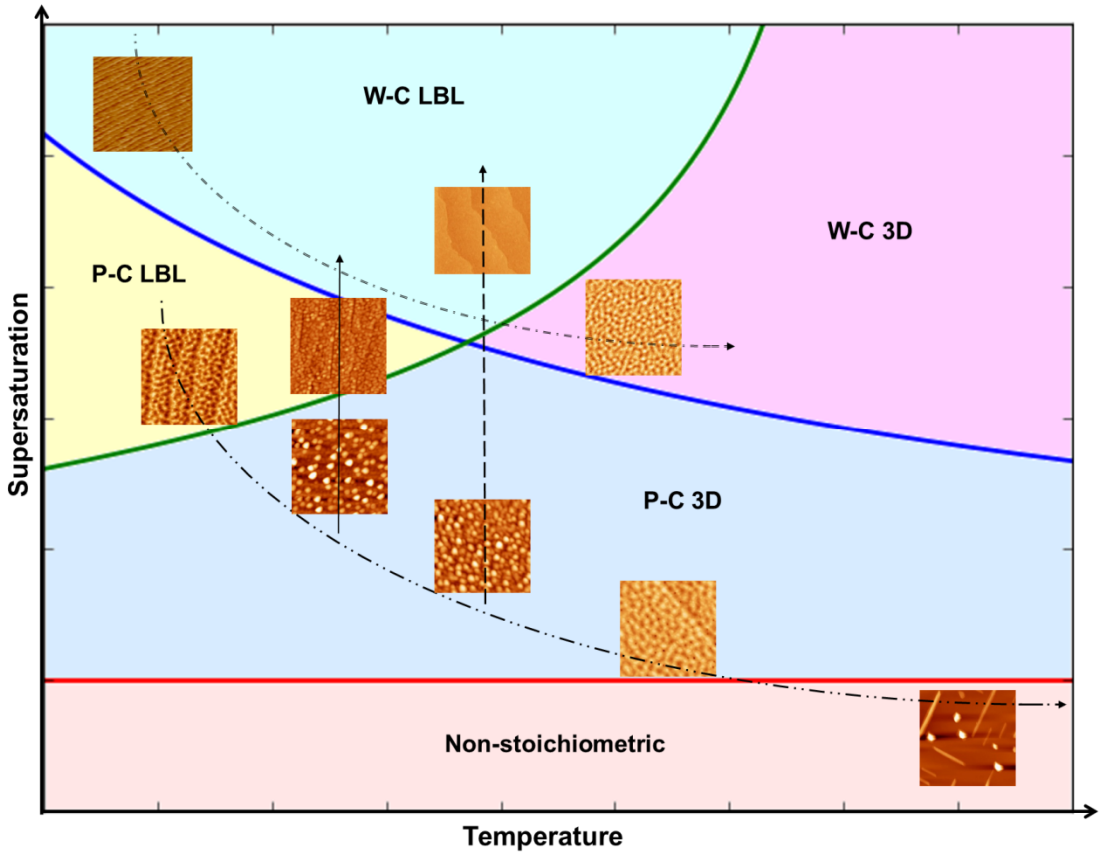

Figure 3-11: Qualitative comparison between experimental results and theoretical growth diagram. Arrows description: dash-dot-dot: temperature increase (720 ^{o}C, 776 ^{o}C, 840 ^{o}C) under constant laser fluence (1J/cm^2) and pressure; dash-dot: temperature increase (660 ^{o}C, 760 ^{o}C) under constant laser fluence (4J/cm^2) and pressure; long dash: laser fluence increase (1J/cm^2, 2.2 J/cm^2) under constant temperature and pressure; solid: pressure increase under constant temperature (730 ^{o}C) and laser fluence (1J/cm^2).

First, the temperature dependence of samples grown at a laser fluence of 1 J/cm^2 is shown (the dash-dot-dot arrow). As discussed, the sample grown at 720 ^{o}C has a poorly crystallized layer-by-layer feature, so it falls into P-C LBL region. By increasing the

temperature to 776 ^{o}C, the growth mode becomes three dimensional, corresponding to region P-C 3D; while further increasing the growth temperature to 840 ^{o}C will lead the system to non-stoichiometry. Next, we study the temperature dependence of samples grown at relatively large laser fluence of 4 J/cm^2, as indicated by the dash-dot arrow. For sample grown at 660 ^{o}C, the high supersaturation is able to put the system into a well crystallized layer-by-layer growth (region W-C LBL). By increasing the temperature from 660 ^{o}C to 760 ^{o}C, the sample crosses into a well crystallized 3D growth mode (region W-C 3D), consistent with our theoretical understanding.

We also examine the effect of laser fluence at fixed temperature and background pressure. Higher laser fluence translates into a higher ablated atom arrival rate, which implies a larger supersaturation. Indeed our experiments reveal that a higher laser fluence can lead the samples from a poorly-crystallized 3D phase (region P-C 3D) into a well-crystallized layer-by-layer phase (region W-C LBL), as indicated by long dash arrow in Figure 3-11. Similar results have been revealed in experiments in which films become smoother when increasing the laser repetition rate.[67,68] The increase of the oxygen pressure also corresponds to an enhancement of the supersaturation, which leads the thin film from a P-C 3D state to a P-C LBL state (solid arrow).

The experimental and theoretical results in this work are consistent with the findings of Metev et al.[33,64] in which a high deposition rate (high supersaturation) and a low growth temperature favored a 2D growth mode. The dependence of the boundary between step-flow growth and 2D island formation constructed by W. Hong et al.[50] on the atomic flux (supersaturation) differ from the findings of this work. On the other hand, the boundary constructed by W. Hong et al.[50] has not been verified by experiments. The

observation of Ohtomo and Hwang[51] also fits nicely in our more complete growth diagram because according to our theoretical model, the supersaturation decreases with temperature and increases with oxygen pressure.

3.4.3 Summary

To summarize, we studied the surface morphology, crystallinity and stoichiometry of LSMO thin films on STO (001) substrates grown using PLD. Various growth modes and phases have been observed. Theoretical considerations establish a growth phase diagram which reveals the nature of different growth modes in terms of supersaturation and temperature under the following condition: 1) the change of surface energy $\Delta\sigma$ is ignorable; 2) the *step advance* is in the diffusion region; 3) the early stage of forming a layer is the most important in the growth process. As a result of the thorough theoretical framework, our derived growth diagram excellently matches the experimentally observed growth modes. As a case study, our results demonstrate the possibility of more comprehensive understanding on controlling growth process and film qualities in PLD growth.

Chapter 4 Electric Field Effect in Spatial Confined Manganites

4.1 Novel Resistive Switching Effect in Phase Separated Manganites

4.1.1 Introduction and Motivation

Starting from Tokura's paper in 1997, which demonstrate in PCMO the collapse of the charge-ordered insulating state to a ferromagnetic metallic state by a large static electric field[28], extensive study using static or pulse E field to trigger phase transition have been demonstrated by different groups. Tokunaga et al. found that in $(La_{1-y}Pr_y)_{0.7}Ca_{0.3}MnO_3$ (y=0.7) bulk system, electric current around 20mA can break the phase separation inhomogeneous state to homogeneous insulating state by local heating effect (Figure 4-1, left).[69] In another case, $La_{5/8-y}Pr_yCa_{3/8}MnO_3$ (y=0.4) insulating to metallic transition under large voltage and the heating effect has been excluded in this case (Figure 4-1 right).[70] These effects show interesting physics of how to manipulate the phase domains under applied E field, though lots of unexplained problems still remain.

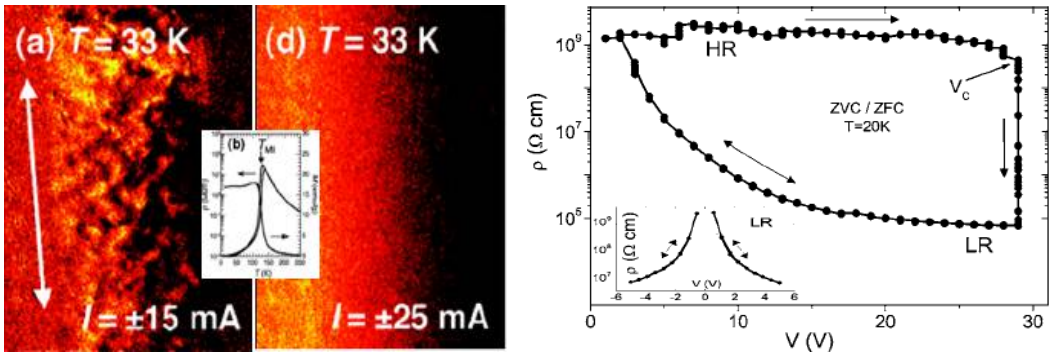

Figure 4-1: electric current and field effect on manganites. Left: Magneto-optical image of breaking phase separation state to homogenous state by current from Ref. [68]; Right: Insulating to metallic transition above a threshold voltage from Ref. [69]

Another main purpose to study electric field effect is the application of resistive random access memory (RRAM), which is considered as new generation of flash memory device due to its low operation voltage, nonvolatile, long operation time, etc. Perovskite manganites are one of the most promising categories. In principle, with different polarity of electric pulse, the manganites stay different resistivity level, namely Electric pluses induced resistive switching (EPIR). In 2000, Liu et al.[71] first reported the EPIR effect using PCMO, as shown in Figure 4-2. After that, similar effects are reported in different manganites materials such as LCMO, NSMO[72] and LPCMO[73].

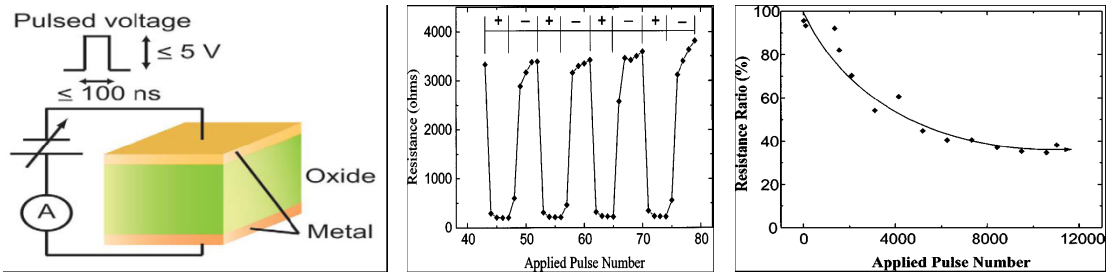

Figure 4-2: RRAM effect in PCMO manganites. Left: typical device geometry, from Ref. [71]; Middle and Right: Typical RRAM behavior, from Ref. [70].

While the underlining mechanism of the EPIR effect in manganites is still far from clear, different mechanisms are discussed such as filamentary conducting path[74], Schottky-like barrier[75] and oxygen vacancies. None of them can comprehensively explain the switching effect. On the other hand, many people assume that such an effect has a strong connection with the spatial inhomogeneity (or phase separation) widely existing in perovskite manganites. Rozenberg et al. proposed a theoretical model to achieve bipolar resistive switching by assuming small non-percolating metallic domains embedded in large insulating matrix.[73] However, no direct experimental evidence is available to clearly address this issue.

4.1.2 Experimental Findings

Here, we are not focusing on the interface effect, but on how the electric voltage pulses can influence the manganites in the EPS states. To study such effect, we want to access as few domains as possible through photolithography technique. 50nm (La_{1-}

$_{x}Pr_{x})_{5/8}Ca_{3/8}MnO_3$ single crystal thin film is grown on the $SrTiO_3$ (001) substrate. LPCMO wires with width of 300um and 1.6um is fabricated on the same substrate, as shown in Figure 4-3a. Constant current of 100nA is used during all measurement.

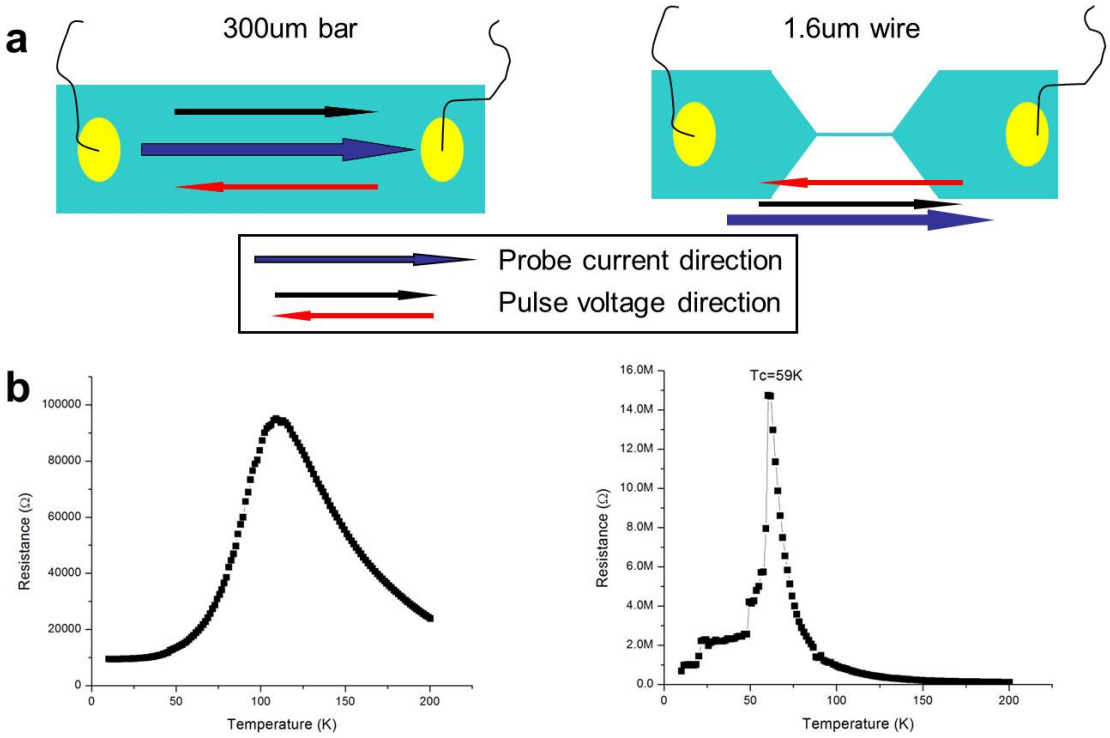

Figure 4-3: sample geometry and RvsT data. (a) 300um and 1.6um wide wire, the probe direction and pulse direction are indicated. (b) Resistance vs Temperature data at 3T.

The resistance vs temperature field cooling data is shown in Figure 4-3b at constant magnetic field of 3T. It is noticed that the 300um wire shows a smooth insulator to metal transition at around 110K, while the 1.6um wire shows strong step-like feature at low temperature, consistent with previous reports.[37] A transition of decreasing resistance is found around 59K, indicating COI and FMM phase coexistence at a wide temperature window. In the following, we will input voltage pulses through the contacts with different polarities and then measure the wire resistance after pulsing. This procedure is the same analogy of RRAM device, the difference lies in that our samples resistance is dominated by the wire bulk, not the metal-manganites interface.

We kept the magnetic field at 3T and decrease the temperature to desired point, then starting the pulsing sequences. Figure 4-4a shows typical features of voltage pulse induced resistance change at the EPS region. Generally, resistance decrease monotonously after voltage pulses is applied. We calculated the relative percentage of resistance change at different temperatures for both wires at fixed maximum pulse voltage of ±10V, using the equation $CER\% = (R_H - R_L)/R_L$, where R_H and R_L denote the high and low resistance states before and after pulsing, respectively. From Figure 4-4b, it is seen that in 300um wire the maximum CER change is about 60% while in a 1.6um wire the CER change can be as huge as 6000% at 65K, which is near the critical temperature of 59K for this wire.

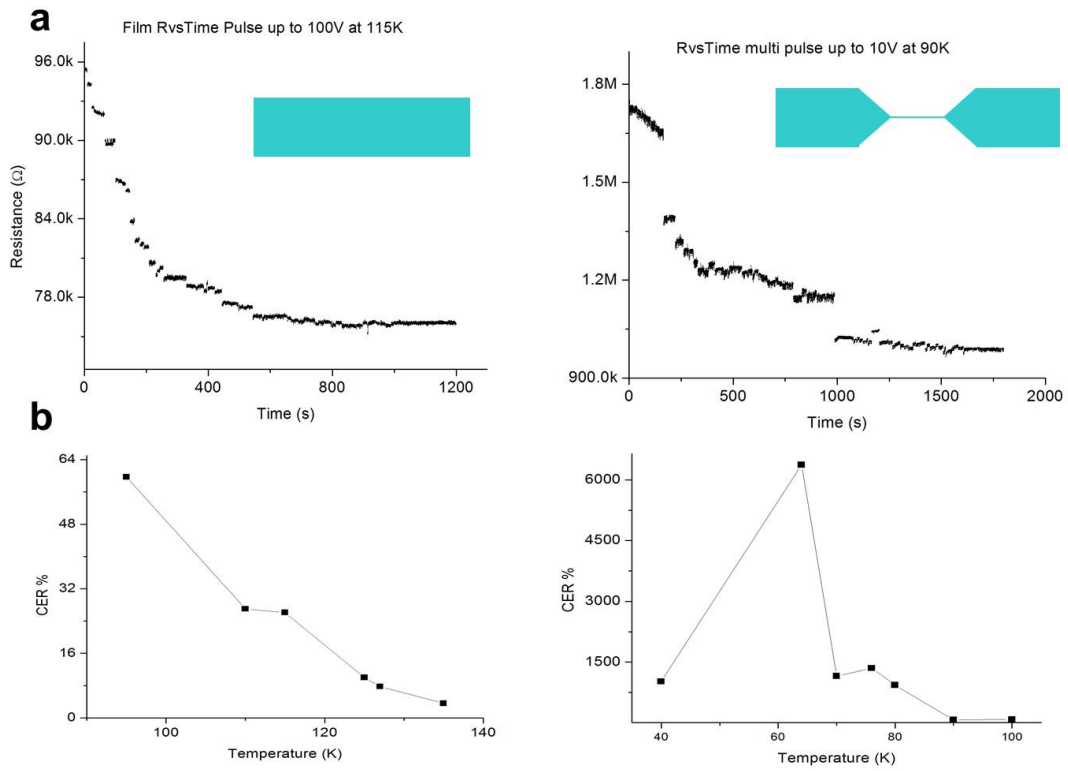

Figure 4-4: Voltage pulses induced resistance change. (a) Resistance decreases with applied pulsed voltages for 300um and 1.6um wire. (b) CER% change at different temperatures.

These features is somewhat expected and can be explained in a scenario of COI melting under applied electrical voltages.[76] At the phase coexisting regions, the electrical voltage can trigger the breakdown of COI domains and COI domains become metallic to open conducting channels inside the system. Thus, decrease in resistance state is seen. While in the 1.6um wire, the global transport properties are dominant by a few residual domains inside the wire. The breakdown of one COI domain will have substantial influence on the transport properties, thus a very large change in resistance is observed.

This effect is smeared out when wire width is increased since multi-channel percolation is possible so that opening or closing one channel will have a smaller effect on the transport properties, as indicated by 300um wire.

We keep focusing our study on the 1.6um wire. Unexpected behavior is found when we further pulse voltage into the system. Figure 4-5a shows the resistance change versus time plot while the voltage bias of 5V and -1V is applied at an interval of approximately 20sec. Resistance drop is first observed followed by a reversible resistive switching behavior. A zoom-in plot of the resistive switching part is shown in Figure 4-5b. This behavior is unusual since it is widely accepted that the voltage induced breakdown of COI states is irreversible. Such behavior suggests new mechanism as driving forces for the resistive switching behavior.

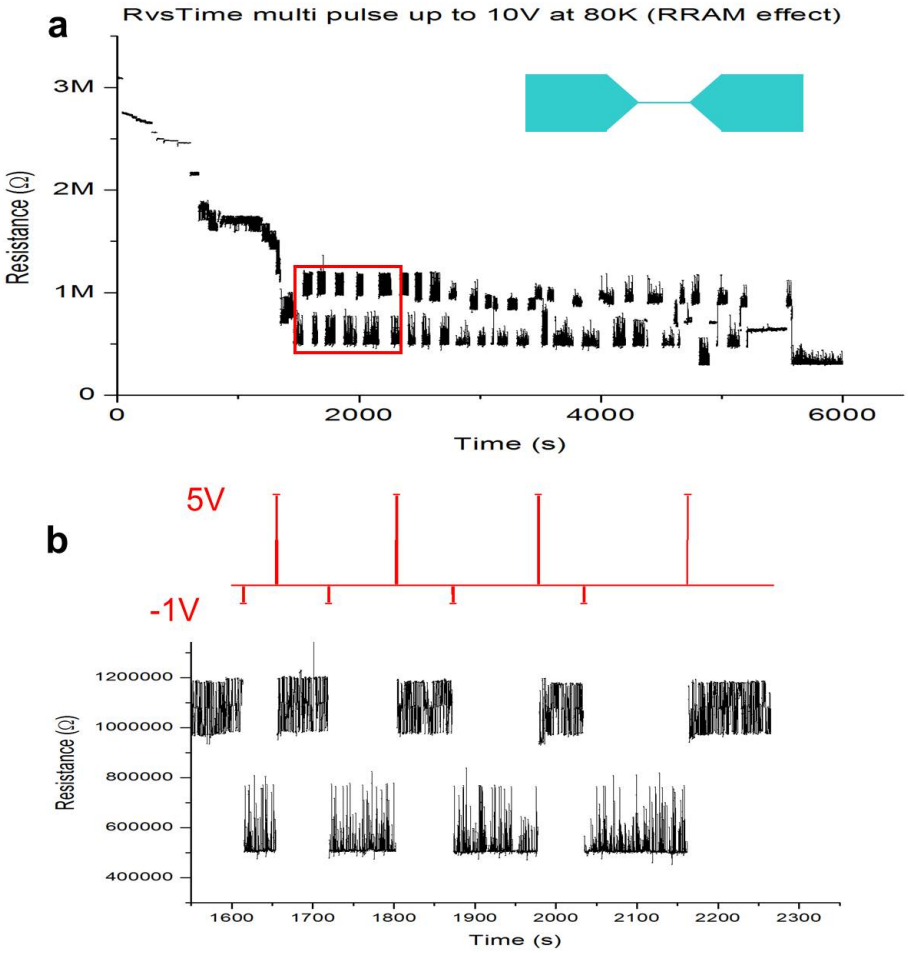

Figure 4-5: Voltage pulses induced resistive switching. (a) Resistance vs time plot. (b) zoom-in plot of red rectangular region in (a).

We have considered several possibilities which may cause such behavior. Joule heating can be possible reason for such switching behavior because by applying voltage pulses, current will flow through the manganites inevitably.[77–79] We rule out heating effect by doing a small trick. While pursuing the voltage pulse sequence of 5V, -1V, 5V, -1V, after 5V is applied and removed, we apply a voltage pulse of 1V. As shown in

Figure 4-6, the 1V pulse has no effect on changing the resistance state which indicates that voltage with opposite polarity (-1V) is necessary to induce such memory effect. The voltage of 1V and -1V will produce the same amount of heat in our LPCMO wire, thus the Joule heating can be excluded to explain our mechanism.

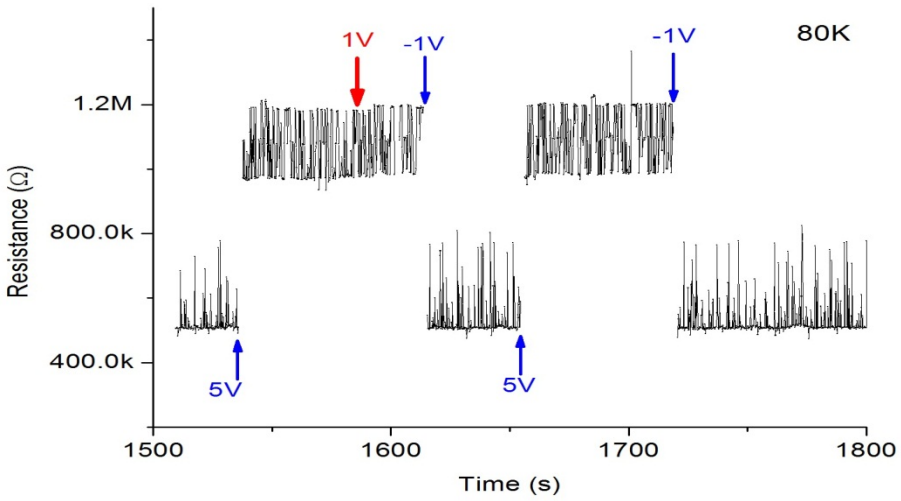

Figure 4-6: Breaking voltage pulse sequences to rule out heating effect.

While our findings seem to have the same effect as a traditional RRAM effect which can be attributed as interface effect, our data differs from the traditional RRAM in the following ways. First, our data can be repeat in both 2-probe and 4-probe configuration, thus any effect due to contact interface resistance can be ruled out. Second, in Figure 4-7, the I-V characteristic of our RRAM behavior is present, the direction of I-V hysteresis differs from normal RRAM device, in fact, two resistance states disappear after I-V sweep, possibly due to melting of COI phase. Third, our effect is only visible in a temperature window from 70K-80K, where the COI state is still robust in the wire. Therefore, our findings differ totally from normal RRAM devices and strongly suggest EPS related novel RRAM phenomena.

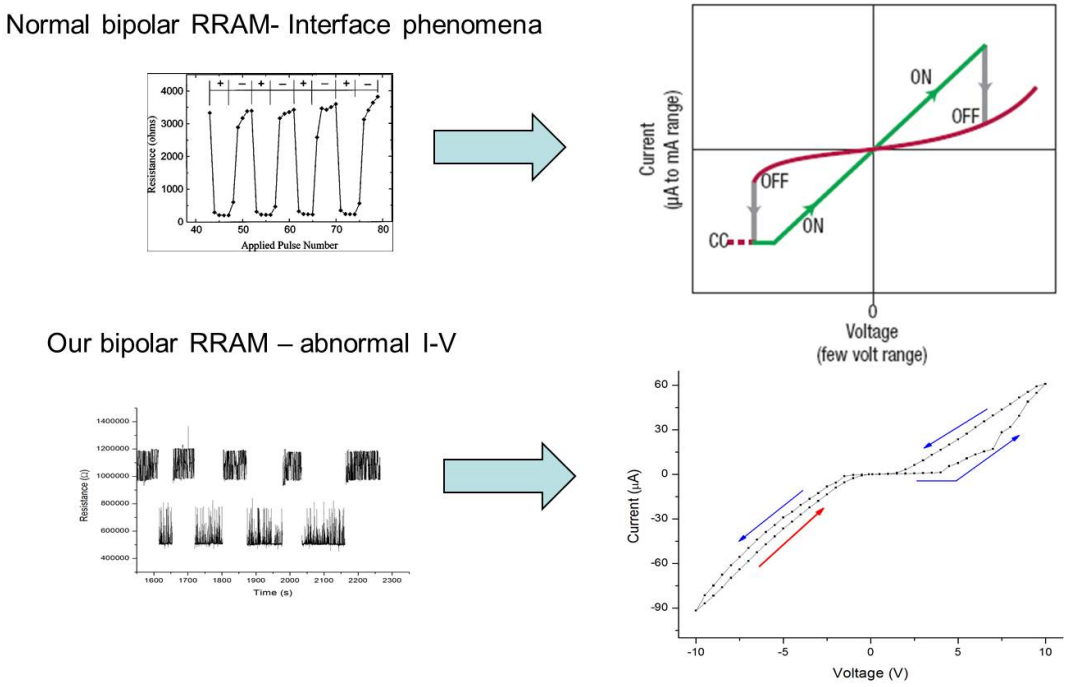

Figure 4-7: Comparison of I-V characteristic of typical RRAM and our data.

4.1.3 Model Consideration

While imaging techniques such as MFM and Microwave Impedance Microscopy (MIM)[80] is desirable to check how the domains react with the applied voltage, at this stage, it is very difficult since it involves leads led into system with low temperature and high magnetic field. So here we propose a mechanism that can explain the phenomena.

It is known that the electric field can lead to melt down of charge ordering phase, it is also been suggested that domain movement can happen under applied electric field.[81] In Figure 4-8, we propose that our finding is a combination of COI melting and domain

movement. At first, the COI domains block the conducting channel inside the wire. At stage (a), the applied voltage melts down the COI state and opening the conduction channel, causing decrease in resistance. While more and more conducting channel is opened, the effect of applied voltage gets smaller on the residual COI domains. Finally, at certain stage (b), the electric voltage does not have enough energy to melt down the COI domains, but is able to make it move. The change of voltage polarity will effectively move the domain back and forth, causing two state resistive switching.

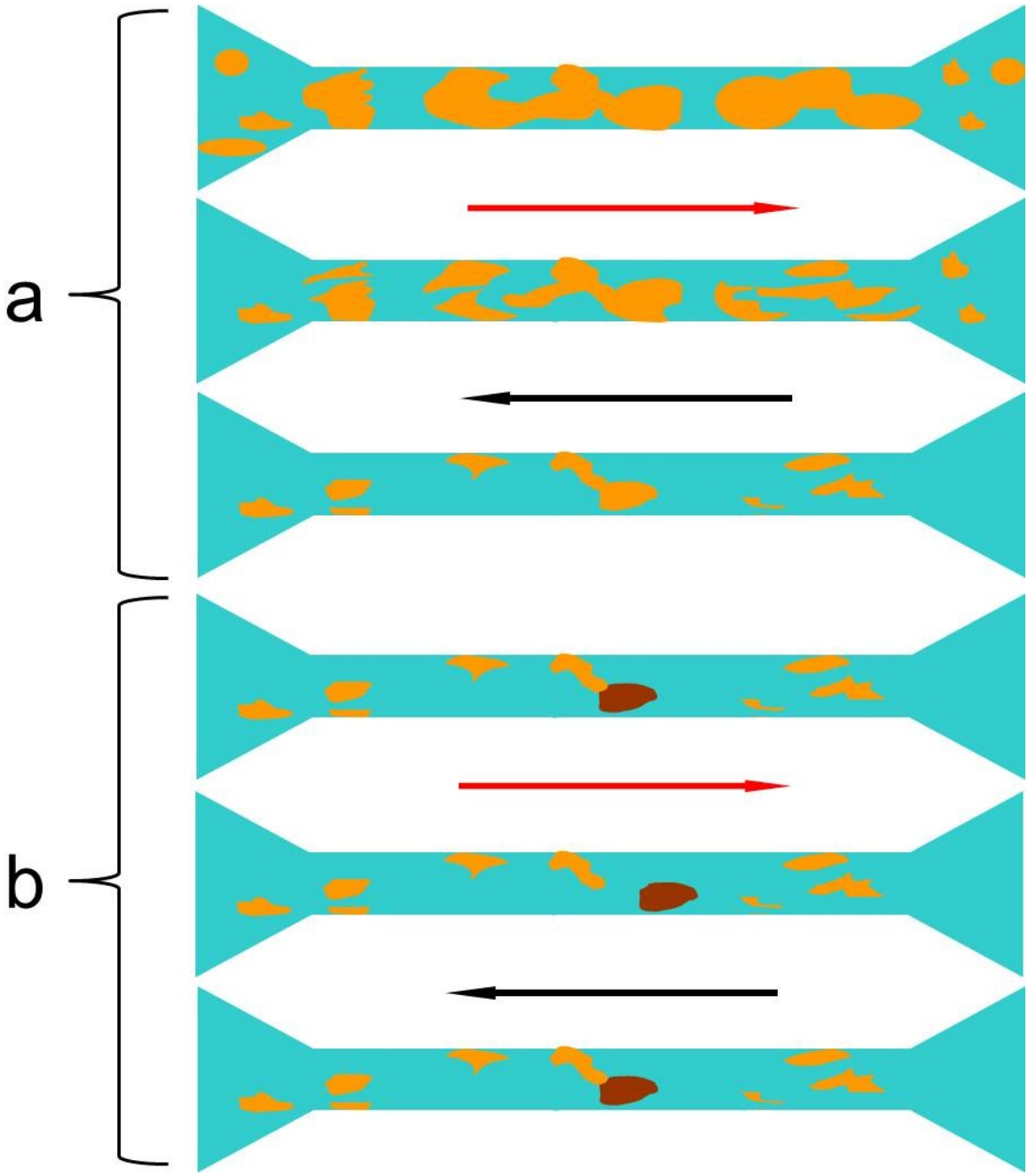

Figure 4-8: Proposed mechanism of two stage voltage pulsed effect.

Our new findings provide a new example on how to use bipolar electrical voltage to create new type of RRAM devices. It is not only the interface that matter, the EPS is very interesting phenomena which can be used to control electronic behavior in manganites.

4.2 Dynamic Resistive Switching Controlled by Local Lateral Gates

4.2.1 Introduction and Motivation

Electronic phase separation in single crystal complex materials is widely observed across many material classes.[1,5,82–85] In these systems, regions with vastly different resistive and magnetic properties can coexist on length scales ranging from microns to nanometers.[82] While there is a great deal of debate on the exact mechanisms that give rise to this phenomenon, it is well accepted that the strongly correlated spin-charge-lattice-orbital order parameters are of central importance in how these phases seed and coexist.[6,72,86] Even small variations to these underlying energetics can have dramatic effects on phase behavior and can lead to colossal changes in character.[30] Most proposed device applications in these exotic systems are based on controlling the macroscopic behaviors by application of global field tuning such as substrate strain, magnetic fields, or thermal manipulation.[5,6,30,87,88]. However, recent work on materials confined to length scales on the same order as the phase domains residing within has shown that it is possible to create structures in which transport is dominated by one or a few domains.[37,40,85,89] This means that macroscopic behaviors can be regulated by controlling mesoscale phenomena which opens the door to using localized fields to create desired electronic circuitry within a single crystal material. We describe an example of this approach where the inherent

metallic and insulating electronic phases are effectively controlled in a spatially confined single crystal manganite wire through the application of local electric fields.

4.2.2 Experimental Methods

50 nm thick [La1-xPrx]5/8Ca3/8MnO3 (x=0.3) films were grown epitaxially on SrTiO3 (001) substrates with a miscut angle of <0.1 degree in an ultrahigh vacuum chamber with a base pressure < 1×10^{-10} Torr using laser (248 nm, 1 J/cm^2 fluence) molecular beam epitaxy. The growth temperature was set at 820 C with an O_2 growth pressure of 1×10^{-3}. Layer by layer growth was monitored by reflection high energy electron diffraction (RHEED) at a growth rate of ~1 unit cell per minute. Films were further annealed ex-situ in flowing O_2 at 1.5 atm at 780 C for 10 hours. Film thickness uniformity, and quality were further verified by atomic force microscope (AFM) and X-ray diffraction.

Firstly, the high-aspect wire structures of LPCMO were patterned by e-beam lithography. Negative maN-2403 e-beam photo resist (Microchem Corp.) was spin-coated at 3000 rpm for 45 s, and then baked on a hot plate at 90 ^{o}C for 1 min. The patterns were exposed using FEI Nanolab 600 equipped with a Raith Elphy Quantum pattern generator at 30 kV acceleration voltage with exposure dose of 200 μC/cm^2. For the 400 and 700 nm wide wire, a higher exposure dose of 280 μC/cm^2 was used. The exposed sample was developed in Microposit MF CD-26 developer for 30 sec, and rinsed with deionize water. The sample was argon ion etched in an Oxford Dry Etcher with an argon flow of 30 standard cubic cm per minute, a Pressure of 3.0 mTorr, an RF Power of 150 W, an ICP RF Power of 2000 W, at 20 ^{o}C for 1 min. After etching, the gate structure

of Au was patterned by e-beam lithography and a lift-off process. Positive ZEP 520A e-beam photo resist (Zeon Corp.) was spin-coated at 3000 rpm for 45 sec, and then baked on a hot plate at 180 ^{o}C for 2 min. The exposure conditions were 30 kV acceleration voltage and 200 $\mu C/cm^2$ dose. The exposed sample was developed in xylene for 30 sec, and rinsed with isopropyl alcohol. Ti (3 nm)/Au (20 nm) was deposited by e-beam evaporation. Finally, large(100mmx100mm) Ti (3 nm)/Au (90 nm) contact pads used for wire bonding and which overlapped the patterned gold gate lines, were patterned using standard UV contact lithography and a lift-off process.

Transport properties were performed on a Quantum Design Physical Property Measurement System (PPMS) using the 2-probe method in a < 1 mTorr vacuum. Electrical connections between the sample and gate electrodes to the PPMS puck were made using a Kulicke and Soffa wire bonder (model 4123) with twenty microns diameter Al wires being directly connected without using any paint or solder. In all transport measurements presented, the magnetic field was applied along the direction perpendicular to the substrate surface during the transport measurements. Resistance measurements were taken in constant current mode using a Keithley 2400 power supply with a drive current of 50nA. All gates were tested at 100 V for leakage current; none was found within limit of measurement device (<100pA). Voltages on gates were applied using Keithley 2400 power supplies in constant voltage mode. Magnetization data was taken using a Quantum Design Magnetic Properties Measurement System. Film's magnetization vs temperature scans were measured using 1000 Oe field applied out-of-plane.

4.2.3 Experimental Findings and Theoretical Considerations

The ideal prototype material to create controllable phase separated circuitry needs to have domain sizes that are easily accessible with standard confinement techniques, must be known to have a sensitivity to order parameter tuning, and must have a region known to possess energetically balanced electronic phases of significantly different resistive properties. For these reasons, we selected the colossal magnetoresistive manganite $[La_{1-x}Pr_x]_{5/8}Ca_{3/8}MnO_3$ (x=0.3) (LPCMO) as an example study. Near its metal insulator transition it is known to have coexisting charge-ordered insulator (COI) and ferromagnetic metal (FMM) domains of a size which can be easily accessed with nanofabrication techniques.[21] These phases have also been shown to coexist in a strain liquid phase, also known as a fluid phase separated state, where the domains strongly interact to maintain local energetic balance.[76,90–92] A 50nm thick single crystal film of LPCMO was grown on a SrTiO3 (001) substrate. The film was etched using electron beam lithography to create 4 pairs of 40um x 40um pads connected by 20um long wires of 400 nm, 700 nm, 1000 nm, and 2000 nm widths. Figure 4-9a shows an example of our experimental device design where a 700 nm x 20um manganite wire is set in a 2-probe geometry with 3 sets of freestanding lateral gates having a width of 1.35um evenly spaced along the wire length to apply in-plane electric fields on each wire across a 1um vacuum gap for each pole. This geometry provides us the opportunity to study how local electric fields can modify electronic phases in a small region of the wire without injecting extra carriers through an interface. Figure 4-9b shows the cooling resistance versus temperature under a 3T magnetic field for all wires. We see that all wires except the widest show very clear sharp jumps in resistance along the metal-insulator transition

which indicates that transport is being dominated by a series of single domains transitioning from an insulating phase to a metallic phase.[34,37,89,93] The onset of the metallic phase seeding is most clearly seen on the 2000nm wire below 123K due to its wider percolation path. The cooling magnetization curve of the parent LPCMO material in Figure 4-9c gives a ferromagnetic metal phase onset below 120K while the warming curve shows the presence of a glass phase below 80K and points to a strain liquid phase between these two temperatures where the metallic regions are not frozen into the background insulating matrix. In 4-9b and 4-9c, the highlighted regions show the temperature range in which a strain liquid phase is present. It is within this region where the phase domains are thought to be most energetically balanced and should give the greatest ability to use external probes to tune the organization of domain structure.

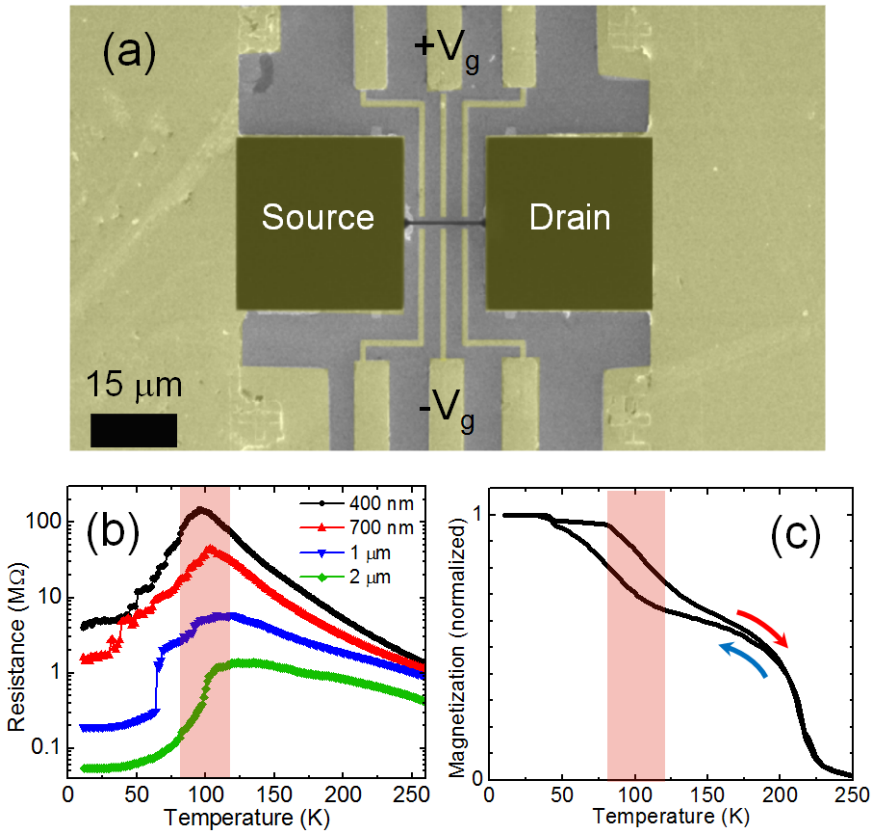

Figure 4-9 Device geometry and basic transport properties of $[La_{1-x}Pr_x]_{5/8}Ca_{3/8}MnO_3$ wires. (a) SEM image of device configuration showing 3 sets of lateral gates placed along phase separated wire. **(b)** Resistance vs temperature on cooling under a 3T magnetic field and 0 gate bias for 20 micron wires **(c)**Magnetization vs temperature plots of parent LPCMO material under 0.1 T magnetic field. Highlighted regions in (b) and (c) show temperature window between onset of ferromagnetic metal phase seeding and blocking temperature where fluid phase separation exists.

In Figure 4-10, we compare the behavior of the 400 nm, 700 nm and 1000 nm wires when applying a bias across the central gate. In each case, we see a clear resistive switch at a voltage that is wire width dependent. The percent change of resistance is also tied to wire width with the wider wires having a smaller resistive change. Indeed, the 2000 nm wire only gives a resistive switching of ~1% and this only at its peak resistance at 115 K (not shown). These resistance switches are dynamic in nature, as the resistance returns to its virgin state when the gate bias is released. This is in stark contrast with previously observed resistive switching behaviors in manganites, where electric field is used in top gating geometries to drive non-dynamic switching through interface modulation or in current pulse geometries that rely on ionic modification.[72,94] Also of note, the resistance remains relatively unchanged below the switching voltage and has only a narrow temperature window of operation which describes a completely different mechanism than traditional semiconductor field effect transistors (FET) where application of a bias immediately begins to saturate the transport channel with holes or carriers and shows a continuous change in resistance preceding the final stable resistance state. Here, the resistive switching is only present within a temperature range of ~120 K – 85K which corresponds to the presence of the strain liquid phase and is consistent with modifications being made to the underlying percolative network upon application of electric field.[76,90–92,95]

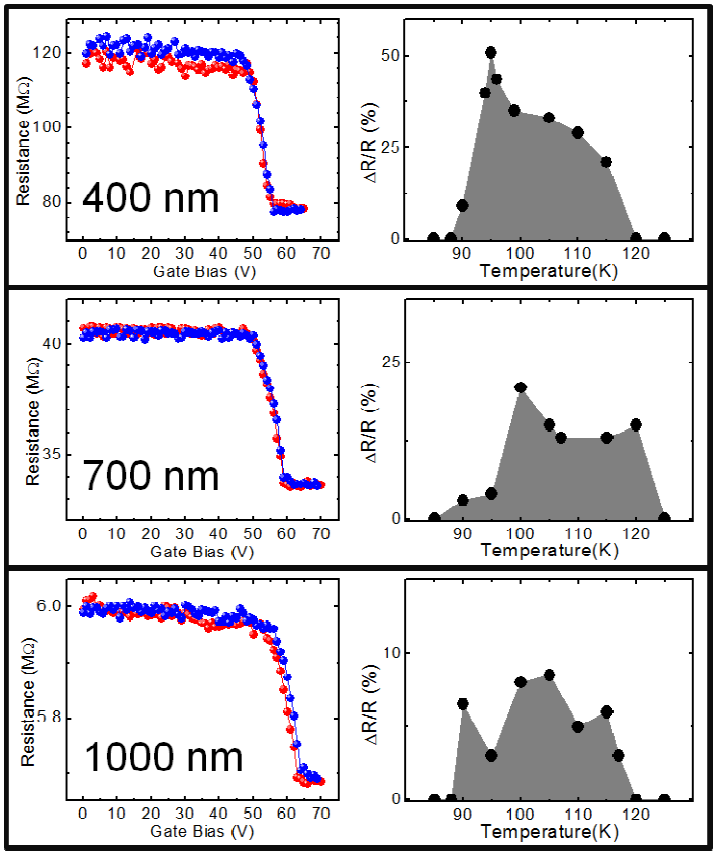

Figure 4-10 Local electric field effects on wire resistances. (Left) Resistance versus gate voltage curves under 3T magnetic field for 400 nm, 700 nm, and 1000 nm wires under central gate electrode bias where each curve is taken at individual peak resistance switching temperature. (Right) Maximum relative resistance change across a range of temperatures for each wire.

To understand the relation between switching bias and wire thickness, we consider the vacuum-LPCMO-vacuum junction as three capacitors in series which allows us to solve for the electric field strength at the edge of each wire. We find that the average electric field at switch onset is very similar for all wires. Figure 4-11a shows the gate biases needed to apply a constant electric field of 114 kV/cm at the wire edges as a function of wire thickness for a serial capacitor model. The average switching bias for each wire is consistent with this linear relation which leads to the conclusion that at a critical electric field there is a fundamental change in the transport channel within the wires.

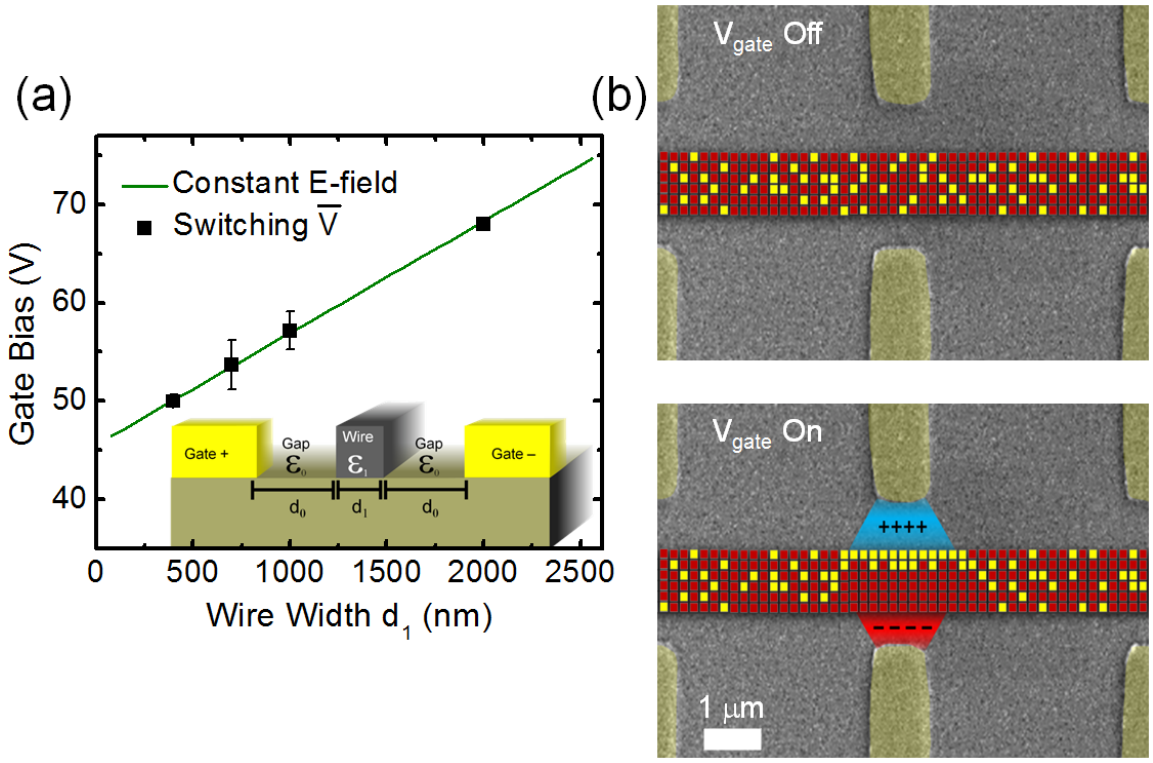

Figure 4-11 Modeled bias and electric field effects. (a) Required gate voltage in a model serial capacitor network for a constant electric field of 114 kV/cm on the wire wall as a function of wire width (green line). **(b)** Colorized SEM images showing three pairs of gates along a wire with superimposed percolative domain movement model. (top) disordered metallic(yellow) and insulating(red) electronic phases coexisting in a random non-percolative network under no electric field. (bottom) Bias applied to central gate creates a non-uniform electric field in the wire which drives electrophoretic domain movement thereby creating a percolation path and causing a large resistive drop.

To understand how the transport channel is being modified we need to consider several possible mechanisms. Electroresisitve switching in manganites has been reported on unconfined samples when large pulses of electric current have been applied along the transport channel which produce an irreversible reduction in resistance across a very wide

temperature range.[70,76] We can rule out this possibility, because we see no measurable leakage current (< 100pA), the resistance is fully recovered when gate bias is reduced below the switch onset voltage, and the switching is only active between metallic domain seeding and glass transition temperatures. Another mechanism to consider is that the substrate is doping carriers into the wire similarly to traditional semiconductor FETs; there are some examples of this in complex oxides.[81,96,97] However, this explanation would require the switching behavior to be active across a wide range of temperature, have a saturation region upon voltage application, and have the sign of electroresistance dependent on bias polarity. We see none of these behaviors.

The reduction in resistance by local electric field in our experiments can be explained in the scenario of phase domain network modification triggered by a critical electric field. These modifications could come from insulating domains transitioning to the metallic phase or from a repositioning of domains to form a low resistance path. There are several reasons to expect the latter explanation. A charge ordered to ferromagnetic metal phase transition is known to be of first order which means that there is a free energy component that must be accounted.[98,35,36] We observe little or no hysteresis in the bias sweeps and the switching field does not appear to be dependent on temperature, so it seems unlikely that the primary cause of the opening percolation path is due to an increase in the metallic volume fraction. This leaves domain sliding as a possible mechanism.

Dielectrophoresis is a mechanism where nonuniform electric fields applied to fluids comprised of two different dielectric values can drive dielectric segregation.[99] In the case of the confined LPCMO wire, the coexisting electronic phases have different

dielectric values and can act to generate the necessary nonuniform electric field while the e_g electrons which drive phase formation can migrate similarly to a liquid.[99] As depicted in Figure 4-11b, between the onset of the seeding of the metallic phase and the glass transition blocking temperature, the insulating and metallic phases coexist in an unconnected percolative network.[100] In this fluid phase separated region, the energy balance between the insulating and metallic phases are very close which allows domain sliding with the application of an external electric field.[90,95,99] The metallic and insulating phases segregate which opens a percolation channel and reduces the wire's resistance. Similar critical electric field needed to trigger this realignment in all wires is consistent with a requirement to overcome seed location pinning sites due to step edges or internal Columbic repulsion between phase domains.[34]

There are several benefits to this type of electronic fluid phase device. Compared to other switching devices, which can degrade with use and time caused by ionic implantation/migration or suffer from dielectric breakdown, this design allows contact free, reversible control of the electronic states which should greatly increase device lifetime.[96] Figure 4-12a shows the resistance of the wire as it is cycled 10,000 times between gate bias of 0.2V and 70V; the two resistance states are stable and without decay over time. Figure 4-12b shows the binned values of all collected resistance states and shows consistent resistance levels. Indeed, no extra carriers are induced into LPCMO wires thus the concern of heating and leakage degrading the device performance can be removed. Also of importance, while one set of gates can produce two stable resistive states, the addition of more gates along the wire length allows access to more unique resistive states. Figure 4-12c demonstrates a four level resistive device that is created

with the use of two sets of gates. Each level is a combination of on and off states triggered by energizing/de-energizing different combinations of the two gates at a bias of 65V. Since the wire region between each gate is unique and has a randomly distributed volume fraction and distribution of metallic domains, the relative change to the percolation channel's resistance after switching is different for each region. As such, fabricating smaller gates or increasing the number of gates should give access to even more resistive levels.

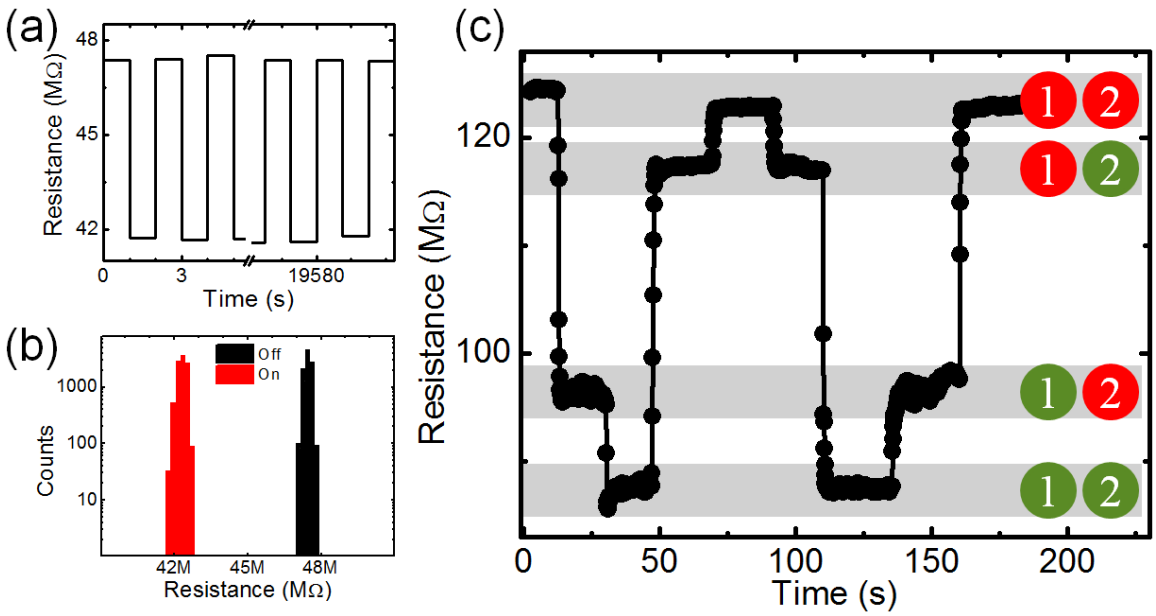

Figure 4-12 Effects of device cycling and example of multi-level switching. **(a)**Horizontal step plot of resistance vs time where a 70 V bias is applied and removed with a full cycle every 2 seconds. Resistance levels are nearly identical at the beginning and end of 10,000 cycles with no sign of aging. **(b)**Histogram of resistive levels collected from 10,000 voltage cycles show two clear resistive levels corresponding to the biased and unbiased states. **(c)** four level resistive behavior achieved by controlling two pairs of gates simultaneously on the same wire. 1 corresponds to the central gate while 2 corresponds to a gate nearer the drain pad. Red represents that the gate is unbiased. The lowest resistance state corresponds to a 65 V bias applied to both gates while the highest resistance state is reached with no applied bias on either gate.

As a prototype system, LPCMO allows us to access local electronic properties where mesoscale phenomena can be used to dominate macroscopic transport. Further reduction of gap size and backfill of high-k dielectric in vacuum are possible strategy to help reduce the voltage amplitude to trigger such memory effect. The utilization of nanometer scale EPS in materials such as $LaCaMnO_3$ can help shrinking down the device to the scale of tens of nanometers. The usage of $LrSaMnO_3$ which reported to have EPS around room temperature will open up the possibility towards achieving room-temperature devices for semiconductor technology. Our study provides a new avenue towards controlling electronic phase separation in tuning the electronic properties. There is no shortage of complex materials exhibiting electronic phase separation across a wide spectrum of temperatures, domain sizes, and resistive and magnetic properties. This offers the possibility of creating an almost infinite combination of temperature specific and size selectable electronic devices.

4.3 Seeding FMM Domain Nucleation and Growing by Static Electric Field

4.3.1 Introduction and Motivation

In the previous section, we have shown that by putting the system in the EPS state first and turn on the electrical voltage the reversible resistance state switching is seen. As for the EPS manganites, it is known that the nucleation of domains is a random process even though the mechanism has been proposed by different authors such as quenched disorder and elastic strain.[101,102] It is important that if we can find a way to control the

domain nucleation and percolation process. Indeed, by applying a static electric field, we observed temperature dependent resistance modulation which strongly suggested local FMM domain seeding mechanism.

In recent field effect transistor study based on manganites materials as channel layers, the multilayer field effect configuration with different top gates or bottom gates geometries.[103–106] The common feature of those geometry is that additional electrons or holes are induced into the system which cause carrier modulation so that the effect can be seen in all temperatures. Thus, whether such field effect modulation is correlated with EPS is not clear. By using the geometry as described in the previous section, we are able to apply local electric field without inducing additional carriers, which makes our method the ideal way to study whether the electric field can alter the EPS properties.

4.3.2 Experimental Findings

As shown in Figure 4-13, same geometry is used in this experiment. The electric voltage of 15V is applied across the wire at 260K, where the system is in the paramagnetic insulator state at this temperature. Then, the system is cooled down to 10K under this electric voltage and constant magnetic field. Figure 4- shows typical features of such electric field effect on the resistance vs temperature curve for gating the 400nm wire. While the resistance remains nearly unchanged beyond 150K, the resistance shows a substantial decrease below this temperature, as shown in Figure 4-13 upper image. By turning on two separate sets of gate electrodes, a larger resistance decrease is seen. We summarized the ER percentage and transition temperature shift in the low panel in Figure 4-13. The Electro resistance change up to 400% and T_c shift up to 9K is observed.

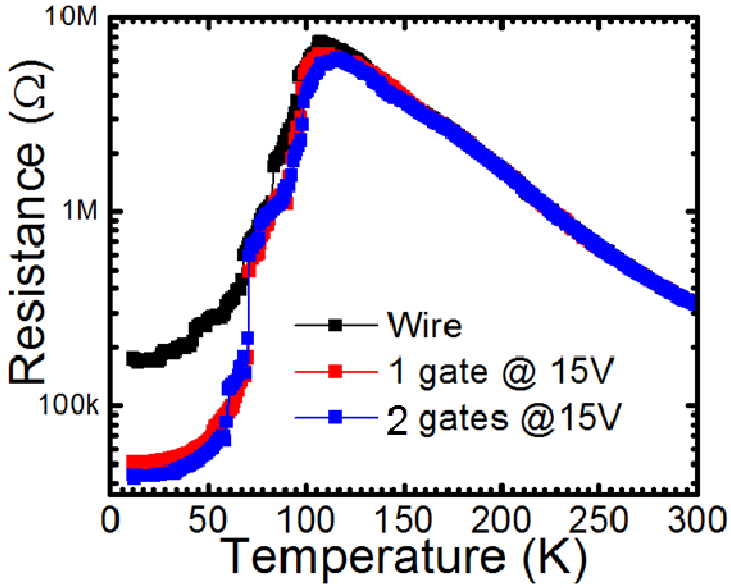

$[LaPr]_{5/8}Ca_{3/8}MnO_3$ 1μm x 10μm wire	Change in transition Temperature (K)	Maximum Electroresistance
1 gate @ 15V	+1	329%
2 gates @ 15V	+9	390%

Figure 4-13: Resistance modulation by static electric field. Upper: resistance modulation for the field cooling process. Lower: maximum change in transition temperature and electro-resistance.

Such electro-resistance modulation is totally different from normal FET behavior since the resistance change only happens below the paramagnetic phase. Considering the fact that no extra carriers are induced into our system, our observation strongly suggests that electric field has modulated the seeding mechanism in the wire.

In Figure 4-14 we conduct one set of experiments by turning on the voltage at 260K and turning off the voltage at different temperature, all biased with three sets of

gate electrodes. The black curve is unbiased while the red curve is 15V biased down to 10K. Distinct difference has seen especially at low temperature regime. For both curves, the low temperature region shows flattened resistance, indicating a partially completed conduction channel. The biased state shows a low resistance with ER % about 50%. The blue curve shows the RvsT resistance with voltage bias turned off at 130K, the temperature which no deviation has occurred for red curve compared to blue one. As seen in Figure 4-14, almost no change in resistance compared with unbiased one is visible. We note that near the transition temperature, due to the random domain seeding with different temperature cycles, it is normal that different RvsT curves show different resistance values.[37] While the low temperature resistance is nearly the same with unbiased one which indicates that beyond 130K, the domain nucleation conditions has not been altered extensively by the local electric field.

Next, we repeat the same procedure but release the bias at 118K as shown in the cyan curve. The cyan curve follow nearly the same tendency as the one biased through the whole temperature range (red), especially at low temperature. This effect clearly indicates that such effect occurs at temperature high than 118K, which is just above the transition where the big drop in resistance takes place. The brown curve is the voltage released at 124K in between 118K and 130K. A resistance state in between black and red curve is clearly seen.

It is well known that in this material, at high temperature, the system is in the paramagnetic insulator phase.[5] As cooling down, a strong COI starts to take over and the resistance keeps on increasing. At certain temperature, the FMM phase starts to pop up inside the COE matrix and energetically favorable to seed and grow. In terms of

measured resistance, it will still go up slowly since the FMM percolation channels have not completed. Once the percolation channels are completed, the resistance will drop substantially, as seen in the black curves in Figure 4-.[107,108] This behavior strongly suggests that applying electric field can force the FMM domain to seed and grow around it. Once the electric field is turned on, the FMM is more likely to seed near the wire edge and grow during further cooling, causing decreased resistance and shifting of transition temperature. It is interesting to point out that such electric field is necessary beyond the transition temperature (cyan curve), and the FMM phase will correspondingly grow afterwards.

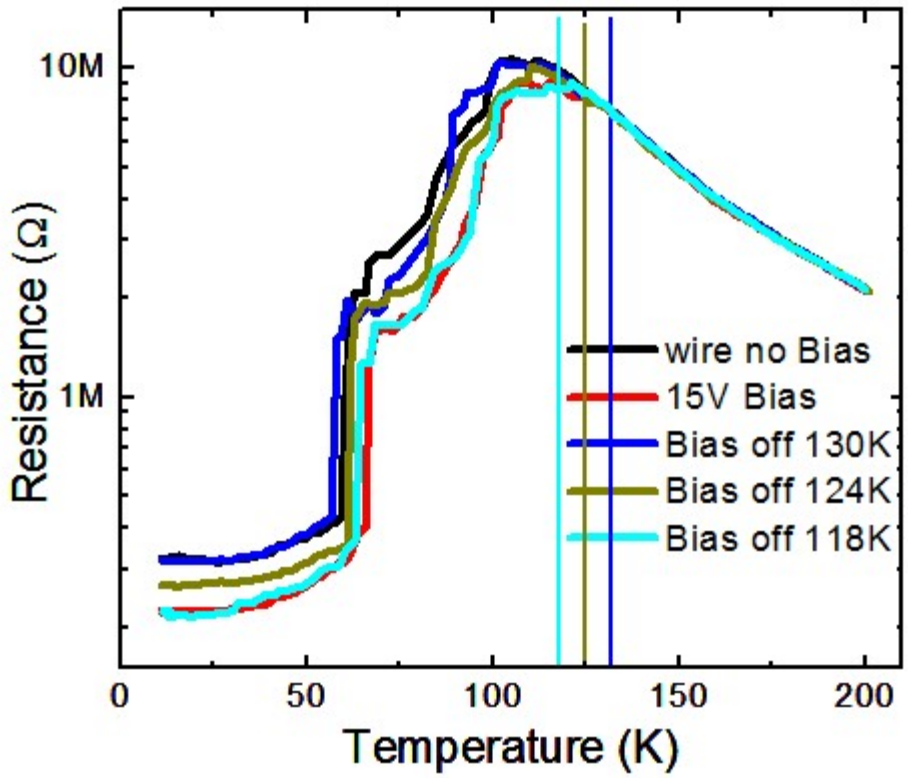

Figure 4-14: Resistance versus Temperature measurement by turning off bias at different temperatures.

The behavior we observed is a unipolar effect[105], i.e. the change of voltage bias polarity does not change the direction of resistance drop. Such effect also suggested that FMM seeding by the static electric field can be accounted for the driving mechanism in our system.

Our findings provide a new example on how to control the EPS state in correlated system by the use of electric field. The geometry of multiple independent gates allow us

to selectively choose multiple seeding locations, thus achieving effective control on the resistance states and transition temperature of phase separated manganites.

Chapter 5 Ongoing and Future Works

5.1 Inherent R-C Circuits in Confined EPS Manganites

Due to the random seeding of EPS states in manganites, the effective and precise control of the electronic domains becomes a challenging goal on the manganites. During the past several years, we have effectively using different experimental knobs towards understanding and controlling EPS.[109] The utilization of EPS as functional devices is another important field we want to achieve right now and in the future. Here, we propose a possible utilization of spatial confined manganites thin film as inherent band-pass filter. Our results on I-V curves indicate that an inherent R-C circuit may exist once the sample is grown on a single substrate.

Thin film of LPCMO with 0.3 Pr doping is grown on $LaAlO_3$ substrate. Wire of 20um and 5um width is fabricated using conventional wet etch lithography. The I-V curve is taken under changing current as a sequence of 0-500nA-0-(-500nA)-0. Figure 5-1 shows the Resistance vs Temperature data and corresponding I-V characteristics. The 20um wire shows I-V curve which has been reported before, i.e. the system became more metallic like states after current sweeping. This is the typical symbol of COI melting as discussed in the previous chapter. The I-V curves for 5um wire shows a totally different feature. When starting from the origin axis, the I-V curve exhibits a remnance at zero current. Unlike the I-V for 20um wire where the resistance always decreases as sweeping more loops, the remnance behavior is stable even cycling 20 times. Such a remnance effect has never been reported before. It reminds us of the leakage capacitor behavior of typical R-C circuit. Indeed, the capacitive characteristics in LPCMO has been reported previously while the COI domain can be considered as capacitor while the FMM

component is considered as the leaking resistor.[110] Indeed, when the system is not confined to the domain size, any current will flow through the metallic portion along with melting the COI state; while the confinement effect will force the electrons to interact with both states. The phenomena we observed could be attributed to the charging effect of FMM-COI-FMM capacitor, manifested as inherent R-C circuit.

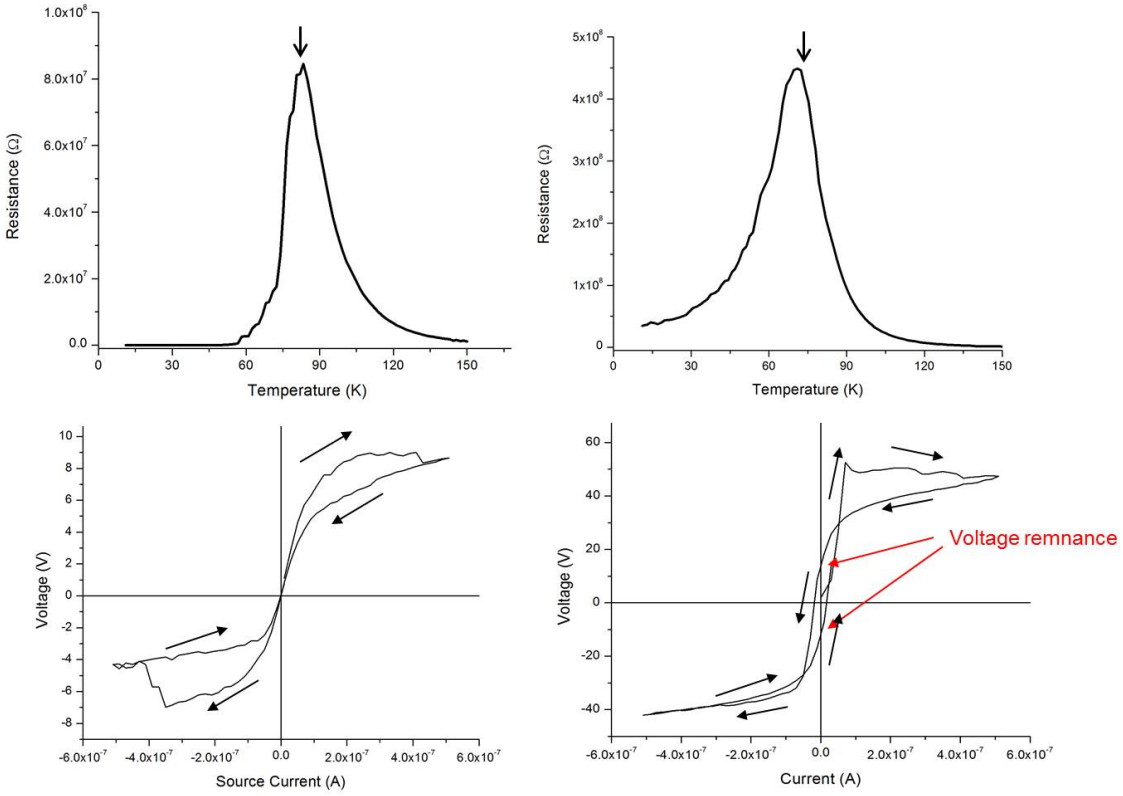

Figure 5-1: I-V characteristics for 20um and 5um LPCMO wires on LAO.

While the R-C circuits have the ability to filter the noise at certain frequency cutoff, acting like either high or low pass, or band pass filter. Our epitaxial confined thin film provides a very good example since the device is inherent after growth and the cut-off can be realized by simple confinement into microns scale. Due to the interaction between COI with the external magnetic field, applying magnetic field could effectively change the relative volume ratio of the COI and FMM domains to effectively control the cut-off properties, hopefully. Our data on I-V curves already show some flavor on the dependence of magnetic field. As shown in Figure 5-2, the remnance behavior is reduced as the magnetic field is applied and finally disappears at 1T. The removal of magnetic field recovers the feature of remnance, consistent with the COI melting and relaxation features.

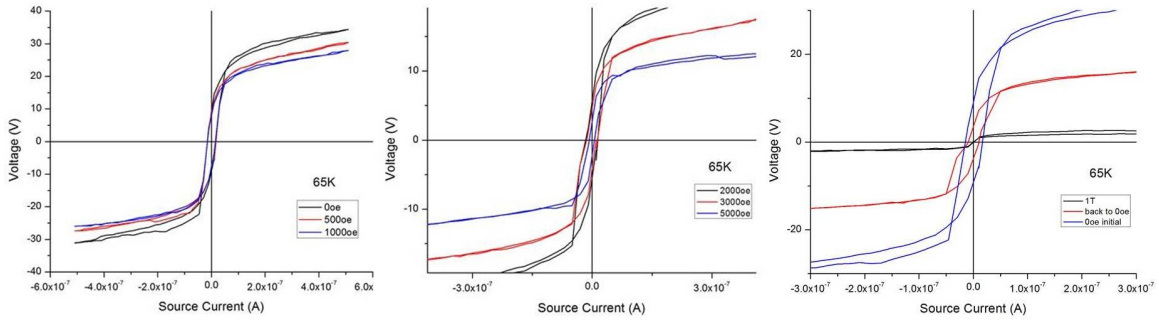

Figure 5-2: I-V characteristics on changing the magnetic field. Magnetic field increases from 0 to 1000oe (left) to 5000oe (middle) to 1T and back to 0T (right).

The capacitive charging may be the mechanism to explain our remnance I-V findings, there are possibilities that the COI may be ferroelectric. The ferroelectricity is known to have electron dipole polarization after removal of electric field.[111] At this stage, this is just a wild guess and evidences from imaging techniques such as PFM should be ideal to prove it.

5.2 Interfacial Effect in Confined Manganites

As introduced in Chapter 4, the utilization of interface effects in manganites has a huge application market potential. The mechanism such as Schottky barriers[75,112], oxygen vacancies[113,114] and Mott transition[115–118] has been proposed. The link between EPS and the interface RRAM behavior has not been established yet. It will be ideal to add controllable EPS state into the RRAM scenario to improve the device diversity. To do this, the key challenge lies in the fabrication of structure into micron scale and the designing of interface structures. Here, we propose two possible ways of studying the correlation of interface RRAM behavior with EPS.

Due to the vertical structure nature of the RRAM devices, it is important to make vertical junctions with the size comparable to EPS domains. It is somewhat very challenging on oxides since it requires a conducting substrate electrode and leakage free vertical junctions. In Figure 5-3, we show a possible geometry of doing such junctions.

(1) Epitaxially grow $SrRuO_3$ (SRO) thin film on top of STO substrate as bottom electrode.

(2) Epitaxially grow LPCMO thin film on top of SRO.

(3) Use conventional optical lithography to etch LPCMO into different patterns, at the end of the lithography process, leave the photoresist on top of the patterned LPCMO and put another droplet of photoresist directly on top of SRO.

(4) Evaporate dielectric materials such as Lu_2O_3 on top of the sample as an insulating medium to separate the bottom and top electrode.

(5) Wash away the photoresist in solvent. The material on the top is lifted off and washed together with the photoresist below. Also, a "hole" is created in SiO_2 layer as a region to evaporate Au/Ti contact onto the bottom electrode SRO.

(6) Evaporate Au/Ti on top of the sample with designed pattern. The Au/Ti on top of LPCMO is used as top electrodes; the Au/Ti on top of the SRO is used as contact to bottom electrode.

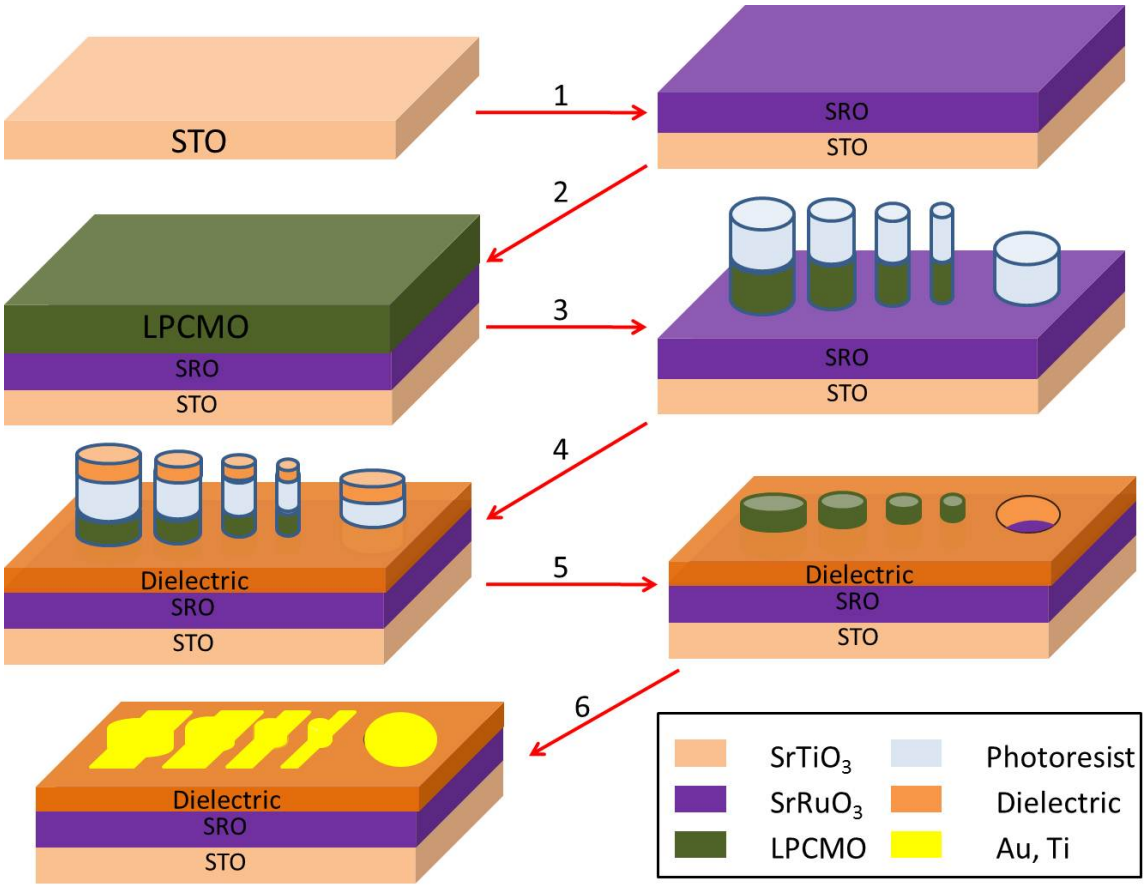

Figure 5-3: Schematic diagram of vertical transport geometry.

The benefit of this approach is to allow us measure the transport properties with small size scale in the vertical direction. We are able to fabricate sub-micrometer size patterns to achieve transport measurement for various purposes. In the case of LPCMO, shrinking down to such length scale gives us the opportunity to reach single domain structure. In that sense, we are capable to manipulate the metallic and insulating phases to achieve different functions.

The method above can help clarify the issue of how spatial inhomogeneity affects the EPIR. By reducing the LPCMO dimension down to hundreds of nanometers, we are able to fabricate the sandwich structure with a pure insulating LPCMO domain which gets rid of the electronic inhomogeneity originally existing. By measuring the electrical pulse induced the resistive switching effect, we have the ability to clarify whether electronic PS has any effect on the electrical pulse induced resistive switching (EPIR).

Also, by shrinking down the sample size from millimeter film-like to sub-micrometer dot-like geometry, it enhances the chance to investigate the single domain dynamics and the two phase competition. The thin film geometry is not a good method to investigate this issue because numerous conducting channels under percolation and lots of competing phases simply smear out all the meaningful fluctuation and competitions of the ferromagnetic metallic and anti-ferromagnetic insulating domains. The wire geometry[9] is a promising way to monitor the fluctuation of the phase dynamics but it still contains finite number of domains coexisting. Using the approach described above, we are able to study single domain dynamics and few domains competing phenomena through transport or other methods. This will benefit to the understanding of the physical dynamics of the perovskite manganites.

Another way of fabrication is to use the wire geometry. Figure 5-4 shows the picture of doing such study. Basically, the confined contact electrodes are put down on top of the spatially confined wire. The current technique can shrink the wire down to 400nm and the contact electrodes down to tens of nanometers, which provides more possibilities on playing with different knobs. By selectively using 2-probe, 3-probe and 4-

probe measurement combined with applying voltage pulse, we expect to see different and new phenomena to clarify the existing puzzles and find new behaviors.

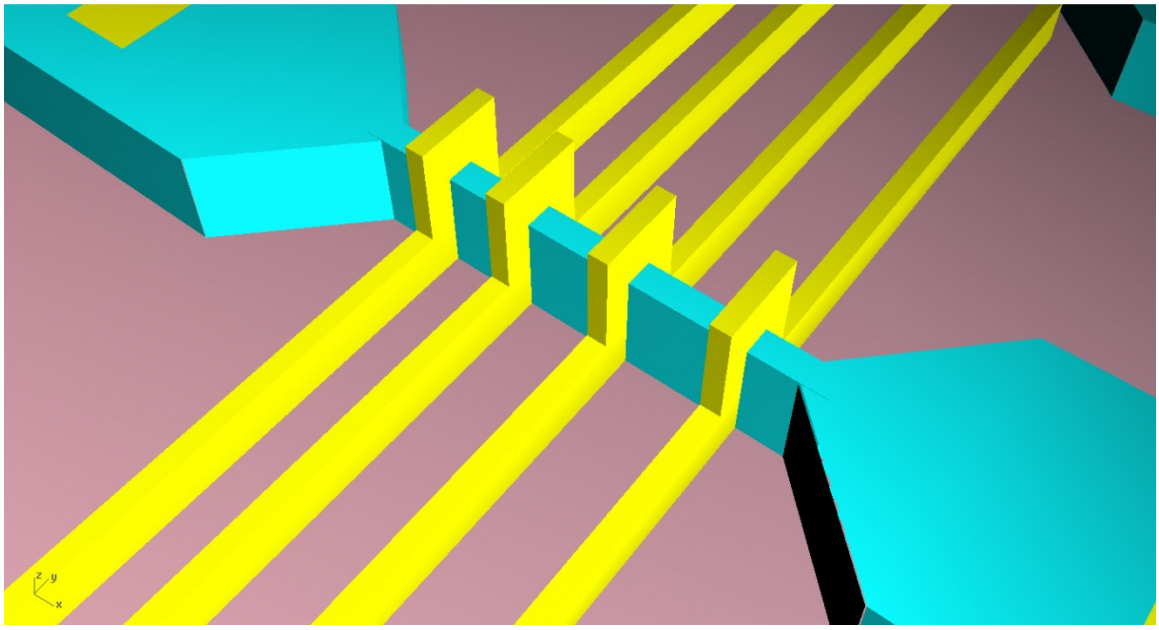

Figure 5-4: Wire geometry on studying interface RRAM effect. Cyan: manganites wire. Gold: contact electrodes.

5.3 Helium Implantation on Lattice Parameter Tuning in Manganites

The strain plays an important role not only on controlling the lattice degrees of freedom, but on electronic, magnetic and orbital degrees. The effective control by substrate lattice mismatch has been shown to successfully controlling the in-plane strain state and anisotropy of EPS domains. Another knob to tune is the controlling of c-axis lattice strain and we successfully find a way to do that by means of Helium implantation. In Figure 5-5, by doping Helium ion into the thin film manganites, we have seen that the c-axis has been expanded by up to 0.7% without degrading the crystal quality. The advantage of using Helium ions is that they are inert so that no electron contribution will be induced into the manganites layers, simplify the problem a lot. Our initial XRD data indicates that the in-plane lattices are still locked to the substrate while the c-axis is expanded. We are working on the issues of how such huge lattice change will influence the magnetic and transport properties of manganites.

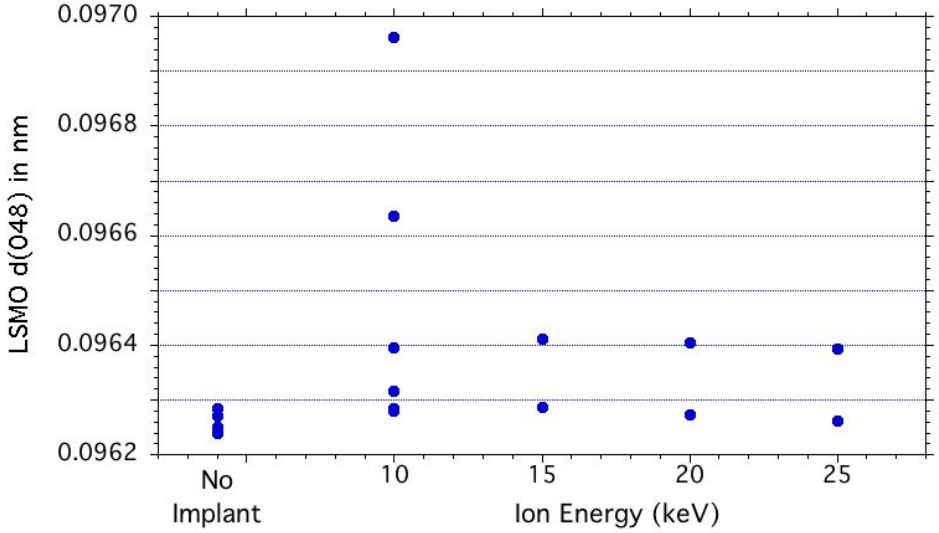

Figure 5-5: Lattice parameter expansion by implanting Helium into LSMO thin film.

5.4 Concluding remarks

Complexity is all around us and it is a great deal if we can disentangle them. In this dissertation, we mainly focused on two directions for this dissertation: establishing a growth phase diagram of PLD thin film growth and electric field control of the EPS manganites.

Somebody may say that the research on growing thin film manganites using PLD is a very mature technique and there is no need to focus the study on them. Indeed,

everyone can grow good quality film right now, but this is not the excuse of stop focusing on the growth. Especially for PLD, the complexity is always present since it involves multiple elements, background gases and high temperature. While different growth features have been observed as little pieces in different papers, there are not many papers which intend to put them together. Moreover, theoretically, it is even more challenging on establishing such a phase diagram because microscopically it is so complicated that assumptions and simplifications have to be made. By reading different books on basic theories and principles, we find that it is possible to putting them together in terms of two parameters: supersaturation and temperature. A theoretical diagram has been established and five different growth modes are proposed. Luckily, the experimental study confirms the feasibility of the growth diagram, at least quantitatively. Although it takes a full year of growing all these samples and taking characterization measurements, it really makes me feel that through this project, I have learned so much on how to think, work as a scientist. The work we have done on the growth diagram is really a small step towards fully understanding the experimental growth observation with the theoretical consideration. More works can to be done such as adding strain into the consideration, defining the phase boundary to further clarify the PLD growth properties.

The study on using electric field to control is very hard at the beginning due to the fact that manganites right now are not the hottest materials and numerous works have been done on it. The discovery of large scale phase separation in LPCMO can be traced back to 13 years ago and many techniques and methods are used to study this system, covering most of the angles. Thus, to find more hidden phenomena, new probing techniques or novel ways of designing is necessary. Spatially confinement is an ideal way

to make a system from parallel resistor network into a series resistor network, unraveling lots of the mystery inside such complex system. By directly putting voltage pulses into the wire, we have observed the novel resistive switching behavior which can be explained in the picture of domain movement. Such finding is not enough to us and we want to study more. When searching in the literature, when people talks about using electric field in terms of putting voltage on the sample through direct contact, it is always an effect of inducing current flowing through the system. Thus, we want to study the effect of pure electric field, without direct current contacting the sample in a spatially confined way. Thanks to the great effort by Dr. Rack and Dr. Noh, the side gate device has been successfully fabricated which allows us to study the local effect on changing the EPS.

Two major observations are observed which can be considered as dynamic and static effects. By putting the system into the EPS state, the application of electric field can induce a reversible change in the local resistance state. We speculate that such electric-field induced resistance modulation can be attributed to electrophoresis effect on moving domain wall, which can be considered as dynamic effect. The static effect are also been observed. By putting the system in the initial paramagnetic states, applying a static electric field and cooling the system down, we find a large electro resistance change up to 400% along with an increase in transition temperature. Such effect strongly suggests that the electric field is able to seed the FMM phase near the wire edge locations and effectively help this phase to grow during cooling. Our findings provides an example of using novel device structure and pure electric field on controlling the phase separation, and hopefully, in the near future, to achieve a real device application of manganites EPS system.

The work presented in this dissertation offers new information on the theoretical and experimental growth of thin film manganites by PLD method as well as effective control of electronic phase separation phenomena by electric field. Further research along this thinking and working line will help us unravel more and more mysteries in the complex material system.

References

1. Shenoy, V.B., Sarma, D.D. & Rao, C.N.R. Electronic Phase Separation in Correlated Oxides: The Phenomenon, Its Present Status and Future Prospects. *ChemPhysChem* **7**, 2053-2059 (2006).

2. Cheong, S.-W., Hwang, H.Y. & Tokura (Ed.), Y. *Colossal Magnetoresistive Oxides*. (Gordon & Breach: New York, 1997).

3. Dagotto, E. Complexity in Strongly Correlated Electronic Systems . *Science* **309** , 257-262 (2005).

4. Ward, T.Z. Emergent Phenomena in Spatially Confined Manganites. (2008).

5. Mathur, N.D. & Littlewood, P.B. The self-organised phases of manganites. *Solid State Communications* **119**, 271-280 (2001).

6. Dagotto, E., Hotta, T. & Moreo, A. Colossal magnetoresistant materials: the key role of phase separation. *Physics Reports* **344**, 1-153 (2001).

7. Zener, C. Interaction between the d-Shells in the Transition Metals. II. Ferromagnetic Compounds of Manganese with Perovskite Structure. *Physical Review* **82**, 403-405 (1951).

8. Anderson, P.W. & Hasegawa, H. Considerations on Double Exchange. *Physical Review* **100**, 675-681 (1955).

9. de Gennes, P.-G. Effects of Double Exchange in Magnetic Crystals. *Physical Review* **118**, 141-154 (1960).

10. Elbio R. A. Dagotto *Nanoscale Phase Separation and Colossal Magnetoresistance*. (Springer: 2002).

11. Mori, S., Chen, C.H. & Cheong, S.-W. Pairing of charge-ordered stripes in (La,Ca)MnO3. *Nature* **392**, 473-476 (1998).

12. Chen, C.H. & Cheong, S.-W. Commensurate to Incommensurate Charge Ordering and Its Real-Space Images in La_{0.5}Ca_{0.5}MnO_{3}. *Physical Review Letters* **76**, 4042-4045 (1996).

13. Radaelli, P.G., Cox, D.E., Marezio, M. & Cheong, S.-W. Charge, orbital, and magnetic ordering in La_{0.5} Ca_{0.5} MnO_{3}s. *Physical Review B* **55**, 3015-3023 (1997).

14. Radaelli, P.G. *et al.* Mesoscopic and microscopic phase segregation in manganese perovskites. *Physical Review B* **63**, 172419 (2001).

15. Millis, A.J., Littlewood, P.B. & Shraiman, B.I. Double Exchange Alone Does Not Explain the Resistivity of La_{1}_{-x}Sr_{x}MnO_{3}. *Physical Review Letters* **74**, 5144-5147 (1995).

16. Röder, H., Zang, J. & Bishop, A.R. Lattice Effects in the Colossal-Magnetoresistance Manganites. *Physical Review Letters* **76**, 1356-1359 (1996).

17. Moreo, A., Yunoki, S. & Dagotto, E. Phase Separation Scenario for Manganese Oxides and Related Materials . *Science* **283** , 2034-2040 (1999).

18. van den Brink, J., Khaliullin, G. & Khomskii, D. Charge and Orbital Order in Half-Doped Manganites. *Physical Review Letters* **83**, 5118-5121 (1999).

19. Arovas, D.P. & Guinea, F. Some aspects of the phase diagram of double-exchange systems. *Physical Review B* **58**, 9150-9155 (1998).

20. Kagan, M.Y., Khomskii, D.I. & Mostovoy, M.V. Double-exchange model: phase separation versus canted spins. *Eur. Phys. J. B* **12**, 217-223 (1999).

21. Uehara, M., Mori, S., Chen, C.H. & Cheong, S.-W. Percolative phase separation underlies colossal magnetoresistance in mixed-valent manganites. *Nature* **399**, 560-563 (1999).

22. Wu, W. *et al.* Magnetic imaging of a supercooling glass transition in a weakly disordered ferromagnet. *Nat Mater* **5**, 881-886 (2006).

23. Israel, C. *et al.* Translating reproducible phase-separated texture in manganites into reproducible two-state low-field magnetoresistance: An imaging and transport study. *Physical Review B* **78**, 54409 (2008).

24. Fäth, M. *et al.* Spatially Inhomogeneous Metal-Insulator Transition in Doped Manganites . *Science* **285** , 1540-1542 (1999).

25. Zhang, L., Israel, C., Biswas, A., Greene, R.L. & de Lozanne, A. Direct Observation of Percolation in a Manganite Thin Film . *Science* **298** , 805-807 (2002).

26. Moreo, A., Mayr, M., Feiguin, A., Yunoki, S. & Dagotto, E. Giant Cluster Coexistence in Doped Manganites and Other Compounds. *Physical Review Letters* **84**, 5568-5571 (2000).

27. Ahn, K.H., Lookman, T. & Bishop, A.R. Strain-induced metal-insulator phase coexistence in perovskite manganites. *Nature* **428**, 401-404 (2004).

28. Asamitsu, A., Tomioka, Y., Kuwahara, H. & Tokura, Y. Current switching of resistive states in magnetoresistive manganites. *Nature* **388**, 50-52 (1997).

29. Gillaspie, D. *et al.* Influence of different substrates on phase separation in La[sub 1 - x - y]Pr[sub y]Ca[sub x]MnO[sub 3] thin films. *Journal of Applied Physics* **99**, 08S901-3 (2006).

30. Ward, T.Z. *et al.* Elastically driven anisotropic percolation in electronic phase-separated manganites. *Nat Phys* **5**, 885-888 (2009).

31. Tosado, J., Dhakal, T. & Biswas, A. Colossal piezoresistance in phase separated manganites. *Journal of Physics: Condensed Matter* **21**, 192203 (2009).

32. Laukhin, V., Fontcuberta, J., García-Muñoz, J.L. & Obradors, X. Pressure effects on the metal-insulator transition in magnetoresistive manganese perovskites. *Physical Review B* **56**, R10009-R10012 (1997).

33. Chrisey, D.B. & Hubler, G.K. *Pulse laser deposition of thin films*. (1994).

34. Ward, T.Z. *et al.* Reemergent Metal-Insulator Transitions in Manganites Exposed with Spatial Confinement. *Physical Review Letters* **100**, 247204 (2008).

35. Ward, T.Z. *et al.* Time-Resolved Electronic Phase Transitions in Manganites. *Physical Review Letters* **102**, 87201 (2009).

36. Ward, T.Z., Gai, Z., Guo, H.W., Yin, L.F. & Shen, J. Dynamics of a first-order electronic phase transition in manganites. *Physical Review B* **83**, 125125 (2011).

37. Zhai, H.-Y. *et al.* Giant Discrete Steps in Metal-Insulator Transition in Perovskite Manganite Wires. *Physical Review Letters* **97**, 167201 (2006).

38. Sarid, D. *Scanning Force Microscopy: With Application to Electric, Magnetic, and Atomic Forces*. 263 (Oxford University Press: 1994).

39. Josephson, B.D. Possible new effects in superconductive tunnelling. *Physics Letters* **1**, 251-253 (1962).

40. Singh-Bhalla, G., Selcuk, S., Dhakal, T., Biswas, A. & Hebard, A.F. Intrinsic Tunneling in Phase Separated Manganites. *Physical Review Letters* **102**, 77205 (2009).

41. Eres, H.M.C. and G. Recent advances in pulsed-laser deposition of complex oxides. *Journal of Physics: Condensed Matter* **20**, 264005 (2008).

42. Ohtomo, A. & Hwang, H.Y. A high-mobility electron gas at the LaAlO3/SrTiO3 heterointerface. *Nature* **427**, 423-426 (2004).

43. Norton, D.P. Synthesis and properties of epitaxial electronic oxide thin-film materials. *Materials Science and Engineering: R: Reports* **43**, 139-247 (2004).

44. Jang, H.W. *et al.* Metallic and Insulating Oxide Interfaces Controlled by Electronic Correlations . *Science* **331** , 886-889 (2011).

45. Jackson, T.J. & Palmer, S.B. Oxide superconductor and magnetic metal thin film deposition by pulsed laser ablation: a review. *Journal of Physics D: Applied Physics* **27**, 1581 (1994).

46. Willmott, P.R. & Huber, J.R. Pulsed laser vaporization and deposition. *Rev. Mod. Phys.* **72**, 315-328 (2000).

47. Willmott, P.R. Deposition of complex multielemental thin films. *Progress in Surface Science* **76**, 163-217 (2004).

48. Ashfold, M.N.R., Claeyssens, F., Fuge, G.M. & Henley, S.J. Pulsed laser ablation and deposition of thin films. *Chemical Society Reviews* **33**, 23-31 (2004).

49. Markov, I.V. *Crystal Growth for Beginners: Fundamentals of Nucleation, Crystal Growth and Epitaxy*. (2003).

50. Hong, W. *et al.* Persistent Step-Flow Growth of Strained Films on Vicinal Substrates. *Physical Review Letters* **95**, 95501 (2005).

51. Ohtomo, A. & Hwang, H.Y. Growth mode control of the free carrier density in SrTiO[sub 3 - delta] films. *Journal of Applied Physics* **102**, 83704 (2007).

52. Sinha, S.K., Bhattacharya, R., Ray, S.K. & Manna, I. Influence of deposition temperature on structure and morphology of nanostructured SnO2 films synthesized by pulsed laser deposition. *Materials Letters* **65**, 146-149 (2011).

53. Sun, D. *et al.* Giant Magnetoresistance in Organic Spin Valves. *Physical Review Letters* **104**, 236602 (2010).

54. Brivio, S. *et al.* Effects of Au nanoparticles on the magnetic and transport properties of La_{0.67}Sr_{0.33}MnO_{3} ultrathin layers. *Physical Review B* **81**, 94410 (2010).

55. Hong, X., Posadas, A., Lin, A. & Ahn, C.H. Ferroelectric-field-induced tuning of magnetism in the colossal magnetoresistive oxide La_{1-x}Sr_{x}MnO_{3}. *Physical Review B* **68**, 134415 (2003).

56. Ferguson, J.D. *et al.* Epitaxial Oxygen Getter for a Brownmillerite Phase Transformation in Manganite Films. *Advanced Materials* **23**, 1226-1230 (2011).

57. Tsui, F., Smoak, M.C., Nath, T.K. & Eom, C.B. Strain-dependent magnetic phase diagram of epitaxial La[sub 0.67]Sr[sub 0.33]MnO[sub 3] thin films. *Applied Physics Letters* **76**, 2421-2423 (2000).

58. *X-Ray Data Booklet*. (Lawrence Berkeley National Laboratory: 2009).

59. http://www.veeco.com/pdfs/mbe/vapor-pressure-Chart-1.pdf. at <http://www.veeco.com/pdfs/mbe/vapor-pressure-Chart-1.pdf>

60. Ohkubo, I. *et al.* High-throughput growth temperature optimization of ferroelectric Sr[sub x]Ba[sub 1 - x]Nb[sub 2]O[sub 6] epitaxial thin films using a temperature gradient method. *Applied Physics Letters* **84**, 1350-1352 (2004).

61. Volmer, M. & Weber, A. No Title. *Zeitschrift für Physikalische Chemie* **119**, 277 (1926).

62. Frank, F.C. & van der Merwe, J.H. One-Dimensional Dislocations. I. Static Theory . *Proceedings of the Royal Society of London. Series A. Mathematical and Physical Sciences* **198** , 205-216 (1949).

63. Stranski, I. & Krastanov, L. No Title. *Sitzugnsber. Akad. Wissenschaft Wien* **146**, 797 (1938).

64. Metev, S. & Meteva, K. Nucleation and growth of laser-plasma deposited thin films. *Applied Surface Science* **43**, 402-408 (1989).

65. Kareev, M. *et al.* Sub-monolayer nucleation and growth of complex oxides at high supersaturation and rapid flux modulation. *Journal of Applied Physics* **109**, 114303 (2011).

66. Wang, W. *et al.* Growth diagram and magnetic properties of hexagonal LuFe{}_{2}O{}_{4} thin films. *Phys. Rev. B* **85**, 155411 (2012).

67. Lee, G.H., Shin, B.C. & Min, B.H. Effect of deposition flux on surface roughness of LiNbO3 thin film grown on sapphire substrate by pulsed laser deposition. *Materials Science and Engineering: B* **95**, 137-140 (2002).

68. Shin, J., Kalinin, S.V., Borisevich, A.Y., Plummer, E.W. & Baddorf, A.P. Layer-by-layer and pseudo-two-dimensional growth modes for heteroepitaxial BaTiO[sub 3] films by exploiting kinetic limitations. *Applied Physics Letters* **91**, 202901 (2007).

69. Tokunaga, M., Tokunaga, Y. & Tamegai, T. Imaging of Percolative Conduction Paths and Their Breakdown in Phase-Separated (La_{1-y}Pr_{y})_{0.7}Ca_{0.3}MnO_{3} with y=0.7. *Physical Review Letters* **93**, 37203 (2004).

70. Garbarino, G., Acha, C., Levy, P., Koo, T.Y. & Cheong, S.-W. Evidence of a consolute critical point in the phase separation regime of

La_{5⁄8−y}Pr_{y}Ca_{3⁄8}MnO_{3} (y∼0.4) single crystals. *Physical Review B* **74**, 100401 (2006).

71. Liu, S.Q., Wu, N.J. & Ignatiev, A. Electric-pulse-induced reversible resistance change effect in magnetoresistive films. *Applied Physics Letters* **76**, 2749-2751 (2000).

72. Sawa, A. Resistive switching in transition metal oxides. *Materials Today* **11**, 28-36 (2008).

73. Quintero, M., Levy, P., Leyva, A.G. & Rozenberg, M.J. Mechanism of Electric-Pulse-Induced Resistance Switching in Manganites. *Physical Review Letters* **98**, 116601 (2007).

74. Aoyama, K., Waku, K., Asanuma, A., Uesu, Y. & Katsufuji, T. Electric-pulse-induced reflectance change in the thin film of perovskite manganite. *Applied Physics Letters* **85**, 1208-1210 (2004).

75. Harada, T. *et al.* Trap-controlled space-charge-limited current mechanism in resistance switching at Al/Pr[sub 0.7]Ca[sub 0.3]MnO[sub 3] interface. *Applied Physics Letters* **92**, 222113 (2008).

76. Dhakal, T., Tosado, J. & Biswas, A. Effect of strain and electric field on the electronic soft matter in manganite thin films. *Physical Review B* **75**, 92404 (2007).

77. Mercone, S. *et al.* Nonlinear effects and Joule heating in I-V curves in manganites. *Journal of Applied Physics* **98**, 23911-23915 (2005).

78. Garbarino, G. *et al.* Current-induced effects in single crystals. *Physica B: Condensed Matter* **354**, 16-19 (2004).

79. Sacanell, J., Leyva, A.G. & Levy, P. Electrical current effect in phase-separated La[sub 5/8 - y]Pr[sub y]Ca[sub 3/8]MnO[sub 3]: Charge order melting versus Joule heating. *Journal of Applied Physics* **98**, 113704-113708 (2005).

80. Lai, K. *et al.* Mesoscopic Percolating Resistance Network in a Strained Manganite Thin Film . *Science* **329** , 190-193 (2010).

81. Wu, T. *et al.* Electroresistance and Electronic Phase Separation in Mixed-Valent Manganites. *Physical Review Letters* **86**, 5998-6001 (2001).

82. Basov, D.N., Averitt, R.D., van der Marel, D., Dressel, M. & Haule, K. Electrodynamics of correlated electron materials. *Reviews of Modern Physics* **83**, 471-541 (2011).

83. Szot, K., Speier, W., Bihlmayer, G. & Waser, R. Switching the electrical resistance of individual dislocations in single-crystalline SrTiO3. *Nat Mater* **5**, 312-320 (2006).

84. Shenoy, V.B. & Rao, C.N.R. Electronic phase separation and other novel phenomena and properties exhibited by mixed-valent rare-earth manganites and related materials . *Philosophical Transactions of the Royal Society A: Mathematical, Physical and Engineering Sciences* **366** , 63-82 (2008).

85. Sharoni, A., Ramírez, J.G. & Schuller, I.K. Multiple Avalanches across the Metal-Insulator Transition of Vanadium Oxide Nanoscaled Junctions. *Physical Review Letters* **101**, 26404 (2008).

86. Ahn, C.H., Triscone, J.-M. & Mannhart, J. Electric field effect in correlated oxide systems. *Nature* **424**, 1015-1018 (2003).

87. Cox, S., Singleton, J., McDonald, R.D., Migliori, A. & Littlewood, P.B. Sliding charge-density wave in manganites. *Nat Mater* **7**, 25-30 (2008).

88. Cao, J. & Wu, J. Strain effects in low-dimensional transition metal oxides. *Materials Science and Engineering: R: Reports* **71**, 35-52 (2011).

89. Wu, T. & Mitchell, J.F. Creation and annihilation of conducting filaments in mesoscopic manganite structures. *Physical Review B* **74**, 214423 (2006).

90. Sacanell, J., Parisi, F., Campoy, J.C.P. & Ghivelder, L. Thermodynamic modeling of phase separation in manganites. *Physical Review B* **73**, 14403 (2006).

91. Sharma, P.A., Kim, S.B., Koo, T.Y., Guha, S. & Cheong, S.-W. Reentrant charge ordering transition in the manganites as experimental evidence for a strain glass. *Physical Review B* **71**, 224416 (2005).

92. Burkhardt, M.H. *et al.* Imaging the First-Order Magnetic Transition in La_{0.35}Pr_{0.275}Ca_{0.375}MnO_{3}. *Physical Review Letters* **108**, 237202 (2012).

93. Wu, T. & Mitchell, J.F. Negative differential resistance in mesoscopic manganite structures. *Applied Physics Letters* **86**, 252503-252505 (2005).

94. Waser, R. & Aono, M. Nanoionics-based resistive switching memories. *Nat Mater* **6**, 833-840 (2007).

95. Dong, S., Zhu, H. & Liu, J.-M. Dielectrophoresis model for the colossal electroresistance of phase-separated manganites. *Physical Review B* **76**, 132409 (2007).

96. Dhoot, A.S., Israel, C., Moya, X., Mathur, N.D. & Friend, R.H. Large Electric Field Effect in Electrolyte-Gated Manganites. *Physical Review Letters* **102**, 136402 (2009).

97. Pallecchi, I. *et al.* Field effect in manganite ultrathin films: Magnetotransport and localization mechanisms. *Physical Review B* **78**, 24411 (2008).

98. Ghivelder, L. *et al.* Abrupt field-induced transition triggered by magnetocaloric effect in phase-separated manganites. *Physical Review B* **69**, 214414 (2004).

99. Tsori, Y., Tournilhac, F. & Leibler, L. Demixing in simple fluids induced by electric field gradients. *Nature* **430**, 544-547 (2004).

100. MurakamiY. *et al.* Ferromagnetic domain nucleation and growth in colossal magnetoresistive manganite. *Nat Nano* **5**, 37-41 (2010).

101. Bakaul, S.R., Lin, W. & Wu, T. Engineering magnetic domains in manganite thin films by laser interference. *Applied Physics Letters* **100**, 12403-12404 (2012).

102. Burgy, J., Moreo, A. & Dagotto, E. Relevance of Cooperative Lattice Effects and Stress Fields in Phase-Separation Theories for CMR Manganites. *Physical Review Letters* **92**, 97202 (2004).

103. Gao, J., Hu, F. & Liu, H. Field Effects in Thin Films of Manganites Using a Planar Field Effect Configuration. *Journal of Superconductivity and Novel Magnetism* **23**, 855-857

104. Ogale, S.B. *et al.* Unusual Electric Field Effects in Nd_{0.7}Sr_{0.3}MnO_{3}. *Physical Review Letters* **77**, 1159-1162 (1996).

105. Eblen-Zayas, M., Bhattacharya, A., Staley, N.E., Kobrinskii, A.L. & Goldman, A.M. Ambipolar Gate Effect and Low Temperature Magnetoresistance of Ultrathin La_{0.8}Ca_{0.2}MnO_{3} Films. *Physical Review Letters* **94**, 37204 (2005).

106. Pallecchi, I., Pellegrino, L., Bellingeri, E., Siri, A.S. & Marre, D. Reversible shift of the transition temperature of manganites in planar field-effect devices patterned by atomic force microscope. *Applied Physics Letters* **83**, 4435-4437 (2003).

107. Gueguen, Y. & Dienes, J. Transport properties of rocks from statistics and percolation. *Mathematical Geology* **21**, 1-13

108. Barthélémy, J.-F. Effective Permeability of Media with a Dense Network of Long and Micro Fractures. *Transport in Porous Media* **76**, 153-178

109. Ward, T.Z. *et al.* Tuning the Metal-Insulator Transition in Manganite Films through Surface Exchange Coupling with Magnetic Nanodots. *Physical Review Letters* **106**, 157207 (2011).

110. Rairigh, R.P. *et al.* Colossal magnetocapacitance and scale-invariant dielectric response in phase-separated manganites. *Nat Phys* **3**, 551-555 (2007).

111. Ramesh, R. & Spaldin, N.A. Multiferroics: progress and prospects in thin films. *Nat Mater* **6**, 21-29 (2007).

112. Sawa, A., Fujii, T., Kawasaki, M. & Tokura, Y. Hysteretic current--voltage characteristics and resistance switching at a rectifying Ti/Pr[sub 0.7]Ca[sub 0.3]MnO[sub 3] interface. *Applied Physics Letters* **85**, 4073-4075 (2004).

113. Dong, R. *et al.* Improvement of reproducible hysteresis and resistive switching in metal-La[sub 0.7]Ca[sub 0.3]MnO[sub 3]-metal heterostructures by oxygen annealing. *Applied Physics Letters* **90**, 182113-182118 (2007).

114. Nian, Y.B., Strozier, J., Wu, N.J., Chen, X. & Ignatiev, A. Evidence for an Oxygen Diffusion Model for the Electric Pulse Induced Resistance Change Effect in Transition-Metal Oxides. *Physical Review Letters* **98**, 146403 (2007).

115. Tokunaga, Y. *et al.* Colossal electroresistance effect at metal electrode/La[sub 1 - x]Sr[sub 1 + x]MnO[sub 4] interfaces. *Applied Physics Letters* **88**, 223503-223507 (2006).

116. Rozenberg, M.J., Inoue, I.H. & Sanchez, M.J. Strong electron correlation effects in nonvolatile electronic memory devices. *Applied Physics Letters* **88**, 33510-33513 (2006).

117. Kim, D.S., Kim, Y.H., Lee, C.E. & Kim, Y.T. Colossal electroresistance mechanism in a Au/Pr_{0.7}Ca_{0.3}MnO_{3}/Pt sandwich structure: Evidence for a Mott transition. *Physical Review B* **74**, 174430 (2006).

118. Oka, T. & Nagaosa, N. Interfaces of Correlated Electron Systems: Proposed Mechanism for Colossal Electroresistance. *Physical Review Letters* **95**, 266403 (2005).

Vita

Hangwen Guo was born and raised in Shanghai, China. After graduating from Fuxing Senior High School in Shanghai, he spent the next 4 years studying Physics major at the Fudan University, Shanghai, China. By the time he graduated with a BS in Physics in 2003, he decide to go abroad to experience a totally brand new lifestyle. In 2003, he enrolled in the Physics PhD program at the University of Tennessee as teaching assistant and research assistant and spent the next 5 years mainly in Oak Ridge National Laboratory studying on experimental complex material science.